Universita degli Studi Roma Tre

DOCTORAL THESIS

Passive and Active Cellular Micro-Structured Materials for Morphing Applications

Author:
Yingjie Chen

Supervisor:
Dr. Giulia Lanzara

A thesis submitted in fulfillment of the requirements

for the degree of Doctor of Philosophy

in the

Department of Engineering

5 May 2017

The research leading to these results was supported by the European Research Council under the European Union's Seventh Framework Programme (FP/2007-2013)/ERC Grant Agreement n. 308261.

Abstract

Morphing materials represent an emerging field since they have the potential to improve performance of the materials/structures/devices in which they are integrated. These materials have the capability of passively or actively providing radical shape changes to adapt to a varying environment. For this reason, they can be extremely beneficial in several applications including optics, three-dimensional biological scaffolds, airplane skin, micro-air vehicles, controlled drug delivery and smart textiles etc. In this thesis we design, fabricate, test and analyze novel passive and active cellular micro-structured films for morphing applications to provide ultra-light weight, non-invasive, highly stretchable and synclastic shape changes with the addition of 2D and 3D local/global morphing when the films are also active. One of the key aspects in the proposed material design approach is that it is possible to shape the microstructure of a material in such a way that, by strategically adding to the material microstructure extra elements of another forming material, it is possible to switch the material from a passive to an intrinsically active (temperature driven in this case study) response. For instance, in this thesis polyimide-based micro-structured unit cells were designed to form an auxetic film (passive response with synclastic shape changes), but polyimide-based microstructured unit cells with a light integration of poly (vinyl alcohol) microelements, behave as a temperature activated film that can morph in 2D and its intrinsic degree of morphing can be tuned. This is possible because the latter film is structured in such a way to exploit a negative, and indeed tunable, coefficient of thermal expansion. In this case the highest ever presented negative coefficient of thermal expansion for a polymer material is presented and the beauty is that this is done by using only materials with a positive coefficient. Now, if the latter film is sandwiched with another film that has a positive coefficient of thermal expansion, then 3D morphing can be exploited whose response can also be magnified as needed. Another interesting aspect of this research activity is that if the miniaturized cells are properly designed, then it is possible to tune the material properties also in terms of isotropy, anisotropy, energy dissipation, ultra-high stretchability etc. With this in mind, polyimide-based auxetic films with a novel miniaturized structure as well as polyimide-based temperature activated morphing films, were studied in depth. The designed and tested auxetic film provides enhanced auxeticity despite its higher stretchability if compared with existing materials, auxetic anisotropy, hysteretic and repeatable loading/unloading cycles even if performed after auxetic failure which is here for the first time introduced. The active film, that finds its actuation capability in its intrinsic microstructure, is capable to provide tunable and up-to- ultra-low negative coefficient of thermal expansion, isotropic response, in-plane and out-of plane morphing (in the latter case in a multilayer configuration) which, if used in a pixelling fashion can be used to induce local/global, radical and unprogrammed shape changes. Moreover, the latter design is not affected by orders of magnitude stiffness losses as may occurs in other existing morphing materials, and is capable to provide fast responses. The results of this thesis are all based on numerical models (Comsol Multiphysics) that were used to design and predict the material response. They are also based on the implementation and optimization of the fabrication process that was carried-out constantly verifying the resulting microstructure and its influence on the overall material response (tested at the unit cell level as well at the global level).

Acknowledgements

Firstly, I would like to express my sincere gratitude to my advisor Prof. Giulia Lanzara for the continuous support of my Ph.D. study and related research, for her patience, motivation, and immense knowledge. Her guidance helped me in all the time of research and writing of this thesis. I could not have imagined having a better advisor and mentor for my Ph.D. study.

I am grateful to all of those with whom I have had the pleasure to work during my Ph.D. study. Each of the members of our research group and Consiglio Nazionale delle Ricerche (CNR) has provided me extensive personal and professional guidance and taught me a great deal about both scientific research and life in general. I would especially like to thank Dr. Andrea Notargiacomo, who helped me a lot in experimental part of work. My sincere thanks also goes to Kaveh Samadikhah, for the stimulating discussions, for the sleepless nights we were working together before deadlines, and for all the fun we have had in the last four years.

Nobody has been more important to me in the pursuit of this project than the members of my family. I would like to thank my parents, whose love and guidance are with me in whatever I pursue.

Contents

List of Figures

List of Tables

Chapter 1

Introduction

Morphing materials are a class of materials that are capable to change shape. The interesting thing is that there is neither an exact definition nor an agreement between the researchers about the type or the extent of the geometrical changes necessary to qualify a material for the title ‘shape morphing". Here with the term "Morphing" we intend materials that are capable to provide the largest possible, drastic, or, even better, "radical" shape changes. Looking at history, morphing has definitely started in aeronautics for which the idea of taking inspiration from flying creatures has driven this research field. In aeronautics, morphing is ‘a set of technologies that increase a vehicle’s performance by manipulating certain characteristics to better match the vehicle state to the environment and task at hand’ [1]. In view of this definition, the morphing technology is including flaps and retractable landing gear. In early 1890, Clement Ader proposed a morphing wing for an airplane (Eole) which take the inspiration from the bat wing, that could reduce its size to half or one-third of its full deployment. The ‘polymorphic’ aircraft include the Pterodactyl IV that was designed by Geoffrey Hill at Westland in 1931, and the Russian fighter IS-1, which flew in 1940 and was able to switch from a maneuverable biplane to a faster monoplane [1]. Historically, morphing solutions always led to penalties in terms of cost, complexity, or weight, although in certain circumstances, these were overcome by the benefits attained at the overall system level which was summarized by Weisshaar in 2006. Airplanes such as the F-14 Tomcat and the Panavia

Tornado are good examples, where varying the wing sweep angle allows good performance at both low and high speeds [2].

Recent advances in SMART materials may overcome these limitations and enhance the benefits from morphing material solutions. A review of the state-of-the-art of smart structures and integrated systems was presented by Chopra in 2002 [2]. The challenge of morphing smart material is to design a structure that is capable of withstanding not only the prescribed loads, but also to change its shape in order to withstand several load conditions. In order to reduce the complexity and also increase the reliability, the actuation system, consisting of active materials, should be embedded in the structure. Ideally there should be no distinction between the structure and the actuation system, so that the system used to produce and carry the loads, is also capable of changing shape [3]. In addition to the benefits in terms of complexity, reliability, and production cost, such a concept could also prove to be lighter.

Smart morphing materials are not only used in the aeronautical field, but they could also be used in cells scaffold, space system, electronic system and micro-aerial vehicles.

Scaffolds are typically used to provide the necessary support for cells to grow and maintain their function. Several scaffold materials have been investigated for tissue engineering bone and cartilage including hydroxyapatite (HA), poly(a-hydroxyesters), natural polymers such as collagen and chitin and also the composite materials. Several reviews have been published on the general properties and design features of biodegradable and bioresorbable polymers and scaffolds [4-8]. Aforementioned requirements for scaffold materials are numerous, including high porosity and proper pore size, high surface area, biodegradability, mechanical integrity to maintain the predesigned tissue structure, the scaffold should not be toxic to the cells and the scaffold should positively interact with cells, including enhanced cell adhesion, growth, migration, and differentiated function [4]. To fulfil as many requirements as possible, composite systems combining advantages of polymers and ceramics seem to be a promising choice, in particular for bone tissue engineering, as demonstrated by the increasing research efforts worldwidee. Scaffolds serve as temporary, artificial extracellular matrices to accommodate cells and support three-dimensional tissue regeneration. Therefore, it is often beneficial to mimic certain features of a natural extracellular matrix in scaffold design, such as micro to nano-scale structured material which is one of the exciting new areas in tissue engineering [9-17].

The term micro air vehicle (MAV) refers to a new type of unmanned aerial vehicle (UAV) that is significantly smaller than similar aircraft's. This represents another interesting application field for smart morphing materials, such as shape memory alloy, piezoelectric materials and composite materials. The target dimension for MAVs today is approximately 15 centimeters (six inches) and development of insect-sized aircrafts is reportedly expected in the near future. Potential military use is one of the driving factors, although MAVs are also being used commercially and in scientific, police, and mapping applications. As early as 1990s, MIT Lincoln Labs creates concept model of tiny EO reconnaissance system. DARPA holds micro air vehicle technology workshop which leads to 35-million-dollar contract in 1995, also narrows vision for MAVs to use by the individual soldier in 1997 [3]. The requirements of MAV are including high-lift-to-drag ratio, Airfoil Shape, high propulsive power, flight endurance, light-weight and strength of materials. In order to match the requirements, there are several design solutions such as fixed wing, rotary wing and flapping wing. the different design may have different benefit and limitations, the fixed wing design has high speed (up to 40 mph), but not suitable for indoor applications, the rotary wing like mini helicopters has slow fly speed but is able to have hover movements, the flapping wing which takes inspiration from birds is the best for the indoor use. All of these design can benefit from the smart morphing materials which should be light-weight, change the shape without loss of rigidity, have a synclastic shape change and be able to have a global and local deformation in 2D and 3D.

Morphing materials can be divided in two main categories: (a) passive morphing materials and (b) active morphing materials. The passive morphing material can only deform if an external load is applied (e.g. a stretching force) while the active morphing materials can self-deform by thermal, electron or magnetic environment. The common examples of passive morphing material are stretchable materials such as elastomers and auxetics. Elastomers are a class of polymers with a low density of cross-link, and have the ability to undergo large elastic deformations without permanent changes in shape. Auxetics are cellular materials which have a negative Poisson’s ratio thanks to the cell geometry, so under loading the sides of the cells expand outwards producing an overall negative Poisson’s ratio effect. They can be foams, ceramics, composites and polymers, from the macro- to the micro- scales. The most classical active morphing materials include shape memory polymers (SMP), shape memory alloys (SMA), elastic memory composites (EMC), magnetic shape memory materials and piezoelectrics even though theinclusion in the latter in this category is at the limit since they are characterized by small strain levels.

Temperature-responsive polymers are polymers that exhibit a drastic and discontinuous change of their physical properties with temperature. Thermoresponsive polymers belong to the class of stimuli-responsive materials, in contrast to temperature-sensitive (for short, thermosensitive) materials, which change their properties continuously with environmental conditions. In a stricter sense, thermoresponsive polymers display a miscibility gap in their temperature-composition diagram. Depending on whether the miscibility gap is found at high or low temperatures, an upper or lower critical solution temperature exists, respectively (abbreviated UCST or LCST). Heló ïse and Zi Liang designed a gel sheets which can achieve multiple 3D shape transformations in response to distinct external triggers [18]. The gel sheet was prepared by primary hydrogel (P(NIPAm-co-HEAM)) and binary gel (poly(NIPAM-co-HEAM)/PNIPAm) which has different response under thermal gradients. The LCST of primary hydrogel is 50°C and binary gel is 35°C, which lead to the result shown in Fig. 1.1. The hydrogel sheets have two phases of deformed shape, they show a helix shape when the temperature reaches LCST of binary gel which is above 35°C and below 50°C. In this phase the binary gel is shriking and the primary hydrogel stays stable (Fig.1.1b). When the temperature continues to increase up to 60°C, which is above the LCST of both gels, the material shrinks uniformly (Fig. 1.1c).

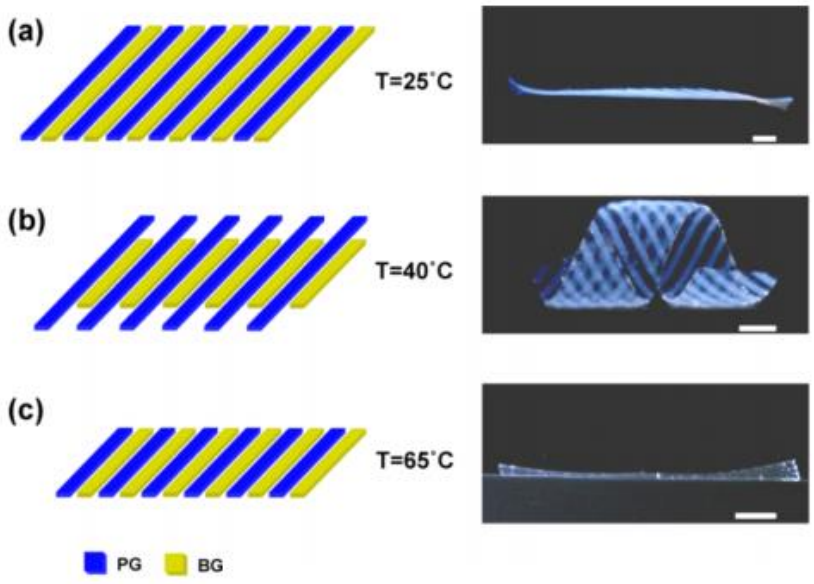

FIG.1.1. SHAPE TRANSFORMATIONS OF THE GEL SHEET COMPOSED OF P(NIPAM-CO-HEAM) (PG) AND POLY(NIPAM-CO-HEAM)/PNIPAM (BG) STRIPES. (A) AT 25 °C, PG AND BG REGIONS HAVE SIMILAR DIMENSIONS (LEFT) AND THE GEL ACQUIRES A PLANAR SHAPE (RIGHT). (B) AT 45 °C, THE BG REGIONS SHRINK (LEFT), AND THE GEL ADOPTS A HELICAL SHAPE (RIGHT). (C) AT 65 °C, THE PG AND BG REGIONS BOTH SHRINK TO THE SAME EXTENT (LEFT) AND THE SHEET RETURNS TO A PLANAR CONFORMATION (RIGHT).

Shape memory polymers (SMPs) represent one of the most important class of stimuli-responsive materials [19]. More specifically, the conventional definition of a SMP is a polymer that can be deformed and subsequently fixed into a temporary shape, which would remain stable unless it is exposed to an appropriate external stimulus that triggers the polymer to recover to its original (or permanent) shape [20]. The recovery process can be activated by a change in temperature, although alternative stimuli including magnetic, electric, light and electromagnetic field have been investigated [21-23].

Covalently cross-linked thermosetting and thermoplastic networks are one type of SMP which are highly programmable than semi-crystalline polymers whose properties of crystalline domains are highly strong [24]. The thermoset-thermoplastic network SMPs have certain properties which freely allowed the modification around glass transition temperature (T_g). The shape memory process is shown in Figure 1.2; the original shape can be modified under external loading when the temperature increases to Tg, and then the shape can be fixed while the temperature decreases to room temperature by keeping the external load [25]. Once the temperature goes to Tg, the SMP recovers the original shape without the need of an externalload. This is a single cycle process, which means that the SMP need the application of another load to start another cycle. This type of SMPs have some benefits such as high recovery rate, high degree of deformation capacity thanks to the strong chemical cross-links [26]. The SMPs also have some important limitations; the rigidity of SMPs reduces once temperature is close to T_g, external loads are needed for shape modifications [27].

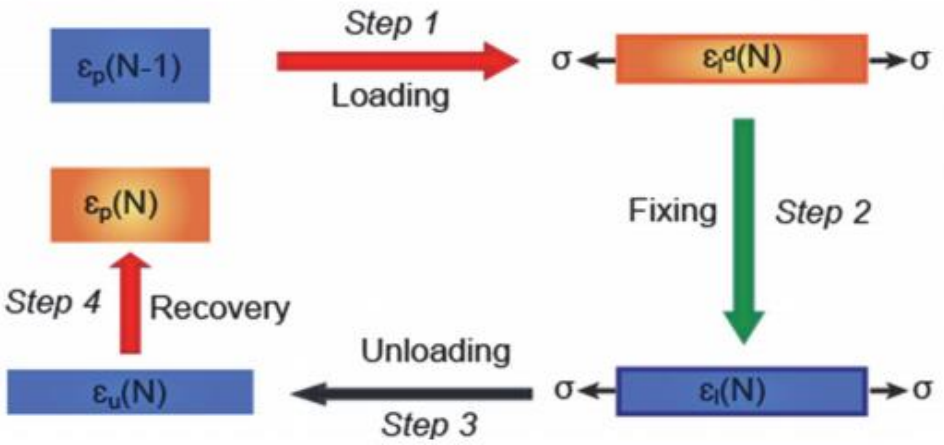

FIG. 1.2. THE MECHANISM OF SHAPE MEMORY POLYMER FUNCTION CYCLES.

Reversible SMPs were recently investigated. In this case there are two types of chemical structures; one is the core which connects thermosets and thermoplastics have thermo-sensitive properties. The thermo-sensitive core can slightly extend in high temperature and shrink when cooled down. Another possibility is related to the polymer crystallization and orientation of attachments, the thermoset which works as scaffold can lead to the orientation of crystallization and lead to the reversible property. The PPD-PCL reversible SMP was investigated by Marc Behl. et al. [27]. The molecular structure is shown in Figure 1.3 in which the red part represents the skeleton domain which is PPD, and the green part represents PCL that fills the gaps within the skeleton. When the temperature reaches T_{reset}, which is higher than Tg of PPD and PCL, the sample can be programmed under loading. Then, when the temperature decreases to T_{low}, which is lower than the Tg of PPD and PCL, the deformed shape is fixed without the need to remove the external load. Then the reversible shape memory effort (rbSME) is shown between T_{high} and T_{low}. T_{high} is the temperature higher than Tg of PCL and lower than Tg of PPD (shown as Figure 1.4). Although reversible SMPs do have the benefit of recycling recovery, they still have few limitations. The major limitation is that the degree of recovery is limited, as PPD-PCL is reversible, the SMP does not have the ability to recover totally, this is because the temperature request to recover totally is very close to T_{reset} which is the point when the SMP loses rigidity. Another limitation is that the reversible process allows only expansion and shrinking movements, so the shape of recovery is automatic and limited. Also this reversible SMP may have some problems and risk of recover speed and mechanical properties.

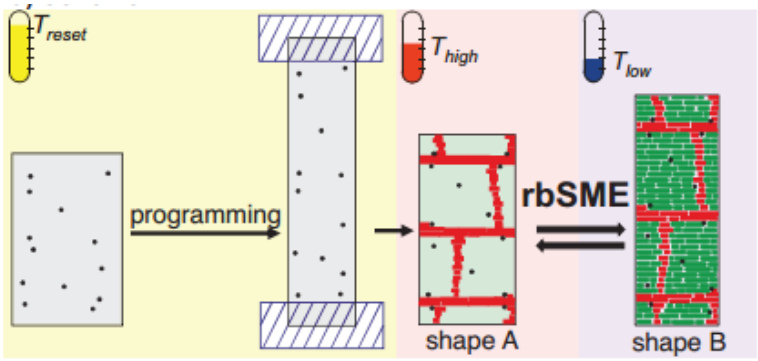

FIG. 1.3. SCHEMATIC OF THE RBSME COPOLYMER NETWORKS: AFTER DEFORMATION AT TRESET THE SKELETON DOMAINS (RED), WHICH DETERMINE THE SHAPE SHIFTING GEOMETRY, ARE CRYSTALLIZED BY COOLING (PROGRAMMING). THE RBSME IS TRIGGERED BY THE REVERSIBLE CRYSTALLIZATION AND MELTING OF ORIENTED ADS (GREEN). BLACK DOTS: CROSSLINKS. [27]

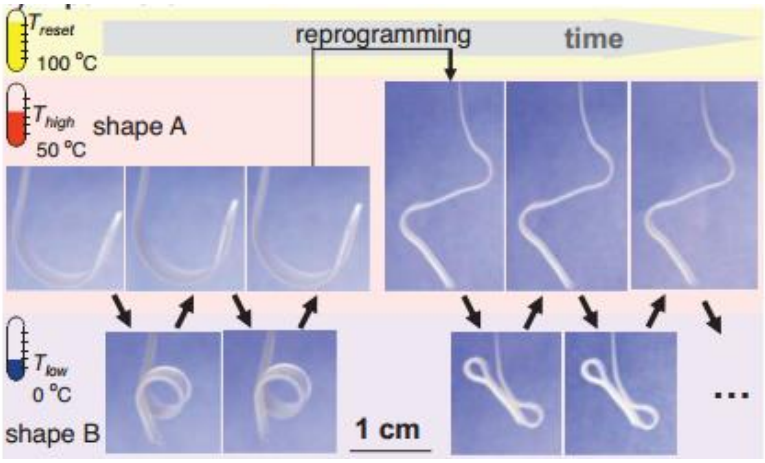

FIG. 1.4. PHOTOGRAPH SERIES SHOWING RBSME OF A POLYMER RIBBON (40 MM × 4 MM × 0.4 MM) FROM PPD-PCL (75). THE BOWED SHAPE WAS OBTAINED AFTER PROGRAMMING BY DEFORMATION IN A HELIX LIKE SHAPE AT TRESET, COOLING TO TLOW AND SUBSEQUENT HEATING TO THIGH. THE RBSME OCCURRED AS REVERSIBLE SHIFT BETWEEN SHAPE A (BOW) AT THIGH AND SHAPE B (HELIX) AT T LOW. THE SAMPLE WAS REPROGRAMMED BY TRESET INTO AN OPEN SHAPE (NEW SHAPE A), WHICH COULD BE SHIFTED REVERSIBLY TO A FOLDED SHAPE (NEW SHAPE B). [27]

Since both of scaffolds and micro air vehicles would benefit from lightweight materials that can have synclastic passive and active shape changes at the local and/or global level, we believe that the solution is to use materials that, while minimizing the amount of material, are capable to perform the same functions (discrete material instead than continuous). These materials additionally should have a structure at the microscale that can allow for synclastic shape changes and possibly for controlled local/global in plane or out-of-plane morphing. For this reason, in this thesis the focus is on materials that have a miniaturized cellular structure that follows different designs. First we study the case of passive cellular materials that can give synclastic shape changes, then we focus on active materials that can morph in-plane and out of plane in different length-scales.

References

1. Weisshaar, T.A. 2006. 'Morphing Aircraft Technology New Shapes for Aircraft Design,' RTO-MP-AVT-141, Neuilly-sur-Seine, France.

2. Chopra, I. 2002.Review of State of Art of Smart Structures and Integrated Systems, AIAA Journal, 40:21452187.

3. Michelson, R. C. 2010 "Overview of Micro Air Vehicle System Design and Integration Issues", Encyclopedia of Aerospace Engineering

4. Ma, Peter X, Scaffolds for tissue fabrication, MATERIALS TODAY, 7: 5, 30-40, MAY 2004

5. Naughton GK, et al. Emerging developments in tissue engineering and cell technology. Tissue Eng 1995;1(2):211-9.

6. Agrawal C, Niederauer G, Micallef D, Athanasiou K. The use of PLA-PGA polymers in orthopaedics. In: Encyclopedic handbook of biomaterials and bioengineering. New York: Marcel Dekker, 1995. p. 2081-115.

7. Kronenthal RL. Biodegradable polymers in medicine and surgery. Polym Sci Technol 1975;8:119-37.

8. D.W. Hutmacher, Scaffolds in tissue engineering bone and cartilage, Biomaterials 21 (2000), 2529-2543

9. Drotleff S, Lungwitz U, Breunig M, Dennis A, Blunk T, Tessmar J. Biomimetic polymers in pharmaceutical and biomedical sciences. Eur J Pharm Biopharm 2004;58:385–407.

10. Suchanek W, Yoshimura M. Processing and properties of hydroxyapatite-based biomaterials for use as hard tissue replacement implants. J Mater Res 1998;13:94–117.

11. Chaikof EL, Matthew H, Kohn J, Mikos AG, Prestwich GD, Yip CM. Biomaterials and scaffolds in reparative medicine. Ann NY Acad Sci 2002;961:96–105.

12. Antoniou G, Mikos AG, Temenoff JS. Formation of highly porous biodegradable scaffolds for tissue engineering. Electron J Biotechnol 2000;3.

13. Levenberg S, Langer R. Advances in tissue engineering current topics in developmental biology, vol. 61. New York: Academic Press; 2004 (p. 113–134).

14. Griffith LG. Emerging design principles in biomaterials and scaffolds for tissue engineering. Ann NY Acad Sci 2002;961:83–95.

15. Karageorgiou V, Kaplan D. Porosity of 3D biomaterial scaffolds and osteogenesis. Biomaterials 2005;26:5474–91.

16. Tirelli N, Lutolf MP, Napoli A, Hubbell JA. Poly(ethylene glycol) block copolymers. Rev Mol Biotechnol 2002;90:3–15.

17. Berger J, Reist M, Mayer JM, Felt O, Peppas NA, Gurny R. Structure and interactions in covalently and ionically crosslinked chitosan hydrogels for biomedical applications. Eur J Pharm Biopharm 2004;57(1):19–34.

18. Heló ïse Therien-Aubin, Zi Liang Wu, Zhihong Nie, and Eugenia Kumacheva, Multiple Shape Transformations of Composite Hydrogel Sheets, J. Am. Chem. Soc. 2013, 135, 4834−4839

19. Tao Xie. Recent advances in polymer shape memory. Polymer 52; (2011); 4985-5000.

20. Qinghao Meng, Jinlian Hu. A review of shape memory polymer composites and blends. Composites: Part A 40 (2009) ; 1661–1672.

21. R. Biju, C. Gouri, C.P. Reghunadhan Nair. Shape memory polymers based on cyanate ester-epoxy-poly (tetramethyleneoxide) co-reacted system. European Polymer Journal 48 (2012);499–511.

22. Hendrik Lützen, Thorsten M. Gesing, Byung Kyu Kim, Andreas Hartwig. Novel cationically polymerized epoxy/poly(3-caprolactone) polymers showing a shape memory effect. Polymer 53 (2012); 6089-6095.

23. I. Bellin, S. Kelch, R. Langer, and A. Lendlein. Polymeric triple-shape materials. PNAS 2006;10;48; 18043–18047

24. Heloıse The´rien-Aubin, Julien E. Gautrot, Yu Shao, Jie Zhang, X.X. Zhu. Shape memory properties of main chain bile acids polymers. Polymer 51 (2010); 22–25

25. Jinlian Hu, Yong Zhu, Huahua Huang, Jing Lu. Recent advances in shape–memory polymers: Structure, mechanism, functionality, modeling and applications. Progress in Polymer Science 37 (2012); 1720– 1763.

26. I. S. Kolesov, H.-J. Radusch. Multiple shape-memory behavior and thermal-mechanical properties of peroxide cross-linked blends of linear and short-chain branched polyethylenes. Polymer Letters Vol.2, No.7 (2008) 461–473.

27. Marc Behl , Karl Kratz. Reversible Bidirectional Shape-Memory Polymers . Adv. Mater. 2013, 25, 4466–4469

Chapter 2

Auxetic Materials

2.1. A Schematic Overview

Auxetic materials were introduced for the first time by Evans in 1991. The key property auxetics is the negative Poisson's ratio for which the material becomes wider when stretched and thinner when compressed (Fig. 2.1) [1]. Most auxetic materials are man-made, but a few can also be found in nature. The natural auxetic materials can be found in biological tissues (skin) and pyrolytic graphite while man-made auxetics were first used in moderator core of Magnox nuclear reactor [3-7]. The cellular materials have several advantages if compared with solid materials and these include low density, light weight, high acoustic isolation and damping, durability at dynamic loading and fatigue etc [8].

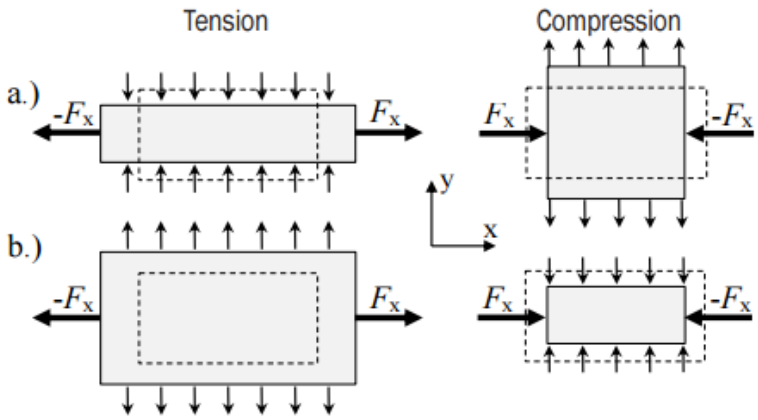

FIG. 2.1. NON-AUXETIC A) AND AUXETIC B) BEHAVIOUR DURING TENSILE AND COMPRESSIVE LOADING (DASHED LINES – UNDEFORMED GEOMETRY)

To date, a variety of auxetic materials and structures have been discovered, fabricated, or synthesized ranging from the macro-scale down to the molecular scale. The auxetic polymeric materials include: polyester urethane (PU), polyimide (PI), polytetrafluoroethylene (PTFE), Ultra-High molecular weight polyethylene (UHMWPE), polypropylene (PP), polyester, nylon and etc, when they are in the form of foams, fibers and composites. Over the past decades, several geometrical structures were proposed, studied and tested. The most common of these structures are: re-entrant and chiral structures, rotating units, angle-ply laminates, microporous polymers and liquid crystalline polymers. A systematic review of these structures is given as follows.

Re-entrant structures

The macroscopic auxetic cellular structure in Figure was firstly suggested by Gibson et al. in 1982. This structure can be deformed by hinging the diagonal ribs in response to an applied stretching load. Development of 2D re-entrant honeycombs (Fig. 2.2) started with analytical calculations of various deformation mechanisms caused by flexing the cell walls [9]. More realistic behaviours consist on honeycombs that undergo flexure, stretching and hinging deflections when subjected to external loadings [10].

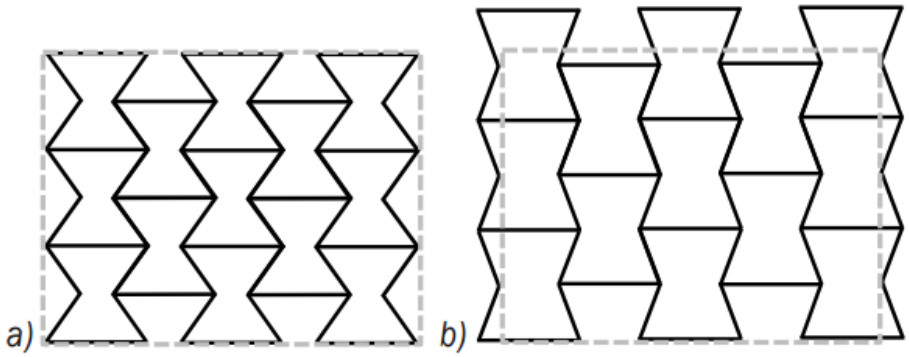

FIG.2.2. RE-ENTRANT AUXETIC STRUCTURES A) UNDEFORMED AND B) DEFORMED RE-ENTRANT STRUCTURE

Chiral structures

Chiral structures are another kind of structures which are formed by interconnecting straight wires known as ribs to central nodes. The nodes may be circles or other geometrical forms (Fig. 2.3). The auxetic effects are achieved through wrapping or unwrapping of the wires around the nodes in response to the applied force. Poisson's ratio of chiral structures is –1, based on theoretical and experimental investigation by Prall and Lakes in 1977 [11,12]. This Poisson ratio is greater than other auxetic designs.

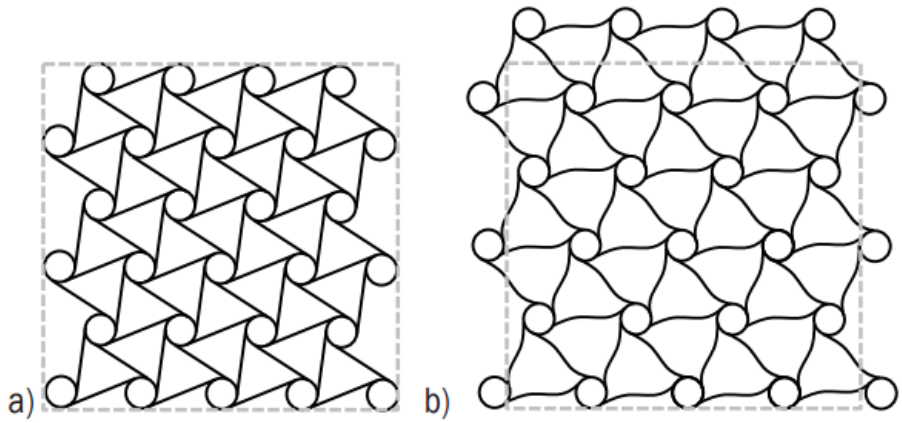

FIG. 2.3. CHIRAL AUXETIC STRUCTURES. A) UNDEFORMED AND B) DEFORMED CHIRAL STRUCTURE

Rotating units

The rotating units were presented by Grima and Evans in 2000 and are shown in Figure 2.4. This structures can be used in nanostructure networked polymers and foams, by joining the rigid or semi-

rigid triangles, squares, rectangles and tetrahedron. These designs can theoretically reach a Poisson ratio equal to -1 [13].

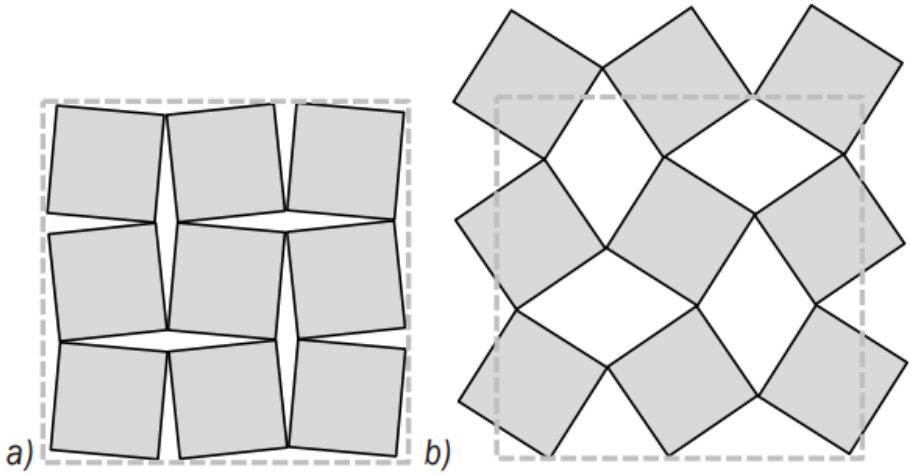

FIG. 2.4. ROTATION AUXETIC STRUCTURES. A) UNDEFORMED AND B) DEFORMED ROTATING RECTANGLES

2.2. Auxetics in this Thesis Context

The auxetic materials were chosen for the passive cellular material as it exploits a negative Poisson ratio which allows them to expand transversally while being stretched. This unique mechanical response is related to special geometries in the structure of cellular materials. Auxeticity was demonstrated in foams [14], polymers [15] and composite structures [16-19] mostly by means of macro-scaled cells. In this context, as mentioned earlier re-entrant, chiral and hexachiral structures are the most widely used because of their excellent response in terms of auxeticity. Several applications could benefit from the use of micro-scaled cellular materials especially when lightweight but outperforming functional "films" need to be used. To name just a few examples, auxetic lightweight films could be of great interest for morphing micro-robots, aerial vehicles, filters and smart textiles. The bio-medical field would also take advantage of such materials for all cases where biological cells need to interact with a foreign object, as in implantable devices or non-invasive surgical tools [20].

Tissue engineering is an emerging field in which often scaffolds are used to guide the growth of the biological tissues. In this context, miniaturized auxetic scaffolds could help the cells growth allowing

also cells differentiation and tissue viability [21]. The problem is that the auxetic response is known to depend on the scale of the cellular structure [22-24]. This is true not only because at different scales specific forces (e.g. surface related or mass related) could have a different impact on the mechanical response, but also because materials (e.g. polymers) may very their properties when their size (e.g. thickness) goes below or above specific threshold values. To the best of our knowledge, very little work has been done towards auxetics miniaturization [26]. Recent efforts by the Multifunctional Materials group at RomaTre University, have designed and optimized a modified hexachiral structure formed by micro-scale elements reaching a numerical 20% strain improvement in auxetic response if compared with the theoretically predicted hexachiral structure. In this thesis, the above mentioned modified micro-scaled hexachiral design is investigated through an experimental campaign and compared with numerical studies. Major challenges (from manufacturing to testing and analysis) that are related to the decrease in length-scale, are phased and discussed.

2.3. References

1. Ken E Evans, Auxetic polymers: a new range of materials, Endeavour, Vol 15, 4, 1991
2. Luzhuo Chen, Changehong Liu, Auxetic materials with large negative Poisson's ratios based on highly oriented carbon nanotube structures, Applied Physics Letters, Vol 94, 25 2009
3. R. BLUMENFELD, Auxetic strains—insight from iso-auxetic materials, Molecular Simulation, Vol. 31, No. 13, 15 November 2005, 867–871
4. Wan H, Ohtaki H, Kotosaka S, Hu G (2004). M. A study of negative Poisson's ratios in auxetic honeycombs based on a large deflection model. Eur. J. Mech. Solids, 23: 95-106.
5. Evans KE (1991). Design of doubly-curved sandwich panels with honeycomb cores. Compos. Struct, 17: 95-111.
6. Grima JN, Alderson A, Evans KE (2005a). Auxetic behaviour from rotating rigid units. Phys. Stat. Sol., (b) 242: 561-575. Grima JN, Alderson A, Evans KE (2005b). An Alternative Explanation for the Negative Poisson's Ratios in Auxetic Foams Jpn. J. Phys. Soc., 74: 1341-1342.
7. Grima JN, Farrugia PS, Gatt R, Attard D (2008a). On the auxetic properties of rotating rhombi and parallelograms: A preliminary investigation. Phys. Stat. Sol, 245: 521-529.
8. K.E.EVANS, A. ALDERSON, AUXETIC MATERIALS: FUNCTIONAL MATERIAL AND STRUCTURES FROM LATERAL THINKING!. ADV. MATER. 2000, 12, NO.9
9. Mary T A, Evans J S O, 1996, Negative Thermal Expansion from 0.3 to 1050 Kelvin in zrw2o8, science.Vol. 272, Issue 5258, pp. 90-92
10. Matsuda T, Kim J E, etc, 2009, Universal thermal response of the Prussian blue lattice, Phys. Rev. B 79, 172302.
11. Masaki Azuma, etc, Colossal negative thermal expansion in binio3 induced by intermetallic charge transfer, Nature Communications 2, Article number: 347 (2011)
12. Nejc Novak, Auxetic Cellular Materials - a Review, Journal of Mechanical Engineering 62(2016)9, 485-493
13. Marian Mir, Murtaza Najabat Ali, etc. Review of Mechanics and Applications of Auxetic Structures, Advances in Materials Science and Engineering Volume 2014

14. Lakes, R. S., 1987, “Foam Structures with a Negative Poisson’s Ratio” Science Vol. 235, pp. 1038-1040.
15. Herakovich, C. T., 1984, “Composite Laminates with Negative Through-the-thickness Poisson’s ratios”, Journal of Composite. Materials, Vol. 18, pp. 447-455.
16. Prall, D., and Lakes, R. S., 1996, “Properties of a chiral honeycomb with a poisson's ratio -1," International Journal of Mechanical Sciences, Vol. 39, pp. 305-314.
17. Alderson, A., Alderson, K.L., 2007, “Auxetic Materials”, Journal of Aerospace Engineering, Vol. 221, pp. 565-575.
18. Scarpa, F., Panayiotou, P., Tomlinson, G., 2000,” Numerical and experimental uniaxial loading on in-plane auxetic honeycomb”, Journal of Strain Analysis, Vol. 35, pp. 383-388
19. Scarpa, F., Adhikari, S., Wang, C. Y., 2009, “Mechanical properties of non-reconstructed defective single-wall carbon nanotubes”, Journal of Physics D, Vol. 42, pp. 2002-2008
20. Soman P., Lee J. W., 2012, “Spatial tuning of negative and positive Poisson’s ratio in a multilayer scaffold”, Acta Biomaterialia, Vol. 8, pp. 2587–94.
21. Lantada A. D., Muslija A. And García-Ruíz J. P., 2015, “Auxetic tissue engineering scaffolds with nanometric features and resonances in the megahertz range”, Smart Materials and Structures, Vol. 24 , pp. 055013.
22. Gatt R., Caruana-Gauci R., 2014, “On the properties of real finite-sized planar and tubular stent-like auxetic Structures”, Phys. Status Solidi B, Vol. 251, 2, pp. 321–327.
23. Valente J., Plum E., Youngs I. J., and Zheludev N. I., 2016, “Nano- and Micro-Auxetic Plasmonic Materials”, Adv. Mater., Vol. 28, pp. 5176–5180
24. Ma Y., Zheng Y., 2013, “Heterogeneous PVA hydrogels with micro-cells of both positive and negative Poisson's ratios”, Journal of the Mechanical Behavior of Biomedical Materials, Vol. 23, pp. 22-31.
25. Samadikhah K. And Lanzara G., 2015, "Can Micro-Chiral Cellular Structures Be Auxetic?", ASME 2015 International Design Engineering Technical Conferences and Computers and Information in Engineering Conference, Vol. 4: 20th Design for Manufacturing and the Life Cycle Conference; 9th International Conference on Micro- and Nanosystems, Boston, Massachusetts, USA, August 2–5, 2015, Paper No. DETC2015-47771, pp. V004T09A020, doi:10.1115/DETC2015-47771

26. Xu B., Arias F., Brittain S. T., Zhao X. M., Grzybowski B., Torquato S. And Whitesides G. M., 1999, "Making negative Poisson’s ratio microstructures by softlithography", Advanced Materials, Vol. 11, pp. 1186–9.

Chapter 3

Novel Auxetic Films with a Miniaturized Cellular Structure

In Chapter 2 the most common auxetic materials and the principle behind auxeticity, were presented. It was also shown that most of these materials have been developed with macro-scaled cellular units due to the major field of applications for which macro-scaled units are sufficient. However, there are some applications (e.g. micro-air vehicles or biomedical applications) for which polymeric morphing materials need to be applied in relatively small areas and need to exploit different properties (better listed in section 3.1) than those most classically required for auxetics.

In this chapter a novel passive morphing film that is characterized by a miniaturized cellular structure and that can be used for small-scale applications (as for micro-air vehicles as well as for biomedical devices) is presented. The presented designs can also provide different degrees of deformation. The reduction in scale of the cellular units has a significant impact on the material characterization and properties. The response of polymeric micro-scaled cells is in fact strongly influenced by surface forces and changes dramatically in air or in a liquid environment. These issues are investigated in

broad detail as reported in the following sections. This study is carried out both numerically and experimentally.

3.1. The Material Design Objective

Small scale applications like for instance micro-air vehicles and biomedical devices/implants, could largely benefit from the use of passive morphing materials. As earlier discussed, morphing in general implies large-scale deformations and, if these deformations need to take place in 3D, then the problem becomes more complex. This is because in such a case, materials with the capability to provide synclastic shape changes are necessary. The most classical materials that can provide such a property are "auxetics". However, as mentioned earlier, auxetic materials are limited by their macro-scale cells, thus they can't be used as they are for small-scale applications. It is believed that the major requirements that a synclastic material should have to be used in such applications are:

- ultra-light weight
- flexible
- highly stretchable

Based on this brief but critical list of properties (it is critical if compared with existing auxetics), here novel materials designs are presented. The following key elements can be highlighted:

- polymeric film: this allows to reach easily mechanical flexibility
- miniaturized cellular structure: this allows to further reduce weight (further because polymers are already lightweight themselves), to reduce impact in a hosting material/devices/structure
- auxetic unit cells: this allows to reach the synclastic shape changes
- highly stretchable: this allows to reach larger deformations in general but also larger auxetic deformations than ever presented and to be used for applications were radical morphing is essential

The films are designed and then tested to work in different environments such as: liquid and air, but also in environments that are able to simulate variable surface tensions which appear to be the most unique and critical aspect when comparing with standard (macro) auxetics.

3.2. The Film Designs

All of the presented designs take inspiration from the existing hexachiral structure presented in Chapter 2. However here some major modification has been inserted so that the mechanical response is significantly different and, from some prospective, the resulting material has improved properties like for example in terms of stretching capability. First of all, the film consists of an aggregation of polymeric unit cells whose sizes are built at the microscale. In particular, the forming material is chosen to be Polyimide because of its biocompatibility, excellent mechanical properties and capability of withstanding rush environmental conditions such as high temperature, chemical agents etc. In this way our work can be applied for both above mentioned bio and aviation applications.

First we present the unit cell design and its working principle, then we specialize it to the ultra-high stretch ability concept. The characterization of the designed cells and of the films will then be addressed experimentally and numerically up to fatigue testing.

3.2.1. Unit Cell Design

The modified hexachiral structure consists of a central node that is interconnected to six peripheral nodes through slender microwires (Figure 3.1). The uniqueness of this design is that the two nodes that are interconnected by a microwire are mirrored with respect to an ideal line that interconnects the central node with the midpoint of the microwire.

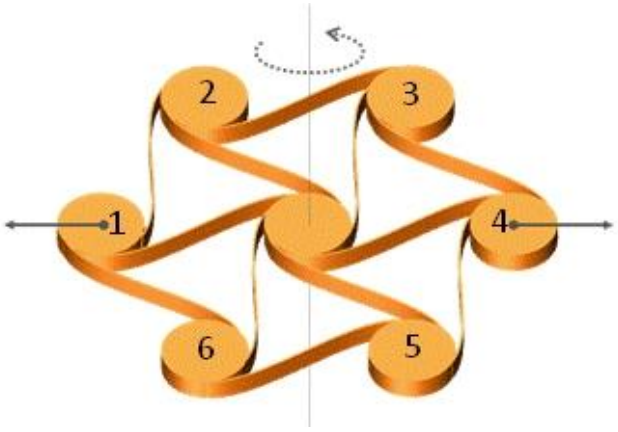

FIG 3.1. SCHEMATIC OF THE MICROCELL DESIGN.

As a consequence, microwires have a tilting angle of 30° if compared with the original hexachiral structure and show a wavy shape that facilitates rotation and delays wire buckling in large strain.

The auxetic mechanism of the cell is similar to a flower opening and closing since, the application of a load in one direction results into the rotation of the centre node. The cell then wraps or unwraps accordingly. A counter clockwise rotation helps the centre node to push-out the connected wires expanding the cell. Similarly, a clockwise rotation induces the connected wires to wrap around the centre node shrinking the cell. Microwires are 5000 μm long (node-to-node distance), 16μm wide and interconnect nodes that have a radius of 500 μm [12].

The pseudo-symmetry of the cell microstructure was related to the anisotropic auxetic response of the cell when loaded in different directions starting from horizontal to the vertical axis. The corresponding response is analysed in terms of *coefficient of auxeticity*. Obviously, when the cells are loaded at their nodes centre, a momentum could be induced to the system for loading directions that are different from the horizontal and vertical ones.

3.2.2. Discrete Film Microstructure Design

A 2D auxetic film with a miniaturized structure is formed by an array of single cells. The film can be considered as an aggregation of cells whose mechanical response depends on the interaction of the cells within each other so as to provide a global auxetic response. It is expected that the cells response should have a strong influence on the overall film response. For this reason, as well as to have a correct boundary condition, the cells are aggregated in such a way to deliver the hexagonal film shown in Figure 3.2. This hexagonal film is pseudo-symmetric as the forming cells, thus, the response was again related to the anisotropic auxetic response of the cell. In particular, the auxetic response of the film is then characterized by the following pulling categories: horizontal, vertical, 60° and 120°. The corresponding behaviour of the film with respect to the different loading directions is expected to follow the single cell response.

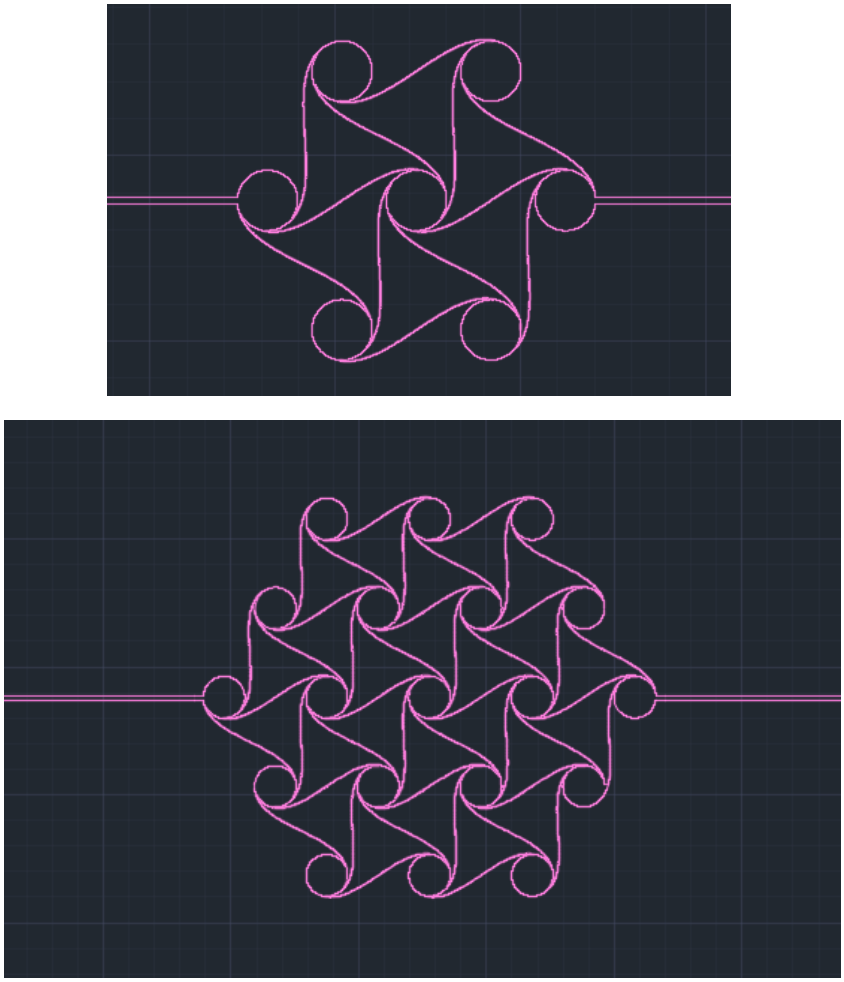

FIG. 3.2. SINGLE CELL AND AN AGGREGATION TO FOR A MINIATURIZED CELLULAR FILM.

3.2.3. Microstructure Design of a Discrete Film with Enhanced Stretching Capability

The enhancement of the stretching capability of the film was achieved by introducing a novel design (shown in Fig. 3.3) in which the cell is initially rolled and then it unrolls by expanding in all directions uniformly, reaching toward the end of the expansion process, a configuration that is near to the initial configuration of the cell design shown in Fig. 3.2. The uniform expansion in all directions is due to the auxetic design of the highly expandable cells, so, by pulling the cell in one direction, it will expand also in the other direction (negative Poisson coefficient).

In particular, two designs are presented:

1. ***fully rolled cell*** (Fig. 3.4a)

2. ***partially rolled cell*** - the rolled parts are intercalated by short straight segments (Fig. 3.4b).

The designed auxetic film is characterized by a significantly larger degree of stretching capability than our initial design which already had higher stretchability than standard hexachiral structures.

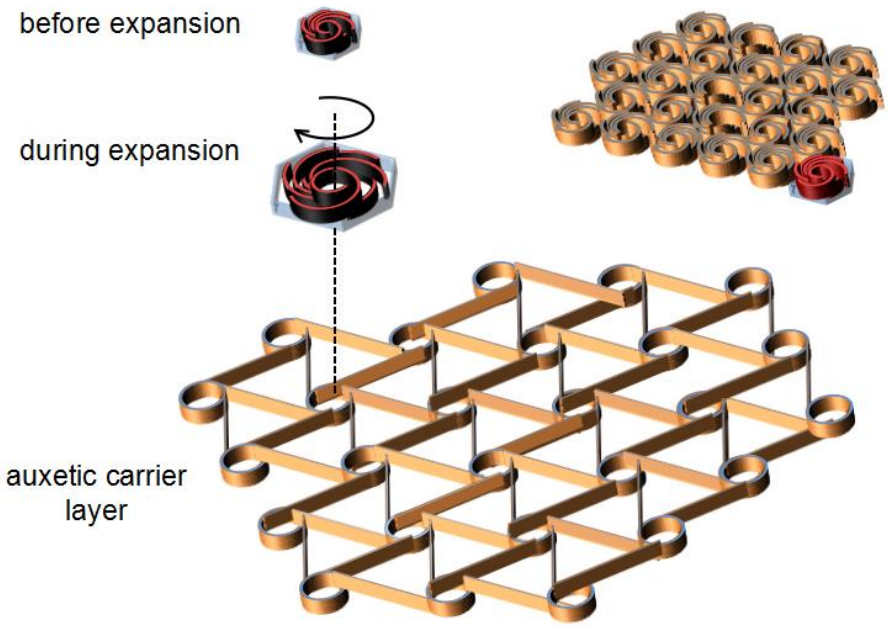

FIG 3.3. SCHEMATIC OF THE PROPOSED CONCEPT TO REACH ULTRA-HIGH STRETCHABILITY.

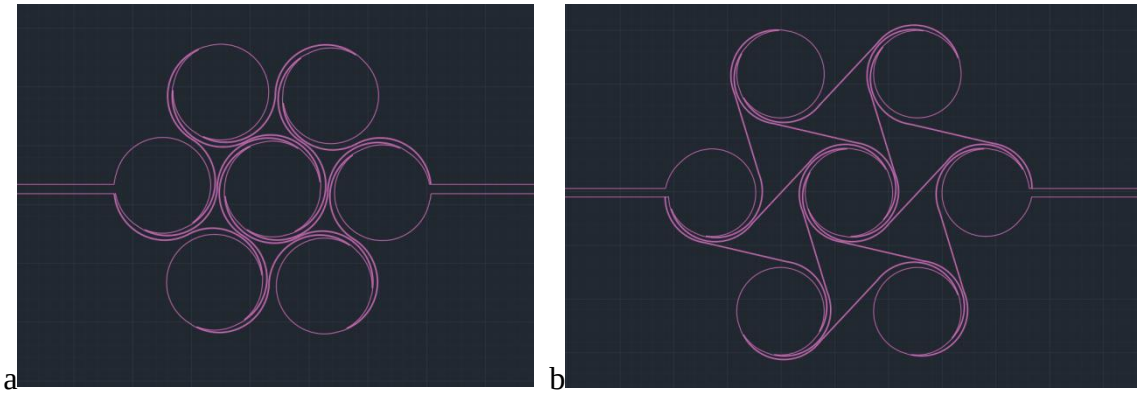

FIG 3.4. LEFT: FULLY ROLLED CELL DESIGN; RIGHT: PARTIALLY ROLLED DESIGN.

3.3. Fabrication Process

A non-standard microfabrication process was designed and implemented to realize the auxetic films. The above mentioned fabrication process requires the design of a photolithography mask whose polarity can be easily exchanged based on the chosen photoresist. The mask was conceived in such a way to be able to produce single wires and aggregations of wires and nodes differently oriented within the plane. Each single independent feature of the mask (the microwires or the networks) is surrounded and supported by a frame that has been designed to facilitate handling of the fabricated structures. These external frames are macroscopic in size, thus, they capture the eye in a normal vision. It is only under the microscope that the smaller-in-size network and wires can be inspected. The mask drawing is reported in Figure 3.5. The schematic of the fabrication process is shown in Fig. 3.6 (a-d). Liquid Polyimide (PI 4110, Microsystem) was spin coated on a silicon wafer with a constant acceleration for a 5s, followed by a final spin speed of 1500rpm for 30s. This speed was adjusted to achieve a film thickness of 40µm (Fig. 3.6(a)). Soft bake processing, which can influence the stability of the final sample, was performed on the hotplate at 90 °C for 3min, followed by an additional 3 min soft bake at 110 °C. It is worth noting that the soft bake in terms of temperature and time, was optimized because it depends on the thickness of the polyimide layer. The sample was then exposed for 20s once it was cooled down to room temperature (Fig. 3.6(b)). After 5 minutes the sample was developed with a spray system (Fig. 3.6(c)).

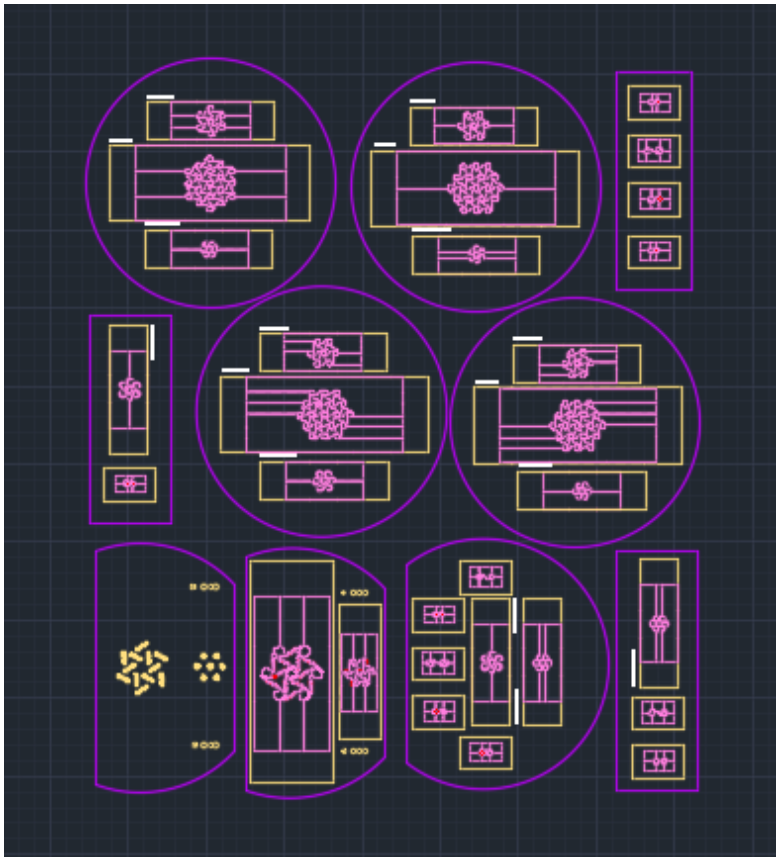

FIG 3.5. MASK DESIGN OF THE AUXETIC NETWORK.

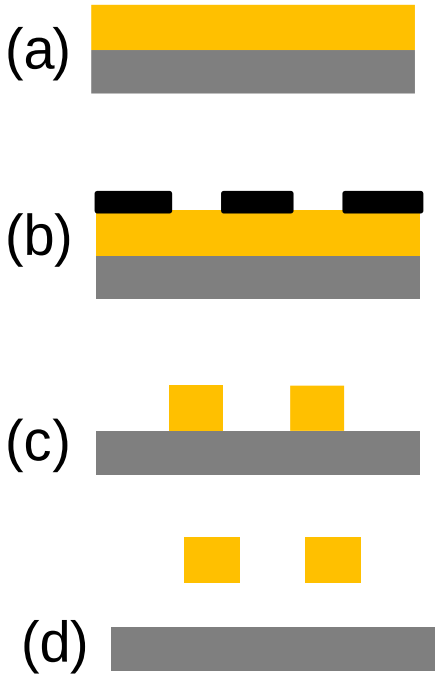

FIG. 3.6. SCHEMATIC OF THE FABRICATION PROCESS.

The development procedure was quite complex since it was performed in eight steps of spray/puddle with a nominal develop time of 20 seconds per spray/puddle step and for a total time of 160 seconds. The sample was then rinsed for 10s and post-baked at 150°C for 60s. The resulting polyimide micro-structures were analyzed after development using an optical microscope while the thickness was measured with a profilometer.

Finally, the material was lifted-off in an HF (49%) bath for 3min (Fig. 3.6(d)) and then was washed in a water bath for three times. The polyimide samples were then cured in air at 200 °C for 30min and then at 300 °C for 60min. As later discussed, the major challenge was found to be related to the wire shape which was lost during the above described fabrication process. The release step was then modified through a several iterative improving steps finally reaching a perfect wire shape with the optimized procedure. Figure 3.7 (a) shows an optical microscope image of a node with the interconnected microwires resulting from the above described initial fabrication procedure.

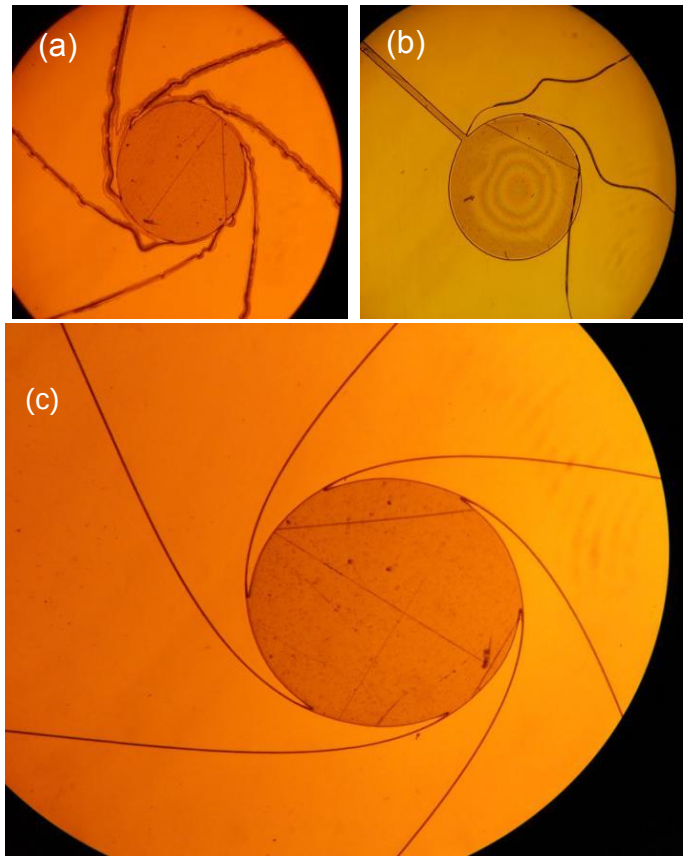

FIG. 3.7. FABRICATION PROCESS IMPROVEMENT. OPTICAL MICROSCOPE IMAGES.

In this case the sample development was done in a chemical bath. The sample was then dried out with Nitrogen. The image clearly shows that the process is not satisfactory. The resulting wire shows in fact a wavy shape where the waviness is different from the design. For this reason, the spray/puddle method, which avoids the wire floating in the bath, was adopted. The resulting sample is shown in Fig. 3.7(b). The background is clearly improved since it is clear, but the wire showed now a random wire shape. A further change of the fabrication procedure, was achieved by optimizing the soft bake timing, the development timing and the spinning speed during development. The final sample is shown in Fig. 3.7(c) which highlights a perfect shape of the wire and a clean background. The sample was finally lifted-off in an HF bath by a special handle tool which minimizes the wire movement. Figure 3.9 shows a fabricated single cell floating in water. The optical microscope image shows the success of the developed fabrication procedure. The fabricated sample is identical to that designed.

3.4. Testing and Characterization.

3.4.1. Testing in water

The fabricated samples were then experimentally tested with the set-up shown in Fig.3.8. Samples were in particular transferred in water to simulate the case in which the auxetic film is applied for tissue regeneration. It is in fact believed that the presence of water represents a more difficult environment from a mechanical prospective. This is because there are additional forces that work against the direction of motion. The major challenge of the sample transition from wafer to the water bath is to make sure that the wires keep the same shape. In addition, it is also critical to avoid undesired stretching which could compromise

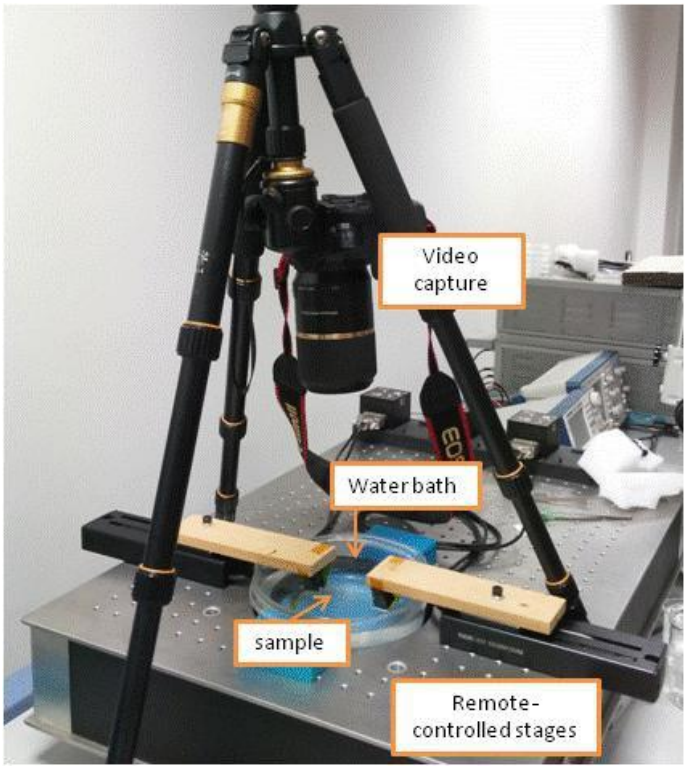

FIG. 3.8. TEST SETUP.

the test data. Figure 3.9 shows a miniaturized cell successfully transferred into the water bath. The two opposite sides of the floating sample were bonded to two movable stages, which were accurately controlled with Thorlabs' Kinesis. The simultaneous and opposite movement of the stages allows the cell stretching. The deformation of the sample during stretching was monitored via a high resolution video camera or with a microscope. The sample was tested in different loading speeds (0.1mm/s-0.5mm/s) and up to 1000 cycles to verify the structural reliability and stability. The video and image data were analysed by Video Tracker. Particular focus was given to tracing the nodes movement during loading/unloading as well as the wires shape. Snap shots of the recorded data are shown in Fig.3.10 and are compared with the corresponding numerical simulations. The images show that the cell expands uniformly according to the expected mechanism. These displacements are transferred to the central node and to the other peripheral nodes (labelled with number 2, 3, 5 and 6) through the interconnected microwires. In addition, the counter clockwise rotation of the central node pushes the transversal peripheral nodes (2,3,5 and 6) which also rotate counter clockwise. Controlled

displacements are applied to the two opposite peripheral nodes labelled with numbers 1 and 4 in Fig. 3.1.

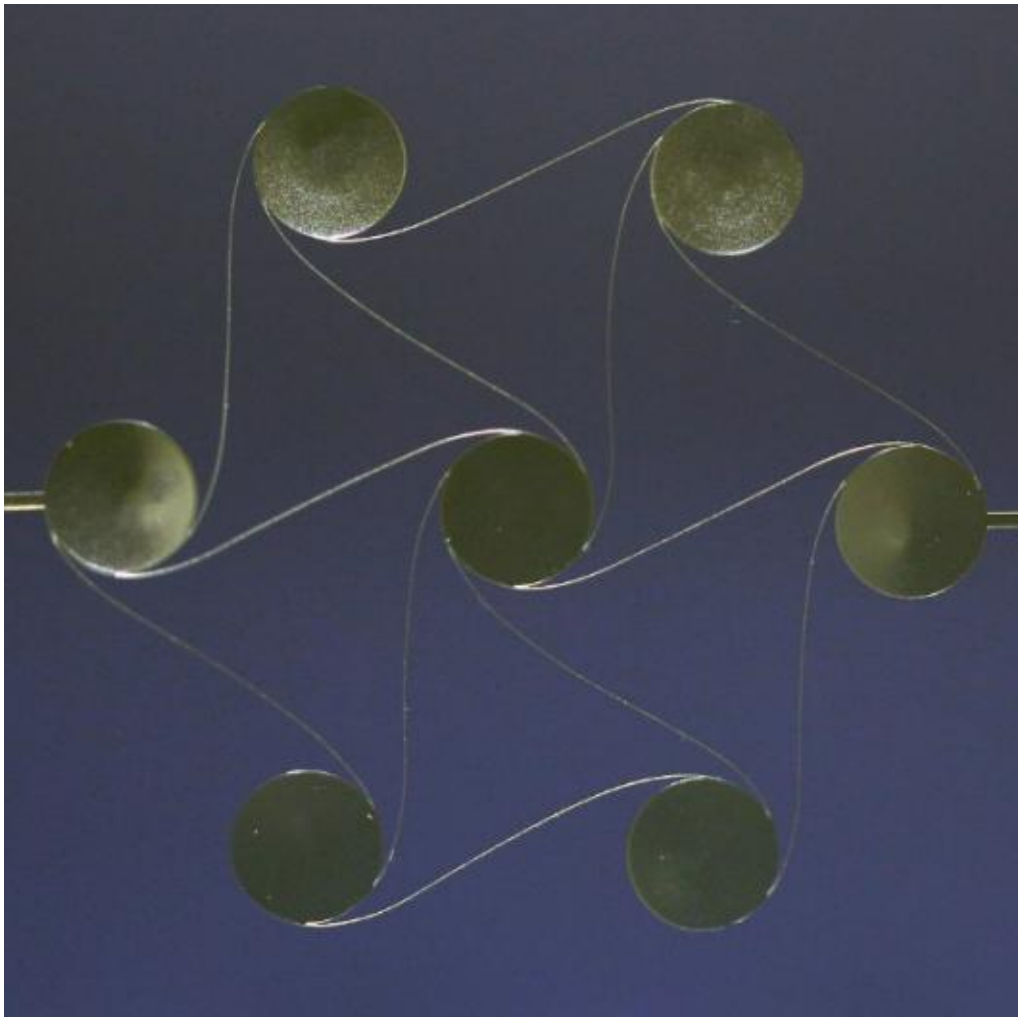

FIG 3.9. LIFTED SAMPLE FLOATING IN WATER

These results clearly show that the cell response is influenced by the loading direction even though all analyzed cases share a similar behaviour profile. The structure starts to expand almost homogenously up to its maximum level and then it fails due to buckling of individual or groups of wires. The buckling failure happens due to the expansion mechanism of the structure. The cell expansion is provided by the central node rotation. Our design is such that the predefined wavy wires provide an even deployment when the applied force is such to induce a clockwise rotation of the central node. This response resembles a “flower” opening. On the other hand, when the applied forces induce a counter clockwise rotation of the central node, the cell shrinks like a "flower"

closing. Therefore, we recognize this mechanism with the "**flower effect**". A quantitative analysis of the cell auxeticity, was also performed. The most common way of classifying auxeticity is through a quantification of the Poisson ratio. The Poisson ratio is defined as the ratio between the transversal deformation and the deformation along the loading direction. But this is true for a continuum material. The use of this definition in the context of discrete materials, as the one treated in this paper, clearly shows some issues. If the Poisson ratio is calculated in agreement with the theoretical definition, then values that are significantly lower than -1 would in fact be reached. This should not be acceptable in a rigorous study because, in agreement with theory, the Poisson values should be comprised between -1 and 0.5 (the theoretical definition would lose its meaning). In addition to the above mentioned loss of meaning because of the discrete cellular design, it is believed that an important contribution to this matter is also given by the specific expansion mechanism. The cell expansion is in fact achieved through the combination of internal deformations and internal rotations (not considered in continuum mechanics theory). To overcome this issue and take into account deformations and rotations, a so called Coefficient of Auxeticity (see equation 3.1), was defined by the authors [1].

$$\nu'_{VH} = -\frac{(\varepsilon_{2,5} + \varepsilon_{3,6})}{2(\varepsilon_{1,4})} \qquad [3.1]$$

The corresponding experimental data that were captured from the videos with the help of Video Tracker are reported in terms of Coefficient of auxeticity vs cell elongation. These analyses comprise cycles performed at different loading speeds (0.1mm/s-0.4mm/s) as well multiple consecutive cycles (up to 1000).

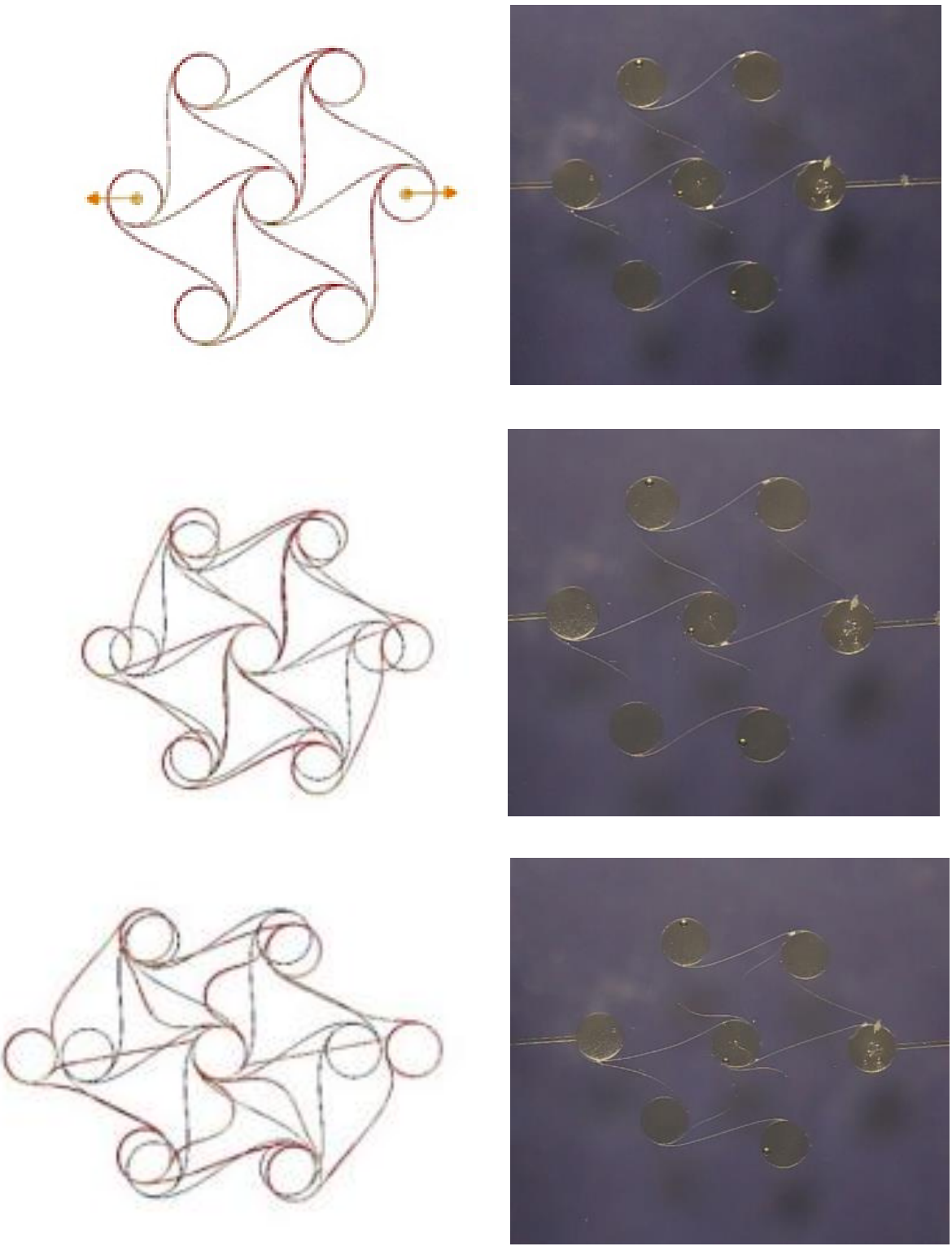

FIG.3.10. EXPERIMENTAL DEFORMATION MECHANISMS OF A SINGLE CELL WHILE BEING STRETCHED: COMPARISON OF THE NUMERICAL AND EXPERIMENTAL MODE SHAPES.

3.4.2. Testing in Air and Loading Speed Effect

Figure 3.11 shows the experimental coefficient of auxeticity of single cell, tested in **air**, with different loading speeds, and its comparison with numerical data (under Comsol simulation whose model is shown in Fig. 3.12). In general, the trends show a smooth increase in coefficient of auxeticity with increasing elongation until reaching a plateau. The experimental data are very similar to each other in terms of trend and coefficient values which highlights that the cellular design is not truly affected by speed variations. However, it is observed that the lowest speed (0.1mm/s) is the only one that presents an initial peak in coefficient of auxeticity. It is believed that this is related to the initial acceleration that in this case is the lowest (from 0.1mm/s to 0.4mm/s under the stretching and un-stretching cycles). Having a lower acceleration implies a lower force that is applied to the center node. Consequently, the expansion effect is delayed. Once this force is great enough to rotate the center node winning the inertia force, the mechanism is immediately activated and leading to the peak. The numerical data show again an excellent agreement. The maximum experimental coefficient of auxeticity is in fact -1.22 while the numerical data is -1.38. This means that the numerical models are reliable for this kind of materials.

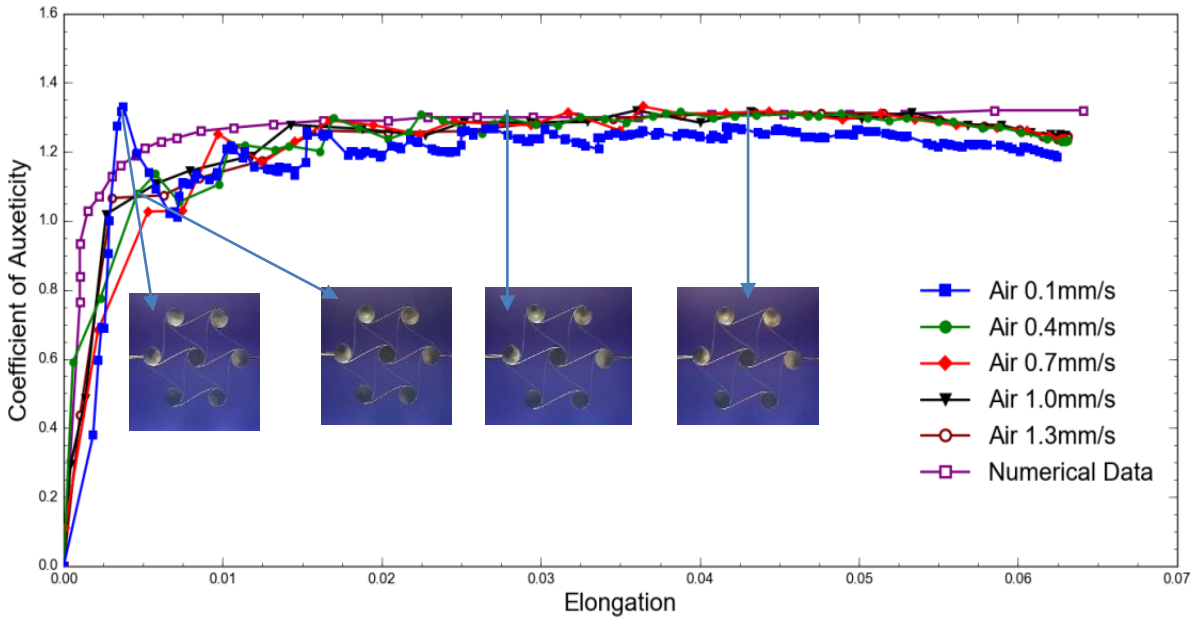

FIG. 3.11. THE RESULTS IN AIR WITH DIFFERENT LOADING SPEEDS: NUMERICAL AND EXPERIMENTAL DATA.

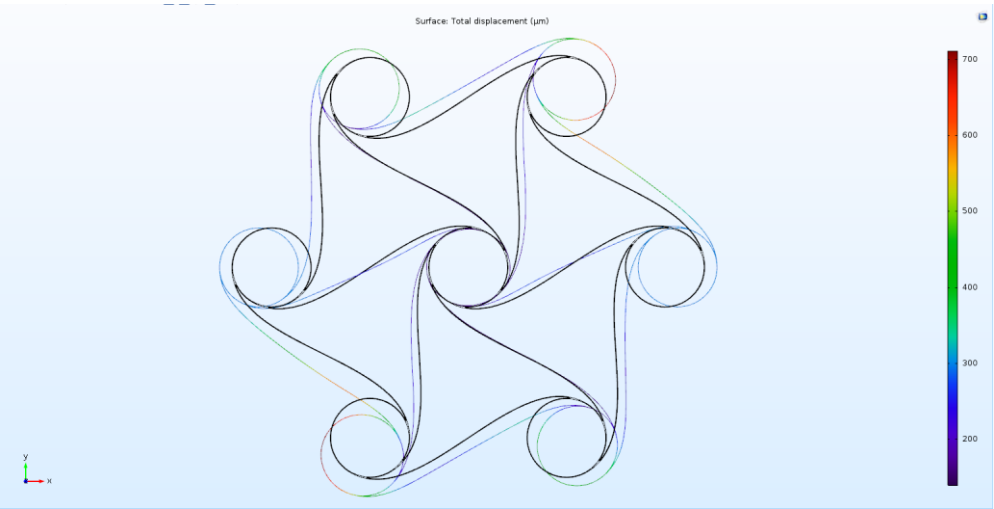

FIG.3.12 COMSOL SIMULATION RESULT AFTER STRETCHING.

3.4.3. Testing in Air: Cyclic Response as Function of Loading Speed

The cyclic response was then investigated to see first the response of the cell within a cycle and then to investigate the microstructure if the response is reproducible under several consecutive loading-unloading cycles (up to 1000 continuous cycles were performed at maximum speed). Figure 3.13 shows the average of 5 cycles under different loading speeds in air. The loading phases show of course the same response discussed in the previous section: rapid and smooth coefficient of auxeticity increase until reaching a plateau with the exception of the slowest loading condition that presents an initial peak for the reasons previously discussed. However, the interesting things are that the response shows a slight hysteresis which appears to be slightly larger for the 0.4 mm/s case. Moreover, in the 0.4mm/s case only a peak appears also during the unloading phase. This is because this speed during stretching is already sufficient enough to overcome inertia and the load applied makes the center node rotate anticlockwise and pushes first the two adjacent wires which expand more in node 3- node 6 direction then the other two wires along the node 2- node 5 direction (see Fig. 3.1 for nodes numbering). But on the way back, the load induces the center node to rotate clockwise which is against the natural rotation of the cell ("flower effect"), so the two wires along the node 2- node 5 direction unstretch first (in time, but with smaller value) while the ones along node 3- node 6 direction unstretch later (in time) but with a bigger value, so, when the pulled nodes

are near to the full unstretching, we have the pick in auxeticity given by the delay in the unstretching of node 3- node 6 direction. This interpretation is proofed with the experimental data reported in Figure 3.14 that shows the elongation profile under stretching and un-stretching cycles for nodes 2-5 and 3-6.

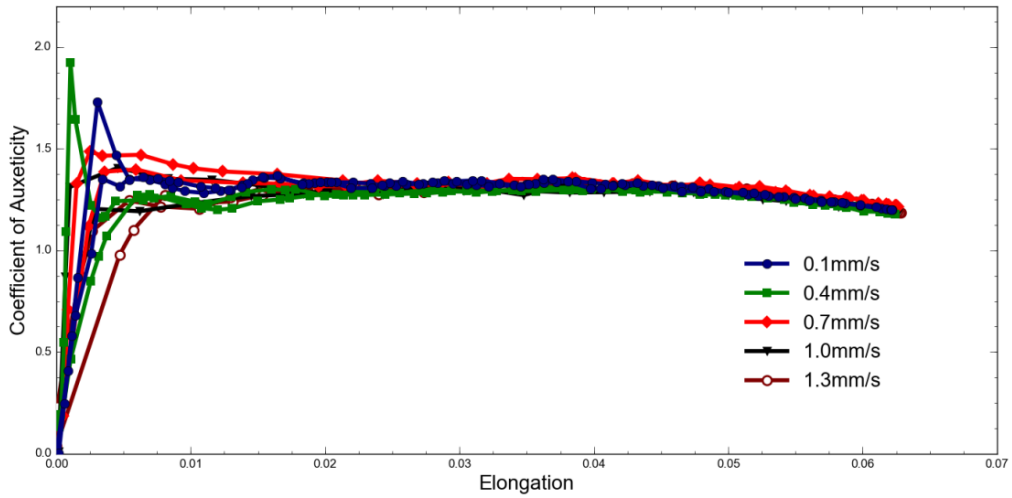

FIG. 3.13. THE ELONGATION PROFILE UNDER STRETCHING AND UN-STRETCHING CYCLES.

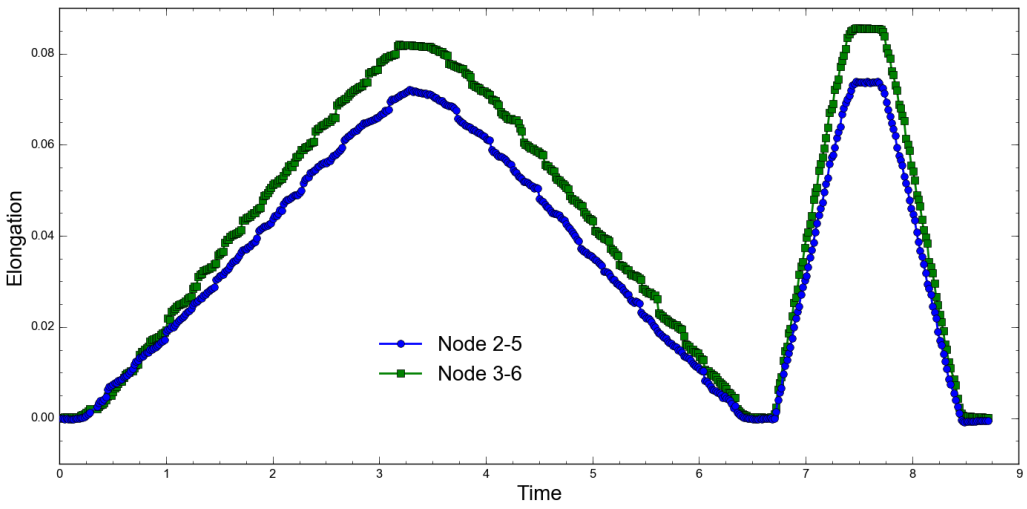

FIG. 3.14. THE ELONGATION PROFILE UNDER STRETCHING AND UN-STRETCHING CYCLES.

3.4.4. Effect of Surface Tension on the microstructure response

The study was extended to different liquids in order to simulate the effect of surface tension on the microstructure response. In particular tests were performed in: air, water and oil, the latter two of

which are characterized by a surface tension of 76 in water and 32 respectively. The results are reported in Figure 3.15. These results show that the coefficient of auxeticity is increasing while the surface tension is decreasing. Moreover, the tests performed in air show the best match with the numerical data. It is also observed that with increasing surface tension the expansion of the cell is smoother as shown by the cancellation of the initial peak (0.1mm/s case) that appears only in air. This is due to a sort of damping effect that the liquid provides to the moving structure.

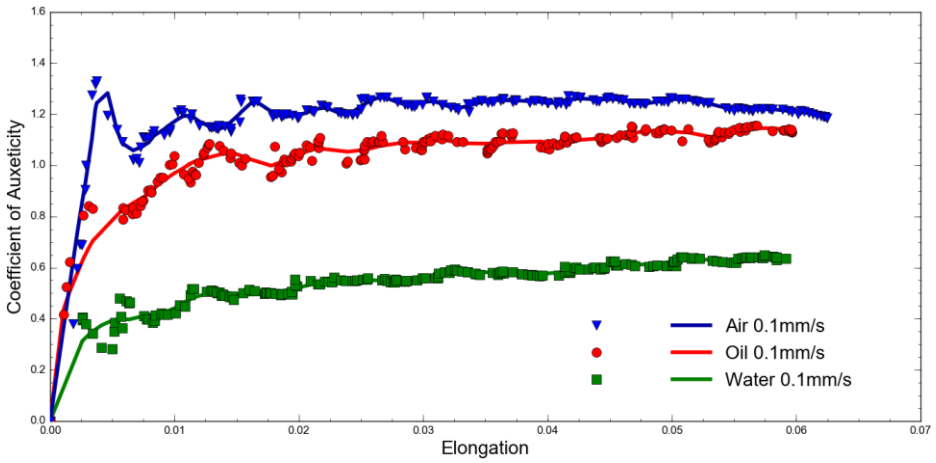

FIG 3.15. THE RESPONSE COMPASSION IN WATER, OIL AND AIR WITH DECREASING SURFACE TENSION.

3.4.5. Microstructural reliability

The cells were also tested up to 1000 loading-unloading cycles to verify the structural reliability and stability. The results are reported in Figure 3.16. In particular, to simplify the graph, the 1st, 200th, 400th, 600th, 800th and 1000th cycles only are here plotted. It is shown that the auxetic cells have a good stability up to 1000 stretching and un-stretching cycles. The slight variations reported in the graph are mostly related to the video capturing software which has a non-negligible error factor.

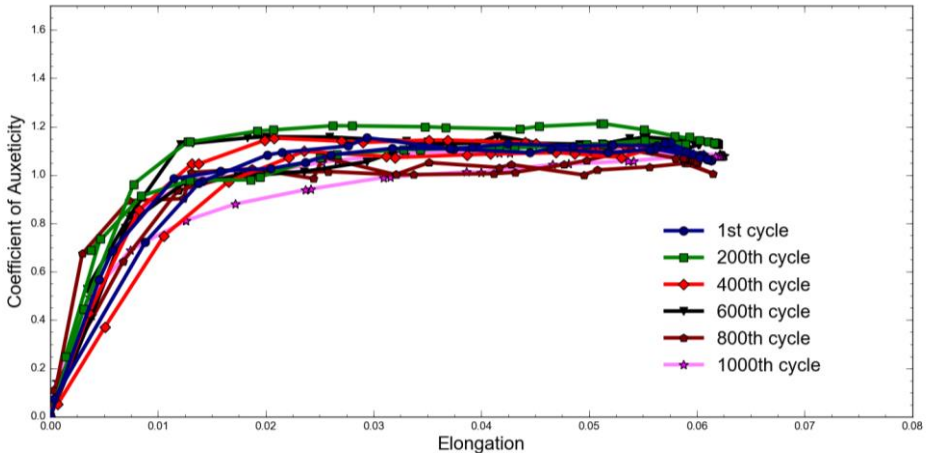

FIG. 3.16. THE 1000 CYCLES TESTING IN AIR

3.4.6. Polyimide-based Microstructured Auxetic Film

The same type of experimental and numerical study was performed in a polymeric film whose cellular structure is formed by a repetition in the xy plane of the already studied cell. The fabricated samples are shown in Figure 3.17 in which also the deformation modes were captured under the optical microscope. It is worth noting that it was not possible to test this sample in air due to strong bending effect with respect of the anchored points. So the study was performed in alcohol that has a low surface tension (23). At a first glance, the film behaviour is qualitatively similar to that of the single cell: after a homogeneous response, buckling of some microwires occurs slowly decreasing the film auxeticity.

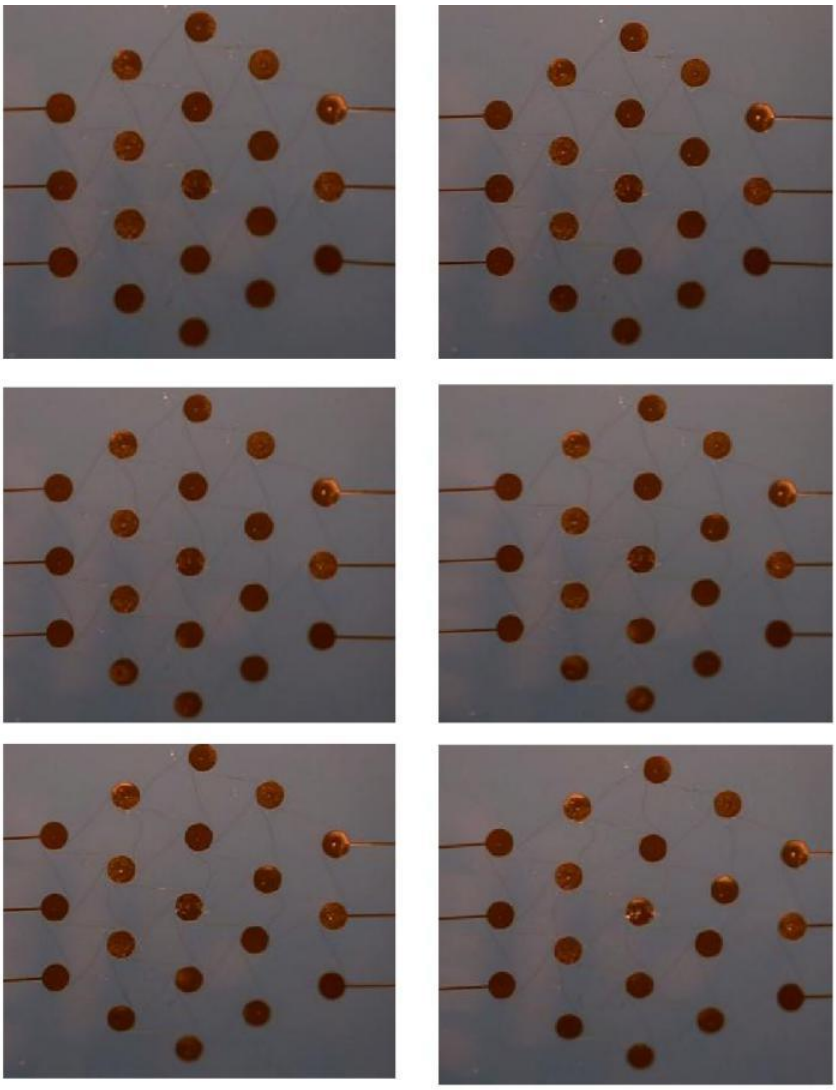

FIG 3.17. EXPERIMENTAL RESPONSE OF A 2D FILM WHILE BEING TESTED.

However, a more careful analysis shows that the single cell because of several direct and indirect effects of node/wire movements into the final response and because a larger array of wires and nodes are placed at a sufficient distance from the boundaries, has a different response. Oppositely, the drawback of the cell study is that a relatively small number of wires and nodes is blocked by the boundary in their movement, thus the overall response might be influenced by the boundary conditions. The combination/interaction of the element movements inside the film makes the response behaviour difficult to be compared with the cell study. Therefore, instead than comparing the film behaviour with the previous single cell study, here an alternative comparison is suggested.

In particular, the film response is compared with the central cell response inside the film to avoid as much as possible the direct influence of the boundary conditions.

On average, the coefficient of Auxeticity values of the central cell are higher than the single cell study but fail at a lower strain range. The reason of such differences is due to the direct boundary effect on the single cell case. Pulling wires make the cell asymmetric and thus prevent its full "homogenous" expansion, however, in the central cell case, pulling nodes are not in direct contact with the cell, therefore they help the cell to expand to its fullest capacity. On the other hand, in the film case, failure happens at lower strain because the load is applied through a looser structure made of wires and nodes surrounding the central cell which make the system less stiff. It is in fact observed that buckling failure happens first in the wires surrounding the peripheral area of the central cell making the whole system to fail.

3.4.7. Microstructured Film in Different Environments

The film was tested in different environments to verify the effect of surface tension on the material response. Figure 3.18 shows stretching in water and alcohol of the full film. These data are also compared with the center cell and with the numerical study for both, the single cell case and the full film. The graph shows clearly that the center cell has a higher coefficient of auxeticity but of course stretches less (which depend on different loading direction, it shows the same stretch in case of 0-degree loading) in the direction of the applied load when compared with the numerical data. At the same time, we also found out the single cell tested in air has a higher coefficient of auxeticity when compared with the film and the center cell, this is due to the high surface tension of water, that is acting against the expansion process, thus the sample's coefficient of auxeticity is limited. Finally, the comparison of the numerical data of the single cell and of the film, show a similar overall behavior than when compared with the single cell and center cell in alcohol, which have the lowest surface tension, so the observed variation what is due to the surface tension.

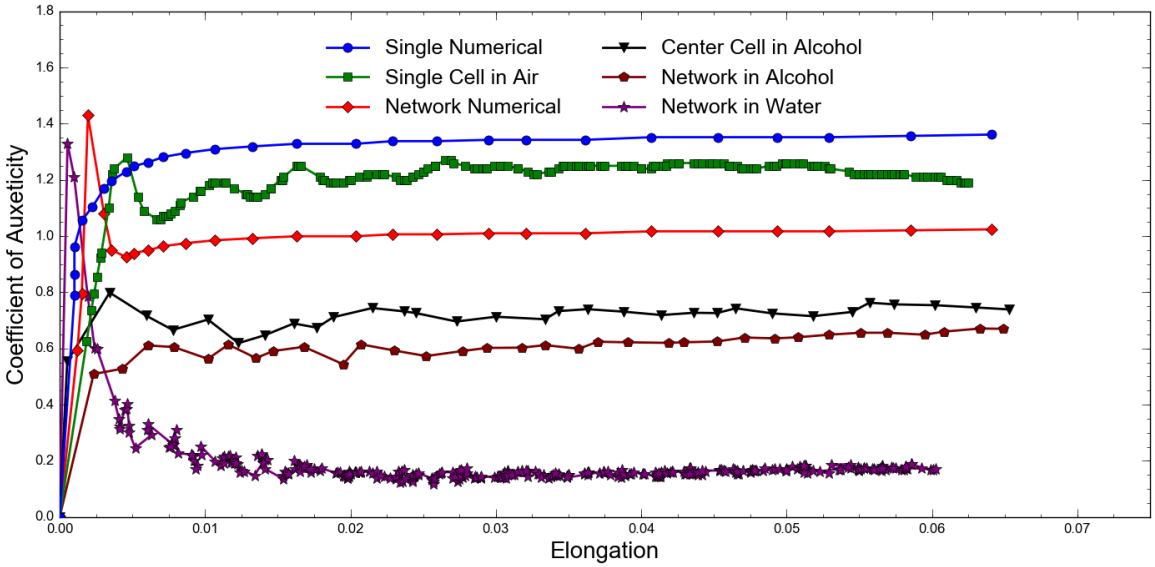

FIG. 3.18. VARIOUS COMPARISON OF EXPERIMENTAL AND NUMERICAL DATA FOR FILMS, SINGLE AND CENTER CELLS.

A direct comparison of the film response in different environments is performed when the film was expanded at 1,3mm/s as shown in Figure 3.19 for the film and Fig. 3.20 for the center cell.

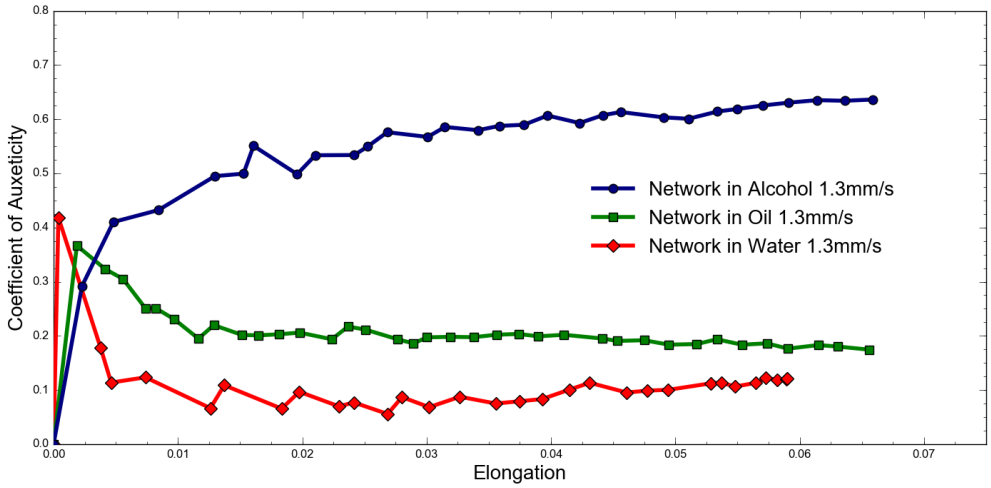

FIG. 3.19. THE NETWORK RESPONSE COMPARISON OF WATER, OIL AND ALCOHOL AT 1.3MM/S

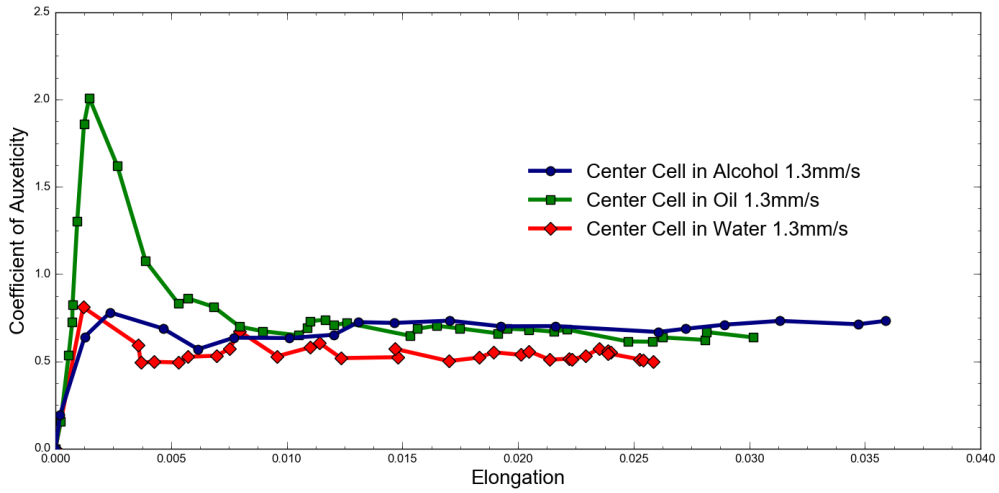

FIG. 3.20. THE CENTER CELL OF NETWORK RESPONSE COMPARISON OF WATER, OIL AND ALCOHOL AT 1.3MM/S

These experimental results show that the film is affected more in its overall response by the different surface tensions. The response in alcohol, that has the lowest surface tension is in fact shown to be the highest of all in terms of coefficient of auxeticity, while testing in water, which has the highest surface tension, shows the worse coefficient of auxeticity. This is fully in agreement with the previous discussions. Moreover, the cell study had shown the absence of an initial peak at a 1.3mm/sec speed when tested in low surface tension (air). This result is again confirmed when comparing the film response in alcohol (low surface tension). However, peaks appear for the oil and water cases. This is due to a sort of stick-slip mechanism that occurs in the wires/nodes while they move away from the direct connection with the side constraints. Surface tension in fact plays the role of a sticking force, once the system wins the sticking force, then the film first shows a peak. The variation between the sticking-release is found to be higher for the higher surface tension (water), and this is in line with the described mechanism.

Interestingly, it is observed in Figure 3.20 that the just described mechanism changes when the center cell of the film is analyzed. The peaks in water and alcohol still appear more or less, but most importantly, the variations in the plateau are no longer so strong when comparing the different surface tensions. This result shows that the surface tension effect becomes less important when we are far away from the boundary area probably because the transfer of load within the interconnected wires and nodes to reach the center cell, acts already as a sort of damping effect which is probably stronger

than the damping effect coming from surface tension. The peak appears in case of fast loading speed in oil which is due the liquid viscosity, the force is related to the stretching speed. This is a very interesting result because, since in general it is expected to work with a much larger number of cells and not with a single cell, then the overall film response is expected not to be influenced meaningfully by the different surface tensions in which it is forced to work during the material in-service life.

3.4.8. Cyclic Film Response at Different Speeds

Figure 3.21 shows the film response for 5 loading-unloading cycles in alcohol at a speed of 0.1mm/s. The response shows a slight hysteretic behaviour which is due to the previously described flower effect and a repeatable response with increasing cycles. An increase in speed to 1.3mm/s (Figure 3.22) increases hysteresis. The increase in hysteresis is most probably related to frictional forces which are higher for higher speeds. These results are very interesting because they highlight that damping effects can be reached not only by using materials whose molecular structure to allow energy dissipation, but dissipation can also be reached playing with the intrinsic mechanisms in the microstructure of films, independently from the molecular arrangement.

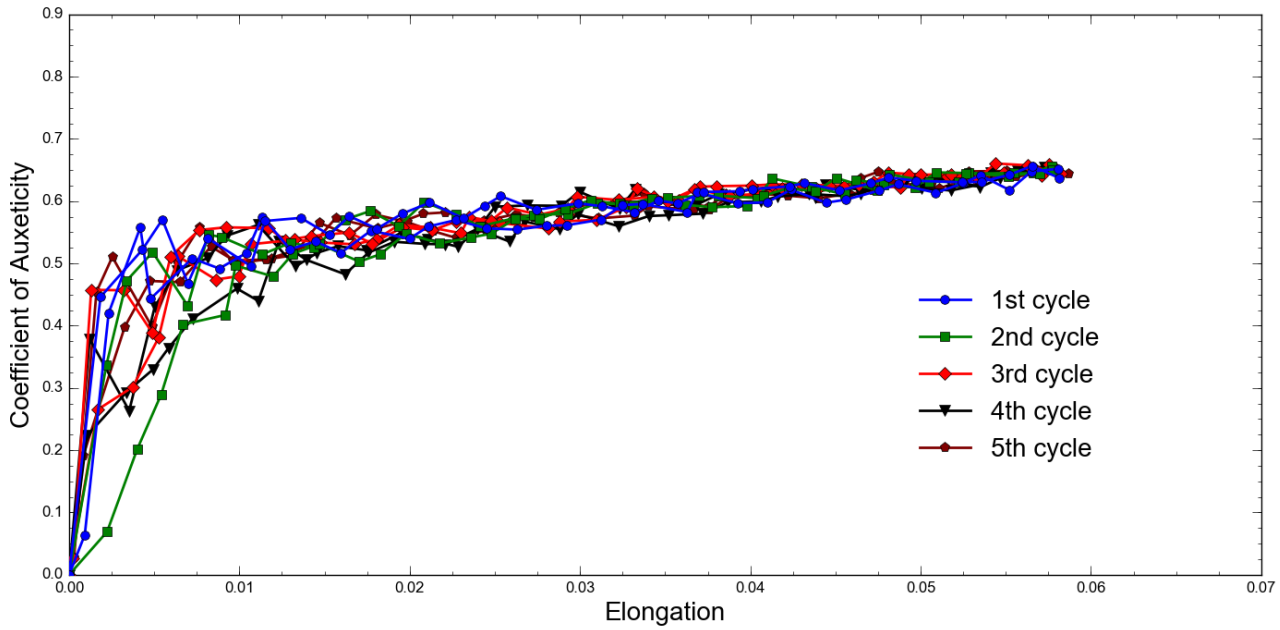

FIG. 3.21. 5 CYCLES IN ALCOHOL FOR THE 0.1MM/S (THE LOWEST LOADING SPEED)

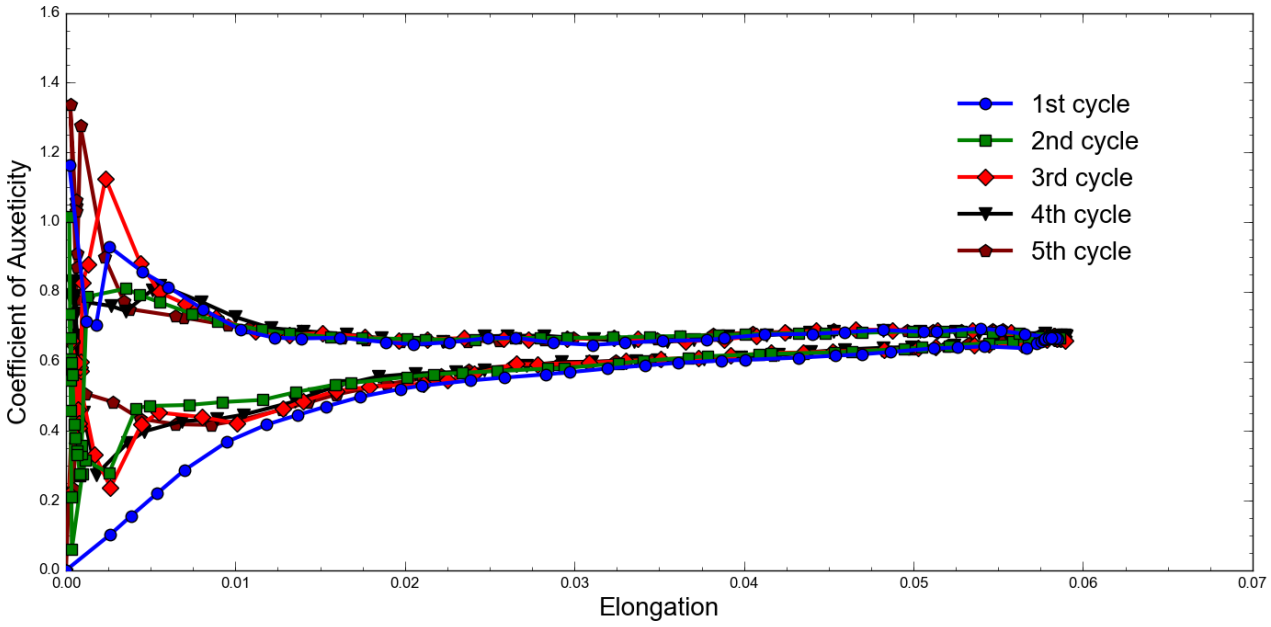

FIG. 3.22. 5 CYCLES IN ALCOHOL FOR THE 1.3MM/S (THE HIGHEST LOADING SPEED)

3.4.9. Failure Mechanism and Material Anisotropy

An important aspect to be investigated is related to the auxetic failure and its mechanism. This is an interesting aspect to be analyzed because auxetic failure is never a discussion reported in the literature. It is worth noting that, the term "failure" here is related to the loss of auxeticity and to to the rupture of the material, Knowing the range of reliability of the auxeticity of a material is an essential aspect.

The combination of all the described mechanisms results into an overall auxetic expansion of the cell. This response goes on until the wires that interconnect the center node with nodes 3 and 6 and later the ones that interconnect nodes 2 and 5, start buckling. This is an expected result due to the slenderness of the microwires whose compression increases with increasing cell expansion. It is clear that once microwires start buckling, the cell auxeticity is gradually lost.

The analysis of the experimental data shows that the cell responds with an auxetic behavior very rapidly once it is loaded. High values of the coefficient of auxeticity are in fact reached for very low elongation values. This interesting auxetic response is kept until microwires start buckling at an

approximate deformation of 0.06. This represents the "auxetic failure" since, with a further elongation increase the auxetic effect is gradually lost as also proven by the numerical analyses (Fig. 3.23). Previous observations showed that, the mechanical response of the cell is fully reversible and is independent on the applied deformation speed. Here we highlight also that reversibility is achieved also after reaching the so called auxetic failure.

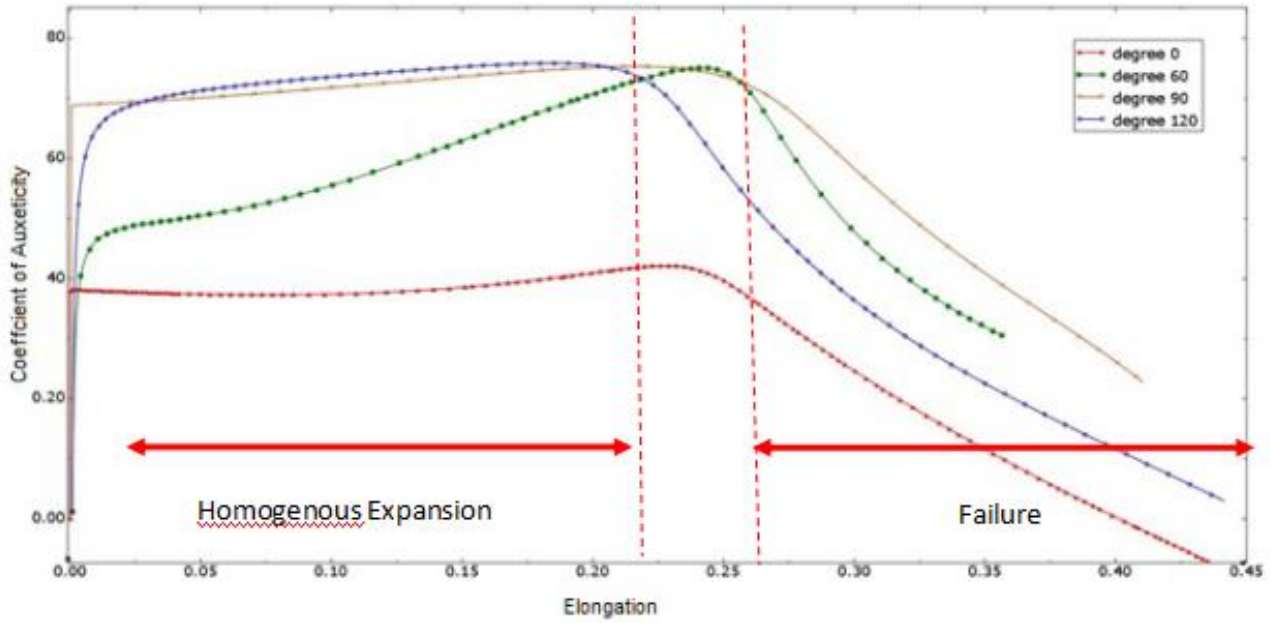

FIG. 3.23: POISSON' S RESPONSE OF DIFFERENT PULLING DIRECTIONS

Figures 3.23 also show that, once the cells are fully (homogenously) expanded, an extra pulling, thus a further node rotation, induces buckling to a specific wire connected to the central node. An accurate analysis of all studied cases, highlighted that buckling always initiates in the wire right next to the one which has been pulled directly. We recognized this phenomenon here as the "Rule of Thumb", which defines the order of buckling failure of the wires within a specific cell. Accordingly, to this rule, the first wire that is prone to buckle, is that right next (anticlockwise direction) to the wire directly loaded by the external force. In figure 3.24 the first buckling wires are highlighted with a red circle.

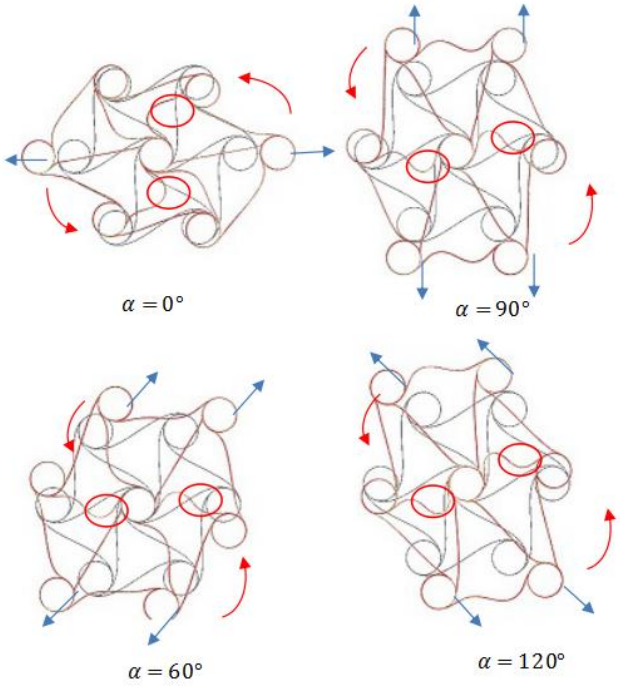

FIG. 3.24: IDENTIFYING THE BUCKLED WIRE BASED ON THE "RULE OF THUMB" IN DIFFERENT PULLING DIRECTIONS

This effect is due to the fact that the pulled wire makes the central node to rotate clockwise and that rotation affects the most the next left adjacent wire directly connected to the node. The loading direction not only affects the auxetic response qualitatively, as depicted above, but also quantitatively. Figure 3.25 shows that the horizontal or the 0°-degrees pulling cases are characterized by the lowest coefficient of auxeticity value. In particular, the auxetic response of the horizontal pulling is around 50% less than that of the vertical case. This important variation in response is linked with the angle β between the force direction and the axis of a wire which is connecting the applied pulling node to the central node. Figure 28 shows that in the horizontal case this angle is $\beta \approx 33°$, whereas in the vertical case β is nearly zero. This wire inclination vs loading direction in the horizontal pulling, causes the loss of part of the pulling force that is first consumed for the wire alignment, weakening the overall expansion response.

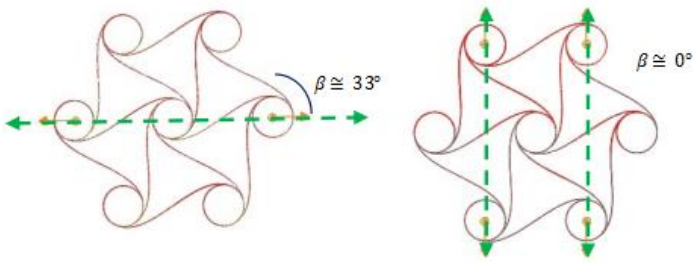

FIG. 3.25: COMPARING THE $\boldsymbol{\beta}$ ANGLE IN VERTICAL AND HORIZONTAL CASES

Finally, the horizontal pulling is also penalized (weakest response) by the fact that it is the only case in which two nodes only, instead than four, are directly pulled. The vertical case (90° pulling) describes the most stable and optimum configuration. In this case one paired nodes are pulled at each side. This obviously enhances the stability of the system. Moreover, as discussed above, the pulling direction is almost aligned with the pulled wire which improves the response. Therefore, a fully steady auxetic response of 0.7 is provided by pulling the cell up to 28% elongation. This configuration is able to keep its auxetic property to the largest level of elongation if compared to all other analyzed cases, with the exception of the 120°- degree configuration that is capable to deliver the largest auxeticity value with the drawback of a smaller elongation level. The failure of the vertical case, according to the "rule of thumb" happens when the two horizontal nodes start to buckle.

The configurations show in Fig. 3.26 represent two special cases because of the orientation of the nodes with respect to the pulling direction. In both cases, the pulling forces are applied on two pair of nodes (up and down) and, since the direction of one pair force is not passing through the center of the cell, a momentum, thus a rotation of the cell is developed. Figure 3.26 shows that the one pair nodal force (green arrows) are applied on the nodes in such a way that the direction passes through the center of the cell whereas the other pair force (red arrows) direction is not passing via the central node and that causes the momentum.

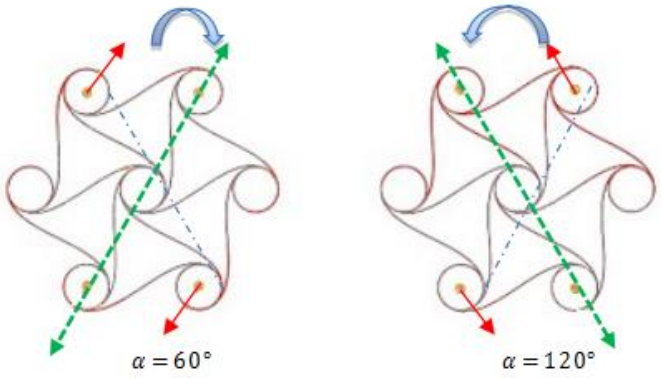

FIG. 3.26: ROTATION DIRECTION IN PULLED WIRES OF 60° AND 120° CASES. GREEN ARROW SHOWS THE FORCE DIRECTION PASSING THROUGH THE CENTER OF THE CELL WHEREAS THE RED ARROWS SHOW FORCES THAT CAUSE THE MOMENTUM TO THE CELL. THE BLUE ARROW SHOWS THE MOMENTUM DIRECTION.

Both configurations in figure 3.26 are affected by this initial momentum. The 60° case is the most unstable case with nonlinear auxetic response. This unstable behaviour is due to the momentum direction which is in contrast with the natural central node deployment rotation (referring to the "flower effect"). As we have discussed before, the flower effect is based on the ability of the structure to fold or unfold by clockwise or counter clockwise rotation of the central node, respectively. The 60° configuration in Figure 80, pulling of the paired nodes indicated with red arrows, causes the nodes to rotate clockwise which is in opposition of the anticlockwise rotation that the cell has to perform so as to expand, therefore it makes the system unstable and nonlinear. On the other hand, in the 120° case, pulling the paired nodes (red arrows) are in the favour of central node rotation and the full cell expansion, therefore, the response indicates the highest value for the auxetic behaviour among all. Nevertheless, in the 120° pulling case, the internal wire buckles earlier than the vertical pulling case because of the instability caused by the momentum effect. In conclusion, as previously indicated, overall, the most stable and meaningful auxetic response of the proposed cell design is achieved for 120° characterized by a 90° degree pulling direction. The minimum auxetic response is reached when the structure pulls in the horizontal direction. The arbitrary pulling directions between 0 to 90 degrees, here represented by 60°, represent the most unstable cases due to the effect of momentum in contrast with the flower effect,

and between 90 to 180 degrees, here represented by 120°, are stable, provide the largest auxeticity values, but buckle at smaller deformation ranges, because of the excessive instability of the momentum effect in the larger strains.

The numerical data in Figure 3.27 are compared with the experimental data in Figure 3.28, both of which refer to single cells cases tested in different loading directions including 0°, 60°, 90° and 120°. The numerical data show that the max Poisson ratio is provided along 90 degrees and the min Poisson ratio is 0 degree, but the experimental data show that the max Poisson ratio is achieved at 0° and the minimum Poisson ratio is at 60°, before failure. This huge difference is due to the testing method in which just one node in each side is directly bonded to the movable stage in the 0° case, and there are two nodes directly connected to the stage for samples: 60°, 90° and 120°. The two bonding nodes apply an internal constrain during stretching and un-stretching and this influences meaningfully the overall result. To proof this concept, we can focus on the 60°, 90° and 120° loading trends. The comparison of the experimental and numerical data show very similar trends. For instance, the 120° and 60° trends cross each other before the buckling where the Poisson ratio is decreasing, and also the 90° and 120° trends have similar shapes.

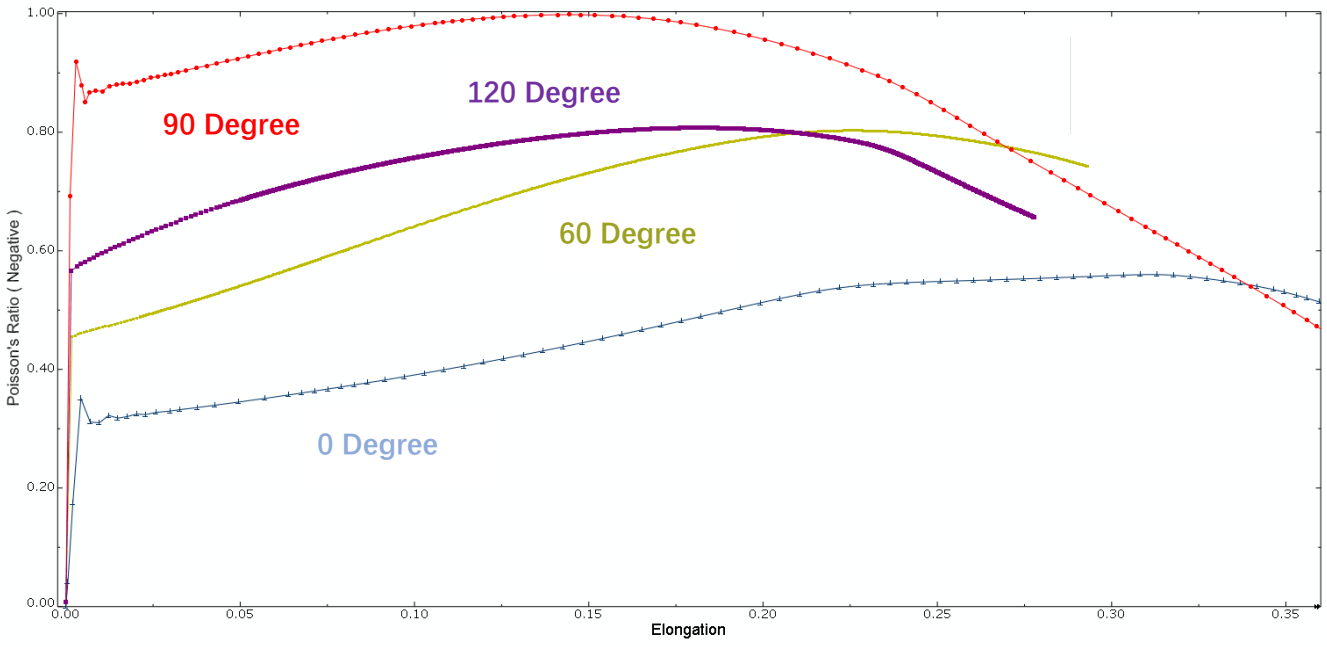

FIG. 3.27:POISSON' S RESPONSE OF DIFFERENT PULLING DIRECTIONS – NUMERICAL DATA

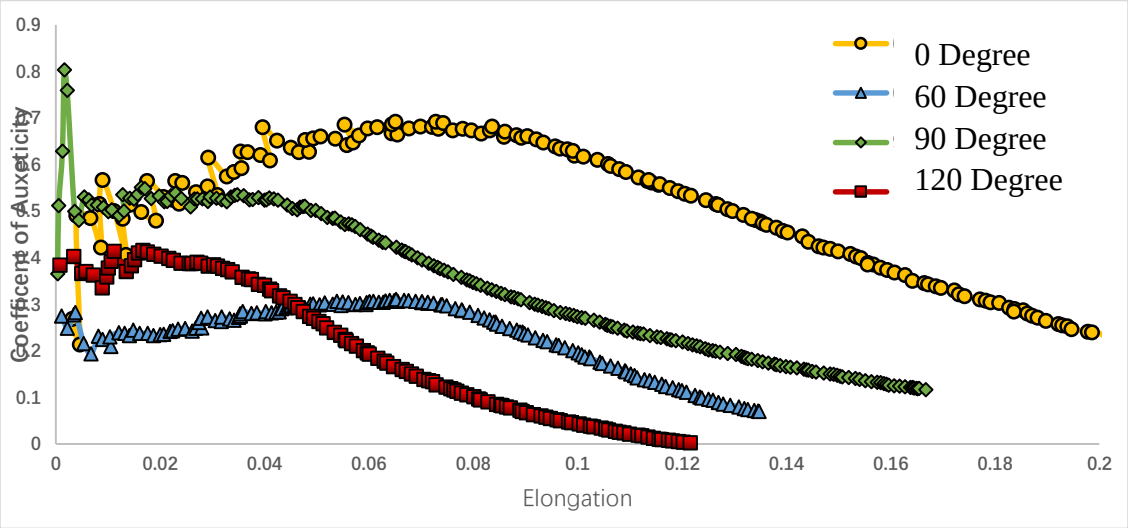

FIG. 3.28: POISSON' S RESPONSE OF DIFFERENT PULLING DIRECTIONS – EXPERIMENTAL DATA

The numerical study of this part of the work was performed with ABAQUS in close collaboration with Kaveh Samadikhah [1].

3.4.10. High Expandable Auxetic Film

The novel designs presented in section 3.2.3 to enhance stretching capability of an auxetic film have also been experimentally characterized. These designs are such that the cell is initially rolled and then it unrolls by expanding in all directions uniformly. We analyzed two different designs, the first one is named "partially rolled" (Fig. 3.29) because a straight segment connects the wires that are rolled around the nodes. The result reported in the figure represents the case in which the sample is being tested in the vertical direction. The sample is expanding uniformly in all directions as a proof of the auxetic response. This uniform expansion goes on until some wires buckle reducing the auxetic effect. The cell was fully recovered to the initial configuration. And the response is repeatable at different speeds for several cycles. The auxetic stretching capability of the partially rolled samples is 37.5%, which represents an improvement over 35% if compared with the previously discussed modified hexachriral structure.

The other designed in named " fully rolled" since the wires are fully rolled around the nodes, as shown in Figure 3.30. This wire design allows an overall 50% in stretching capability. As in the previous case, the auxetic response goes on until buckling is reached in some microwires.

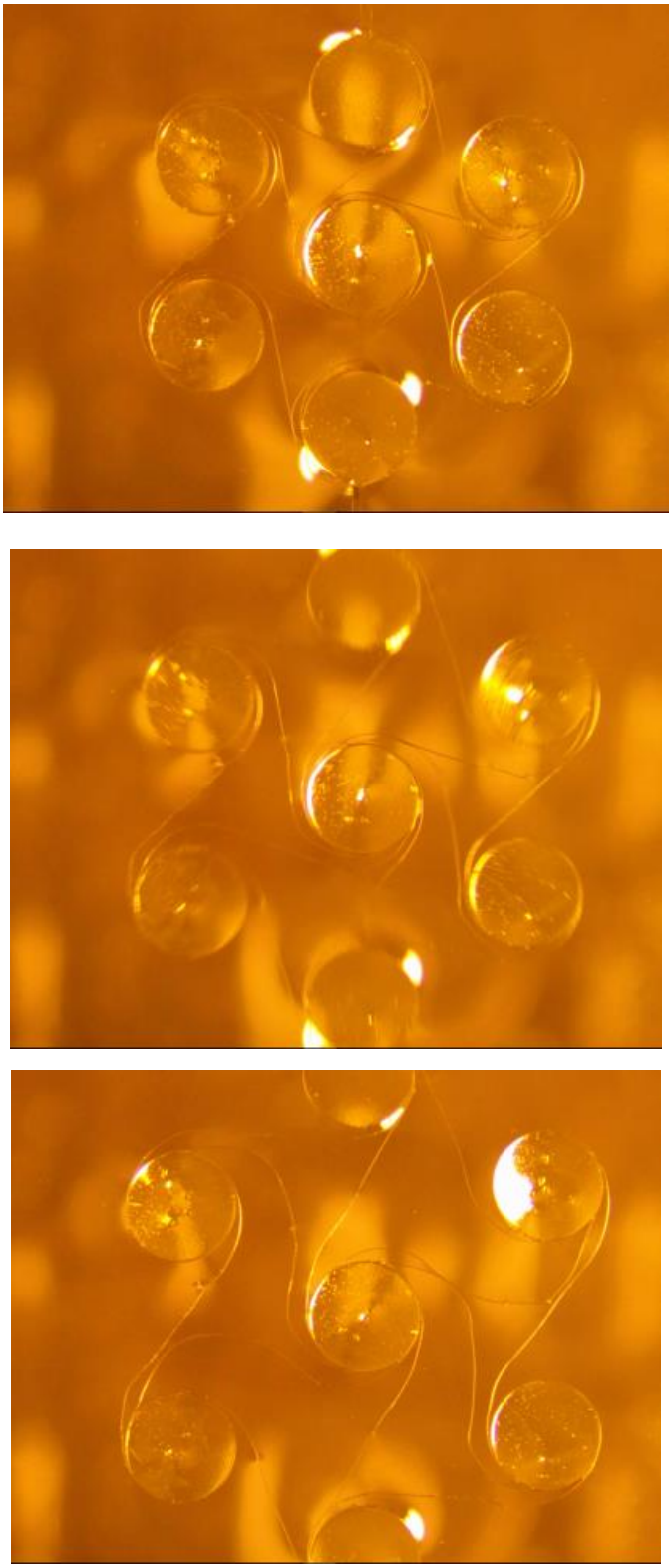

FIG. 3.29. EXPERIMENTAL TESTING OF A "PARTIALLY ROLLED" DEISGN. OPTICAL MICROSCOPE IMAGES.

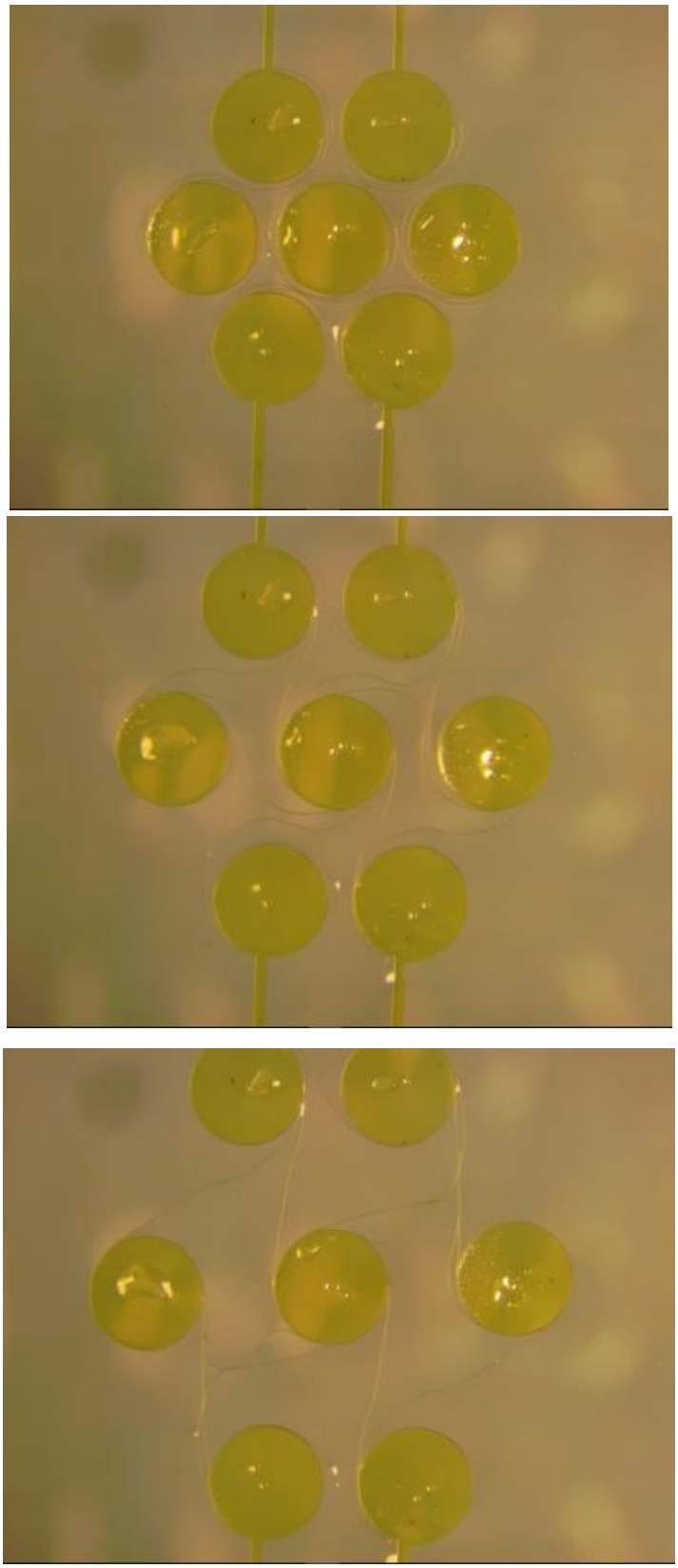

FIG. 3.30. EXPERIMENTAL TESTING OF A "FULLY ROLLED" DESIGN. OPTICAL MICROSCOPE IMAGES.

3.5. Reference

1. Samadikhah K. and Lanzara G., 2015, "Can Micro-Chiral Cellular Structures Be Auxetic?", ASME 2015 International Design Engineering Technical Conferences and Computers and Information in Engineering Conference, Vol. 4: 20th Design for Manufacturing and the Life Cycle Conference; 9th International Conference on Micro- and Nanosystems, Boston, Massachusetts, USA, August 2–5, 2015, Paper No. DETC2015-47771, pp. V004T09A020, doi:10.1115/DETC2015-47771

Chapter 4

Moving Towards the Use of Temperature Mismatches for Morphing Materials: A Preliminary Assessment

In this chapter a preliminary work was performed toward the realization of temperature driven morphing materials. Our interest in this case was to grab mismatches in coefficient of thermal expansion within the layers of a multilayer system in order to drive morphing, instead than exploiting changes or phase transformations of the material molecular structure when temperature reaches specific critical values. In brief, it is well known that variations in coefficient of thermal expansions between adjacent materials can cause the formation of internal stresses thus to global deformations, but this is typically seen negatively because such internal stresses can be the cause of damage initiation in a structure. The deformation ranges that are typically reached for this issue are quite low (just a few %) which is not compatible with morphing applications. As previously discussed, in fact, morphing requires typically a change in shape, given clearly by a global material deformation, that is significant, so significant to be clearly viewable by naked eyes. A preliminary assessment was then performed, and reported in this chapter. The objective was to understand the

limits, key aspects and eventually the advantages of using a multilayer system to make morphing materials driven by temperature, in which each layer responds differently when exposed to temperature gradients.

4.1. State-of-the-art of temperature driven morphing materials

The temperature mismatches were a traditional issue for multilayer systems, since they can generate internal stresses between different layers. A lot of studies were done to avoid temperature mismatch between materials in order to avoid the devices failure [1]. In recent years, some works started using temperature mismatches for morphing materials that can self-actuate by means of temperature, humidity and other environmental conditions. Christine and Jian [2] worked on a shape-morphing nanocomposite which is able to repeatedly and reversibly transform shape (fold and un-fold) in response to variations in environmental temperature and humidity. This is possible thanks to the materials properties, one material (LBL PEMs) can swell base on humidity and another material (PNTE) can be deformed due to temperature changes. There are some limitations in this study. First of all the reversible mechanisms can only be activated by both temperature (fold) and humidity (unfold), which means it can be only applied to devices that work in a controllable humidity environment. This makes it impossible to use this material in biological systems such as stents and implant devices. Then this nanocomposite material can only have the fold and un-fold movements, which means that it has a limited number of shape changes. Also, the response speed is up to 20s which is relatively slow.

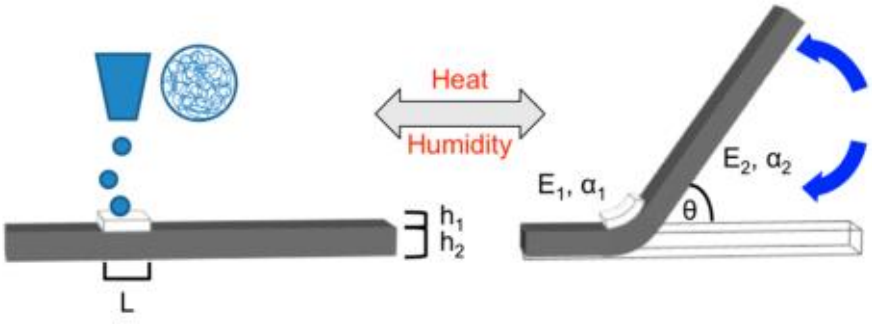

FIG. 4.1.SCHEMATIC OF THE $(PU/CNT)_{200}$ STRIP WITH INKJET-DEPOSITED $(PDDA_2/PSS_2)_{10}$. WHEN EXPOSED TO HUMIDITY AND TEMPERATURE STIMULI, THE BIMORPH RESPONDS BY BENDING, CREATING AN ANGLE OF DEFLECTION OF Θ IN THE LONGER ARM. HERE, Θ DEPENDS ON THE THICKNESS (H), STIFFNESS (E), AND EXPANSION COEFFICIENT (A) OF EACH LAYER, ALONG WITH THE TOTAL LENGTH OF THE BIMORPH (L) [2].

Another study was done by Athanasopoulos and Siakavellas which investigated a novel multi-layer material that consists of carbon fibre reinforce epoxy composite and aluminium foil that can morph during the temperature changes by taking inspiration from Mimosa. This is possible thanks to the materials which have different coefficient of thermal expansion. The CTE mismatch between the two materials creates shape memory effect which alter their shape via the developed internal stresses while temperature changing. The limitations of this study include limited shape changes since it can only have close and open up movements, slow response speed which up to 600s and far away from a continuum material [3].

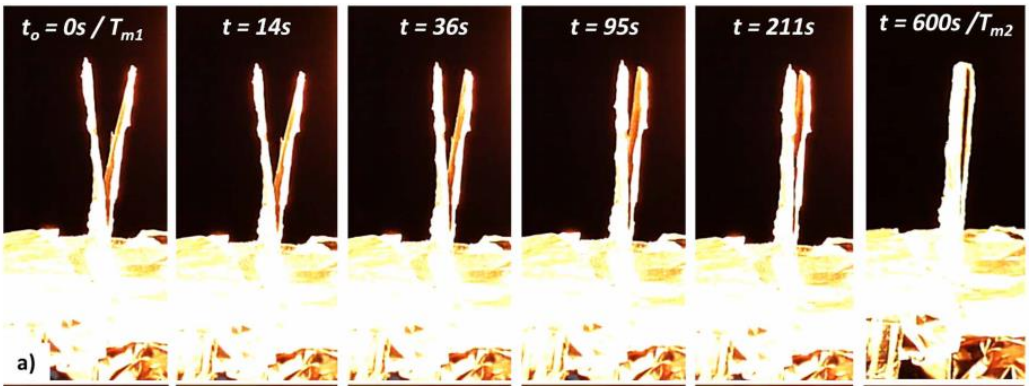

FIG. 4.2. ISO-VIEW OF THE VARIABLE EMITTANCE SELF-SHAPE STRUCTURE (TM1≈ 20 °C, TM2= 145 °C) [3].

Eckstein and Lamacchia [4] investigated a fibre-metal laminate shell, which achieves thermally driven snap-through behaviours. This is achieved by orienting unidirectional, low expansion carbon fibres perpendicular to the direction of the initial curvature (which is stress-free). Due to the different coefficient of thermal expansion between the fibres and the metal, internal stresses grow while temperature changes. This internal stress leads the snap through movement from the initial configuration to another stable configuration via an unstable, non-smooth manner. This composite material only has two stable shape which the initial shape need to be programmed before the material is cured. So the major limitation of this material is that it only has two stable deformed shapes in total as in shape memory polymers. Also the initial curvature needs extra loading to be produced otherwise it will not have the snap-through behaviour.

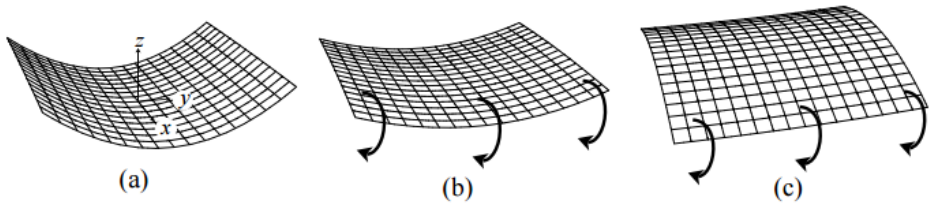

FIG. 4.3. RESPONSE OF CURVED SHELL TO APPLIED INTERNAL BENDING MOMENT PERPENDICULAR TO INITIAL CURVATURE DIRECTION [4].

One more thermally-responsive programmable material was developed by Zhang and Pint [5] which is based on the carbon nanotube-hydrogel polymer composite. In this study they produced a thermal actuator, made by a single-walled carbon nanotubes (SWNT)- poly(N-isopropylacrylamide) (pNIPAM) composite hydrogel. A hinge can fold up to 180° due to the abrupt strain change in the polymer hydrogel above the lower critical solution temperature which is between 32°C -33°C, thanks to the mismatch of coefficient of thermal expansion. The cube can be closed at 48°C in water within 35sec, and open up once the temperature cools down in 256sec. This study has the potential to have more than one deformed shape by playing with the location of thermal actuator, but needs to be pre-designed. The working temperature of this thermal actuator is under 60°C due to the hydrogel properties, which is typically used into biological environmental. As other materials, the response time that is similar to shape memory polymers, is slow if compared with piezoelectric materials.

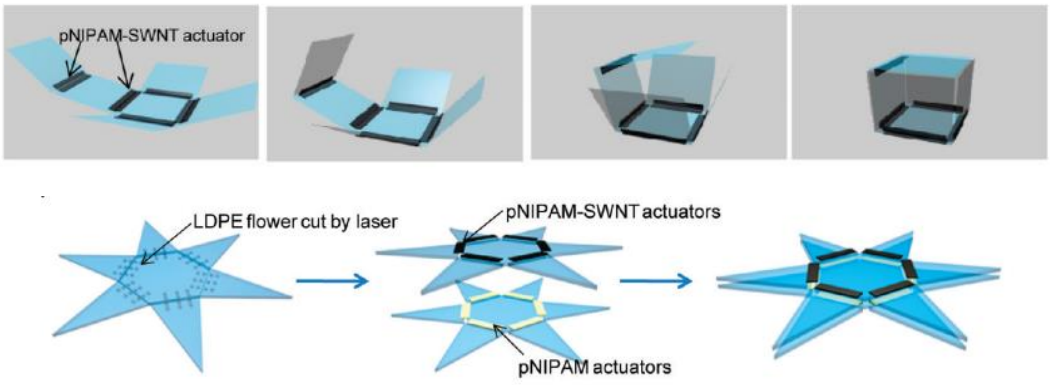

FIG. 4.4. PROGRAMMABLE CUBES AND FLOWER BASED ON THERMAL RESPONSIVE ACTUATORS [5].

According to the mentioned limitations, we design a novel multi-layer morphing material which can pass through these limitations such as limited number of shape changing, slow response as well as, in some cases, loss of rigidity.

4.2. Theoretical Study of Thermal Effects in Elastic Multilayer Systems

As mentioned in section 4.1, mismatches in coefficient of thermal expansion in a multilayer system induce thermal stresses between the layers which lead to a global bending effect. This problem can be easily viewed through the schematic in Figure 4.5 [6] in which the case of an elastic multilayer system (Figure 4.5) formed by *n* layers bonded to a substrate (of thickness t_s), each of which characterized by a specific thickness t_i (where *i* varies between *1* and *n*), is represented. If the layers are free-to-move one with respect to the other (Figure 4.5b), they will elongate independently and will present a different degree of elongation in agreement with their coefficient of thermal expansion (CTE) and with the given temperature gradient ΔT according to the equations:

$$\varepsilon_i = \alpha_i \Delta T \qquad (1)$$

$$\varepsilon_s = \alpha_s \Delta T \qquad (2)$$

However, if the layers are constrained among them, they should elongate of the same amount (displacement compatibility): $\varepsilon_i = \varepsilon_s$ (Figure 4.5c) and this leads to asymmetric stresses, thus to bending (Figure 4.5d). With this in mind, the strain ε in the multilayer can be decomposed into a uniform component, *c*, and a bending component. Fixing the coordinate system in such a way that the interface between the substrate and layer 1 of the film is located at $z=0$, then the substrate's free surface is located at $z=-ts$, the upper surface of the outer-most layer is located at $z=hn$, and the interface between layers *i* and *i*+1 is located at *hi*. In this way, the relation between h_i and t_i can be described as

$$h_i = \sum_{j=1}^{i} t_j (i = 1 \ \ to \ \ n) \quad (3)$$

It can be analytically demonstrated (see Ref. [6]) that the amount of bending, thus of resulting curvature, depends on the thickness, modulus and coefficient of thermal expansion of the films that form the multilayer system according to the following key equations:

$$\frac{1}{r} = \frac{3\left[E_s(c-\alpha_s\Delta T)t_s^2 - \sum_{i=1}^{n} E_i t_i (c-\alpha_i \Delta T)(2h_{i-1}+t_i)\right]}{E_s t_s^2 (2t_s + 3t_b) + \sum_{i=1}^{n} E_i t_i \left[6h_{i-1}^2 + 6h_{i-1}t_i + 2t_i^2 - 3t_b(2h_{i-1}+t_i)\right]} \quad (4)$$

$$c = \frac{\left(E_s t_s \alpha_s + \sum_{i=1}^{n} E_i t_i \alpha_i\right)\Delta T}{E_s t_s + \sum_{i=1}^{n} E_i t_i} \quad (5)$$

$$t_b = \frac{-E_s t_s^2 + \sum_{i=1}^{n} E_i t_i (2h_{i-1}+t_i)}{2(E_s t_s + \sum_{i=1}^{n} E_i t_i)} \quad (6)$$

Where E_s and E_i are the Young's modulus of the substrate and of the layers respectively, α_s and α_i are the thermal expansion coefficients of the substrate and layers and *1/r* is the curvature.

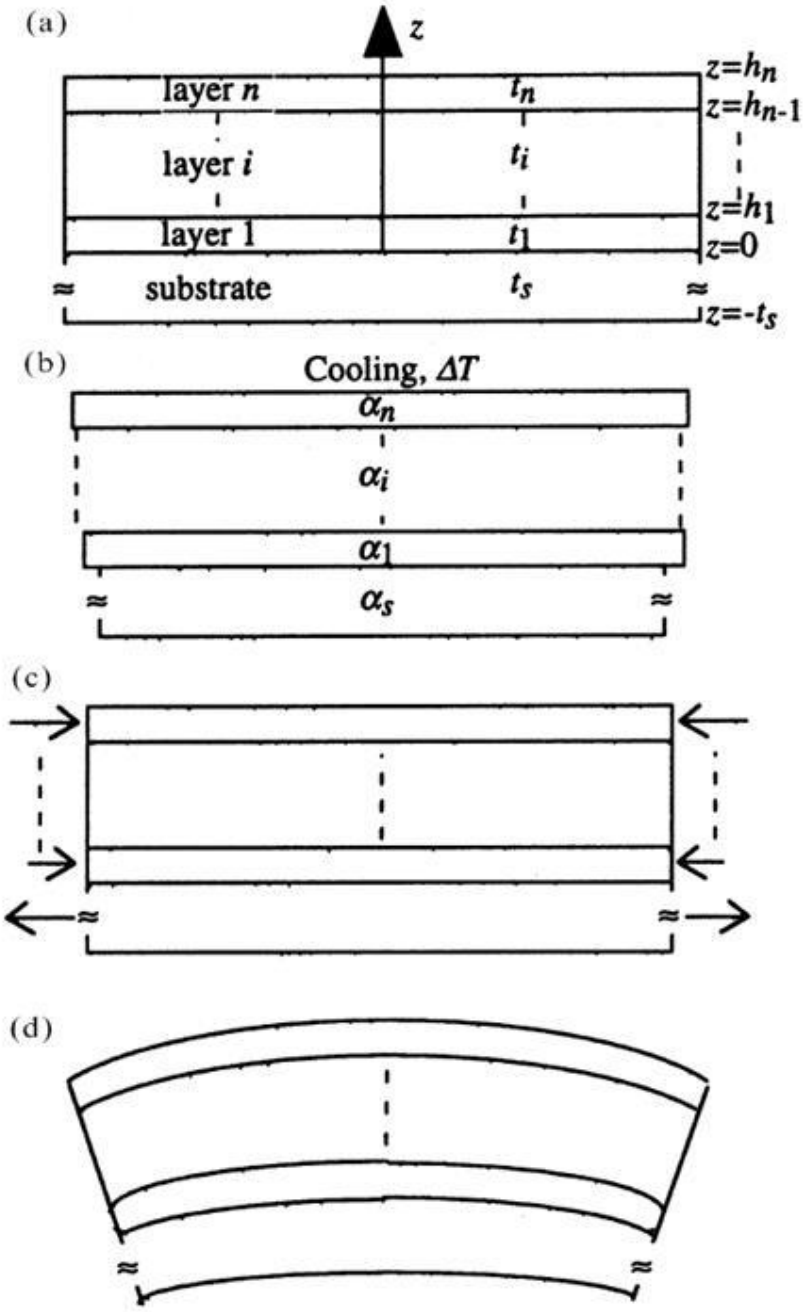

FIG. 4.5. BENDING OF A MULTILAYER BEAM DUE TO THERMAL STRESSES: (A) STRESS-FREE CONDITION; (B)UNCONSTRAINED STRAINS DUE TO A TEMPERATURE CHANGE T; (C) CONSTRAINED STRAIN FOR DISPLACEMENT COMPATIBILITY; (D) BENDING INDUCED BY ASYMMETRIC STRESSES. BY COURTESY OF [6].

4.3. Comparing Theoretical and Numerical Predictions in Bilayers

Complex material designs which can hardly be modelled with a theoretical approach, could benefit from the use of numerical studies. The reliability of the numerical models is a key aspect and needs to be addressed carefully before moving towards complexity. For this reason, the theoretical model described in section 4.2. was used to verify the numerical predictions of the simplest possible multilayer system: a "Bilayer" system which was modelled with the Thermomechanical package of Comsol Multiphysics using the 3D model, solid mechanics, heat transfer in solids, stationary and time dependent studies. Figure 4.6 shows the two layers model that was implemented in Comsol. The substrate layer was chosen to be glass fiber reinforced polycarbonate while the second layer was polycarbonate, which have different mechanical and thermal properties as shown in table 4.1. The length of the beam was 500mm, while the width and the total thickness of the bilayer were of 100mm and 20mm, respectively. The beam was fully constrained at one end forming a cantilever and the temperature gradient was imposed to be ΔT = 120℃-20℃. The analysis was repeated by changing the substrate thickness and consequently modifying the layer thickness in order to keep constant the total bilayer thickness. Both curvatures and percentage of deformation (given by the maximum beam displacement and the beam length) were then calculated starting from the numerical data by Equation 4-6, which take account the thickness, Young's modulus, CTE of these layer.

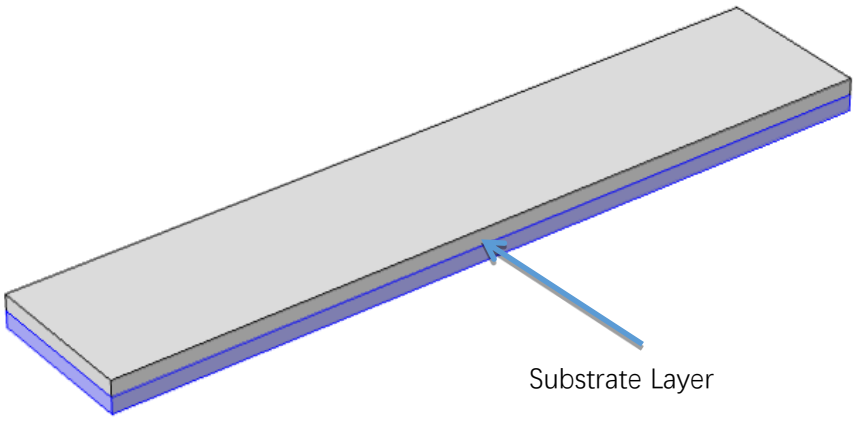

FIG. 4.6: COMSOL MODEL OF THE BILAYER.

TABLE 4.1: THERMAL AND MECHANICAL SPECIFICATIONS OF 2 LAYER COMPOSITE MATERIALS.

Quantities	Symbols	Dimensions	Polycarbonate	Reinforced Polycarbonate
Heat capacity	C	J/(kg*K)	1200	1080
Young's modulus	E	Pa	$2.4e^{9}$	$7.9e^{9}$
Thermal expansion coeff.	A	1/K	$70e^{-6}$	$23e^{-6}$
Poisson ratio	ν		0.37	0.37
Thermal conductivity	K	W/(m*K)	0.22	0.26
Density	Rho	kg/m^3	1.22	1.42

The resulting data in terms of curvature, were compared with the theoretical predictions using equations Eqs. (3)-(6) [6] described in section 4.2 (see Figure. 4.5). According to the equations of multilayer system curvature, the factors which affect the result are the difference of temperature, Young's modulus, thickness and thermal expansion coefficient of each layer. Assume that difference of temperature,

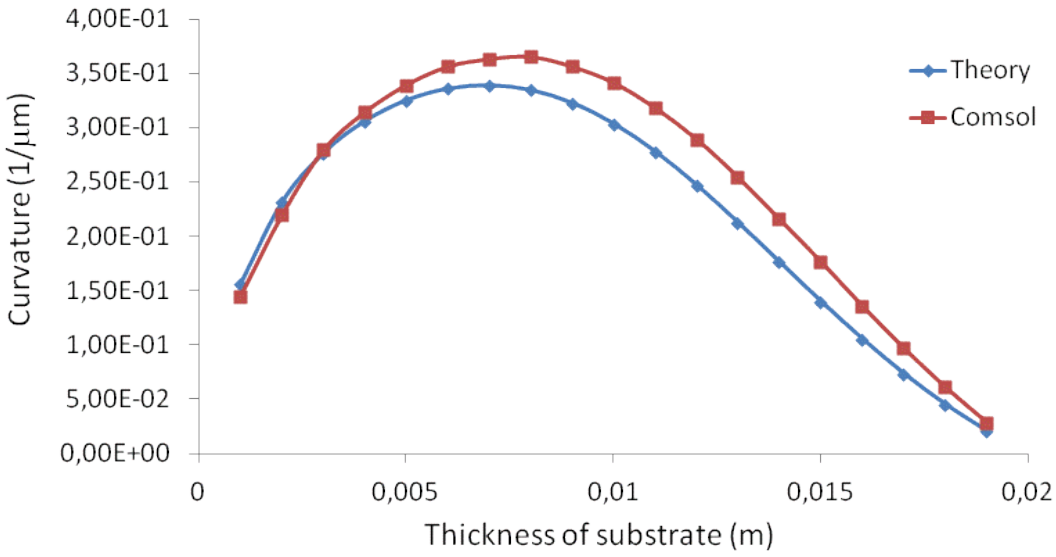

FIG 4.7 THEORETICAL AND NUMERICAL DATA COMPARISON.

The trends reported in Figure 4.7 show a very good agreement between the theoretical and numerical study. Both trends identify that, when keeping constant the elastic modulus of the materials and the total bilayer thickness, the resulting curvature is a function of the ratio between the thickness of the two layers. The maximum curvature is associated with a specific thickness ratio (substrate: top layer = 8:2) of the two layers and corresponds to the deformation mode in Figure 4.8.

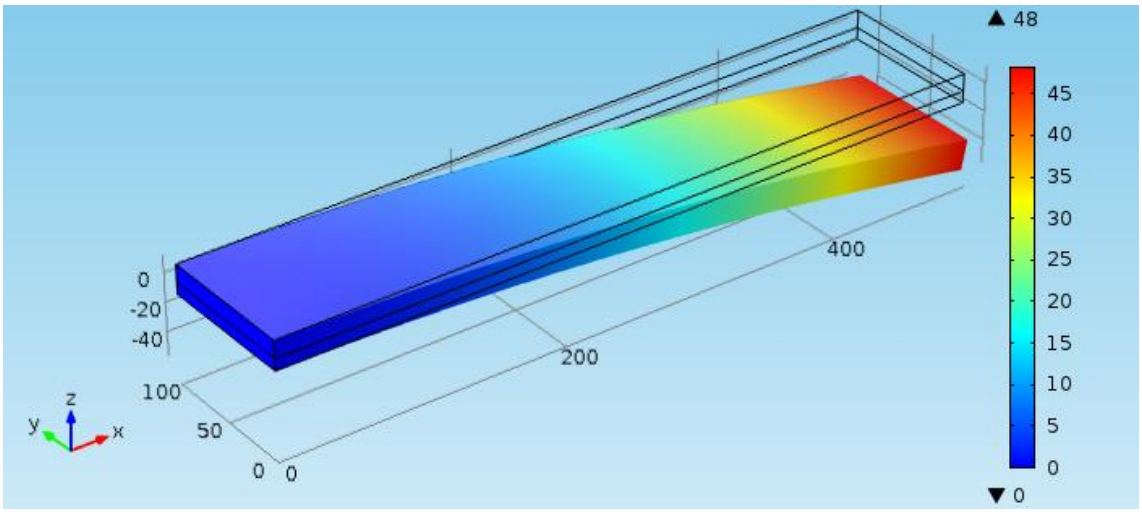

FIG. 4.8 COMSOL SIMULATION RESULT WHICH SHOWS THE MAX DEGREE OF DEFORMATION.

The analysis of the theoretical equations (3) to (6) show that the coefficients of thermal expansion appear only in the numerator of the equations and in equation (4) the resulting curvature is somehow related to the difference of the substrate and the coefficients of the other layers. Therefore, the ***resulting curvature increases with increasing difference of the coefficient of thermal expansion*** of the two layers. However, these equations also show a dependence of the resulting curvature to the thickness of the layers and to the Young's modulus. In order to understand this dependence, the same analysis was repeated by varying the modulus of the substrate, thus by varying the ratio between the substrate modulus and the other layer. The corresponding results are reported in Figure 4.9 in terms of curvature vs substrate thickness for three different substrate modulus values (2.4 GPa, 8.6GPa and 30GPa). It is clear that the effect of the modulus ratio variation results in a *shift only* of the curves and not in a variation of the maximum reachable final curvature. In other words, the results reported in this section highlight very clearly that the *maximum reachable deformation* or curvature, *is mostly influenced by the variation of the coefficient of thermal expansion* of the two layers while the ratio of the elastic modulus of the two

layers has an effect only on the two layer's thickness ratio for which the above maximum deformation can be reached. This is a very important result since it highlights very clearly the key parameters that need to be adjusted in a multilayer system to maximize the resulting deformation.

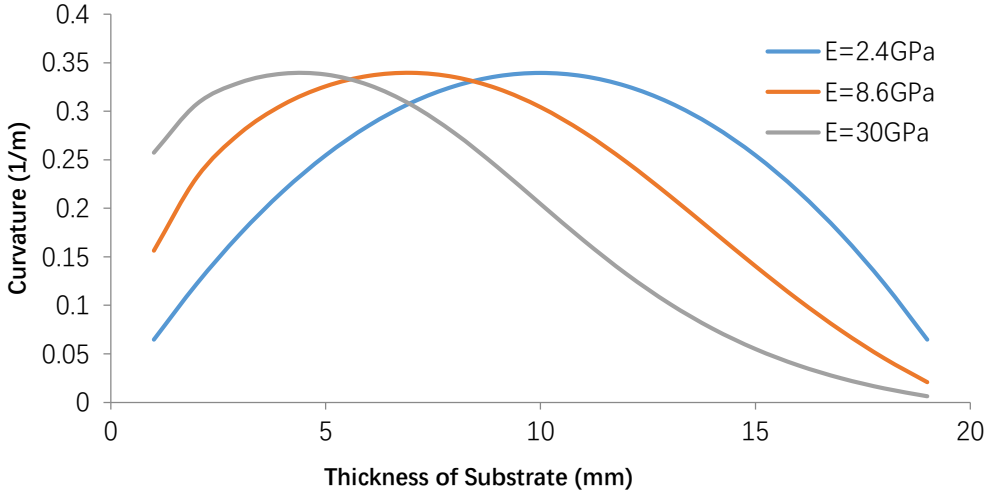

FIG. 4.9: RESULTING CURVATURE BY VARYING THE SUBSTRATE MODULUS.

Finally, in Figure 4.10 it is shown the comparison of the maximum percentage of deformation, which can be easily calculated through numerical simulations, and the theoretical prediction of the curvature variation. It is clear that the two methods give very similar results and are both reliable to assess the problem. In conclusion a maximized response of 9.6% percentage of deformation is achieved for a substrate thickness of 8mm.

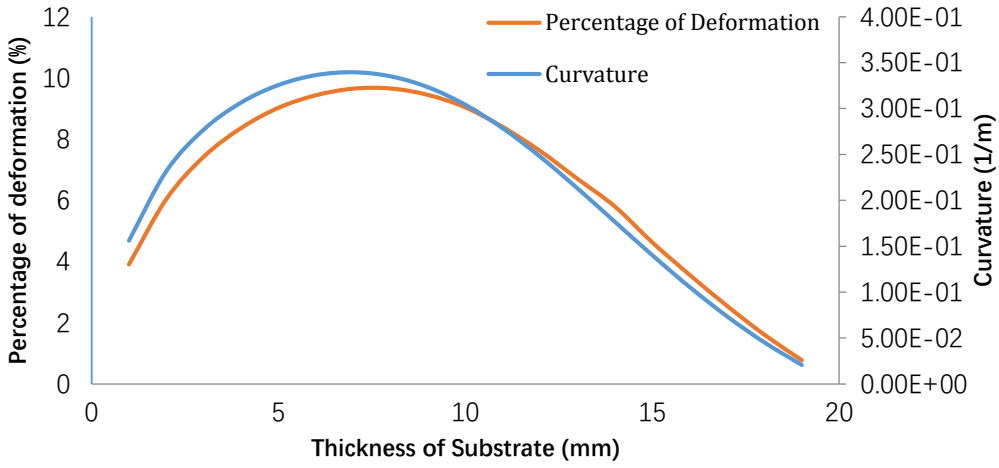

FIG. 4.10. TREND CURVES OF PERCENTAGE OF DEFORMATION AND CURVATURE FOR 2-LAYER COMPOSITE COMSOL MODEL.

4.4. Increasing the Number of Layers: Three-layers Case Study

In section 4.3 it was demonstrated a direct relation of the material response to the coefficient of thermal expansion of the involved layers. For this reason, an additional layer, characterized by a much higher thermal expansion coefficient than the other layers, was added to increase the overall percentage of deformation of the multilayer system. The mechanical and thermal properties of each material can be found in table 4.2. Since the results in the previous section highlighted very clearly that the theoretical and numerical approaches lead to very similar results, then more complex cases were directly treated with a numerical approach using Comsol Multiphysics. The three-layer material was simulated under the same conditions as the two-layers case-study reported in section 4.3. In this case, however, the trend of percentage of deformation and curvature were obtained by changing the thickness of the top layer while the thicknesses of other layers were fixed (Fig. 4.11). It is observed that, as expected, the max percentage of deformation increases in the three-layer case reaching a maximum value of 11% for a top layer thickness of 7mm.

TABLE 4.2: MECHANICAL AND THERMAL PROPERTIES OF THREE-LAYER COMPOSITE COMPOUNDS.

Quantities	Symbols	Dimensions	Polycarbonate	Reinforced Polycarbonate	Polyethylene
Heat capacity	C	J/(kg*K)	1200	1080	1900
Young's modulus	E	Pa	$2.4e^{9}$	$7.9e^{9}$	$0.931e^{9}$
Thermal expansion coeff.	A	1/K	$70e^{-6}$	$23e^{-6}$	$120e^{-6}$
Poisson ratio	ν		0.37	0.37	0.46
Thermal conductivity	K	W/(m*K)	0.22	0.26	0.5
Density	Rho	kg/m^3	1.22	1.42	0.94

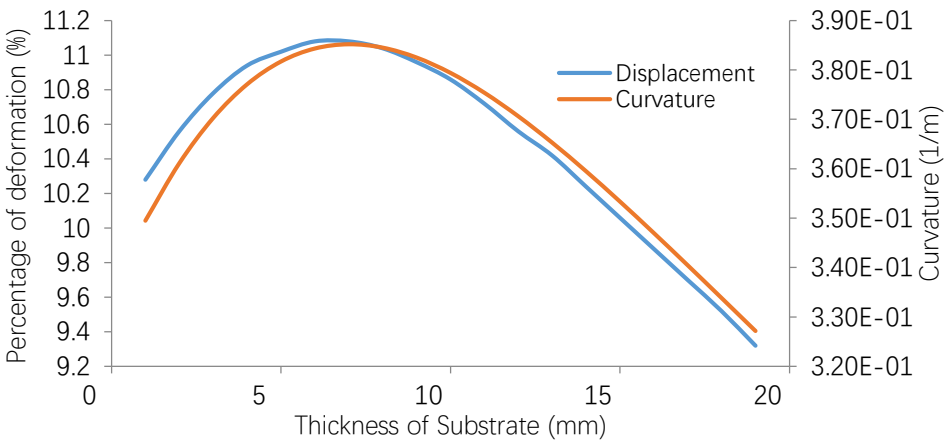

FIG. 4.11. PERCENTAGE OF DEFORMATION AND CURVATURE FOR THREE-LAYER CASE STUDY (COMSOL MULTYPHYSICS).

4.5. Optimization of a Multilayer Material Design Towards Morphing

The results of the previous sections showed first the dependence of the material response on the coefficient of thermal expansion gradients and then that a proper increase in number of layers can lead to a response improvement. More specifically for the above reported case studies, the overall maximum reachable percentage of deformation was improved from 9.6% to 11% by going from a bilayer system to a three-layer system. However, some considerations should be taken into account. A percentage of deformation increase of 1.4% is rather low if compared with the increase in production and design complexity. Adding one layer to the design in fact means additional fabrication steps, additional criticalities like for instance the adhesion between layers which should be guaranteed during the material in-service life. For this reason, it is believed that it is important to find alternative strategies to improve the overall performance of a bilayer material instead than trying to maximize performance increasing the number of layers.

With this in mind, going back to the concept that the variation in coefficient of thermal expansion between layers is essential, a bilayer material that comprises a substrate layer that is characterized by a negative coefficient of thermal expansion while the other layer, to start, was kept constant as in the previous cases. In order to understand the limit of such an approach, the material with the lowest

known negative coefficient of thermal expansion, which is a ceramic, was chosen for this case study without considering other important aspects like materials compatibility. The mechanical and thermal properties of both materials are show in table 4.3. The simulations were held under the same dimensions and condition as previous simulations. A similar trend of curvature previously discussed characterizes this materials design. In Figure 4.12 the trend of the maximum percentage of deformation is reported as a function of the substrate thickness variation. In this case the maximum percentage of deformation is 32.8% for a substrate thickness of 5mm. A further improvement was reached by making a bilayer material whose substrate thickness was the maximized value above reported (5mm) while the modulus of the substrate (which is the modulus of the layer with the negative coefficient of thermal expansion) was varied. The corresponding results are reported in Figure 26 which show that a modulus increase lead initially to a deformation percentage increase until a plateau is reached at 35% for a young's modulus of 15 GPa. In other words, by using a layer with a negative coefficient of thermal expansion, the percentage of deformation in a bilayer system can be enhanced from 9.6% to 35%, which is significantly higher improvement than increasing the number of layers.

However, the critical issue is that, the response was maximized using a ceramic layer overlapped to a polymeric layer. This is clearly not an ideal solution because of materials mechanical and physical compatibility in addition to obvious additional complexities in the fabrication process. Unfortunately, as better discussed in the following section, most existing materials with a negative thermal expansion coefficient are ceramics and alloys. Alternative solutions were then proposed as later discussed.

TABLE 4.3: MECHANICAL AND THERMAL PROPERTIES OF POSITIVE AND NEGATIVE LAYER COMPOSITE COMPOUNDS.

Quantities	**Symbols**	**Dimensions**	**Polycarbonate**	**$Bi_{0.95}La_{0.05}NiO_3$**
Young's modulus	E	Pa	2.4e9	$6e^{9}$
Thermal expansion coeff.	A	1/K	$70e^{-6}$	$-80e^{-6}$

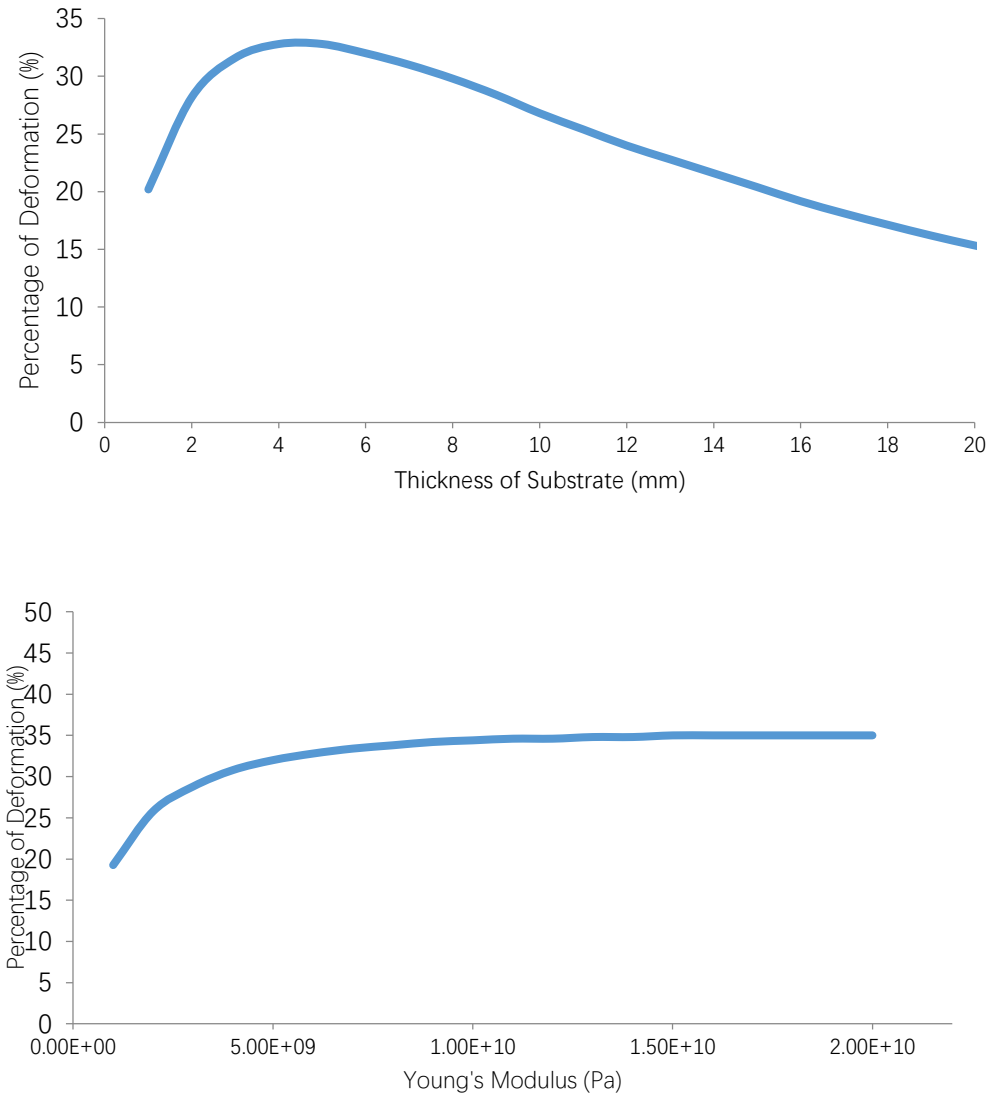

FIG. 4.12. PERCENTAGE OF DEFORMATION AS A FUNCTION OF THE SUBSTRATE MODULUS INCREASE.

4.6. References

1. Chunxue Gao, Zhiwei Zhao, Modeling of thermal stresses in elastic multilayer coating systems, Journal of Applied Physics 117, 055305 (2015)

2. Christine M. Andres, Jian Zhu, Shape-Morphing Nanocomposite Origami, Langmuir 2014, 30, 5378-5385

3. N. Athanasopoulos, N. J. Siakavellas, Programmable thermal emissivity structures based on bioinspired self-shape materials, Scientific RepoRts 5:17682

4. E. Eckstein, E. Lamacchia, thermally-driven snap-through and multistability using laminated fibre-metal shells, ECCM-16TH EUROPEAN CONFERENCE ON COMPOSITE MATERIALS, Seville, Spain, 22-26 June 2014

5. Zhang.X, Cary L. Pint, Optically- and Thermally-Responsive Programmable Materials Based on Carbon Nanotube-Hydrogel Polymer Composites, Nano Lett. 2011, 11, 3239–3244.

6. C.H. Hsueh. Thermal stresses in elastic multilayer systems. Thin Solid Films; Volume 418, Issue 2, 182–188

Chapter 5

Cellular Materials with Tuneable Coefficient of Thermal Expansion: Reaching the Negative Limit

The preliminary study reported in Chapter 4 showed very clearly that the morphing capability of a material formed by an aggregation of multiple layers with different thermal and mechanical properties, can be amplified by enhancing a key factor which is the coefficient of thermal expansion mismatch between layers. It was also shown that this mismatch should be tuned with the thickness and elastic modulus ratio among the layers. In a bilayer system, which is the simplest from a fabrication stand-point, a significant improvement of the percentage of deformation was reached when one of the layers was characterized by a negative coefficient of thermal expansion. However, most known materials that are capable to provide such a property are of a ceramic nature, as described in the following section 5.1, while the focus of this thesis relates to the development of polymeric-based morphing materials that can provide enhanced morphing capability, mechanical flexibility and reduced weight. A ceramic layer would certainly limit not only the overall material performance in terms of maximum deformation capability, mechanical flexibility and system

reliability, but would also require more complex fabrication processes to be implemented and, finally, would add weight. In this chapter the design of a novel film characterized by a miniaturized cellular structure that can be tuned to reach different thermal properties is presented. This polymeric film is capable to provide the largest ever presented negative coefficient of thermal expansion.

5.1. Negative Coefficient of Thermal Expansion: State-of-the-Art

Thermal expansion is the term that describes the volume increase of a material upon heating under constant pressure, which can be found in almost natural polymer materials. There are special and rare groups of materials which have negative thermal expansion coefficient (NTE). These materials contract, instead than expand, upon heating. The interesting on this kind material has increased so much that it is becoming rapidly a growing area of research over the past two decades. There are some main groups of materials that are characterized by a negative coefficient NTE, such as ceramics, alloys and composites. Some of them are described below.

Flexible network

This category includes diverse materials, such as silicates like $LiAlSiO_4$, tungstates like ZrW_2O_4 and cyanides like $Cd(CN)_2$. This type of NTE materials contain strong atomic bonds like W-O and Si-O. The NTE appears once the dynamical deformation open the spaces in the crystal lattice under thermal gradients (Figure. 5.1) [1]. The range of NTE in this category is from -1 to -33.5 ppm/K, for example ZrW_2O_4 has NTE as -6 ppm/K and $Cd(CN)_2$ has NTE as -33.5 ppm/K.

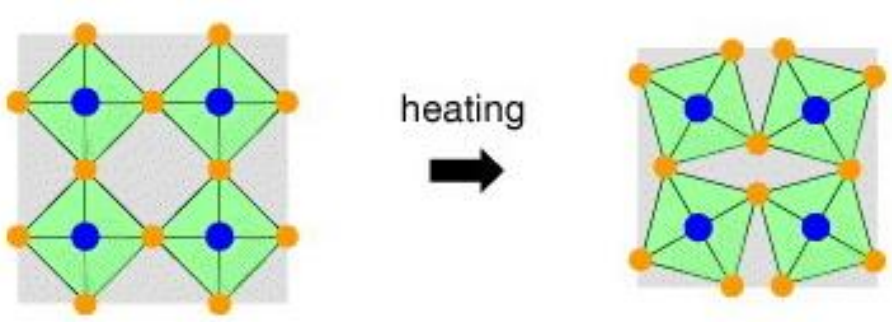

FIG. 5.1 SCHEMATIC OF NEGATIVE THERMAL EXPANSION IN A FLEXIBLE NETWORK. A VIBRATIONAL MODE CONSUMING A SPACE IN A LATTICE IS THERMALLY EXCITED, WHICH YIELDS THERMAL CONTRACTION.

Silicates

Silicates of various kinds like $LiAlSiO_4$, $Li_2Al_2Si_nO_{4+2n}$ and $Mg_2Al_4Si_5O_{18}$ are the most important group among NTE materials. These materials contain covalent bonds that do not expand. The mechanism of the NTE effect is due to the mismatch of two types of bonds, ionic bonds such as Li-O and Mg-o and covalent bonds such as Al-O and Si-O [2]. When temperature increases, the ionic bonds are lengthened and the covalent bonds keep being rigid, so that the material are forcibly pulled closer together as shown in Fig. 5.2.

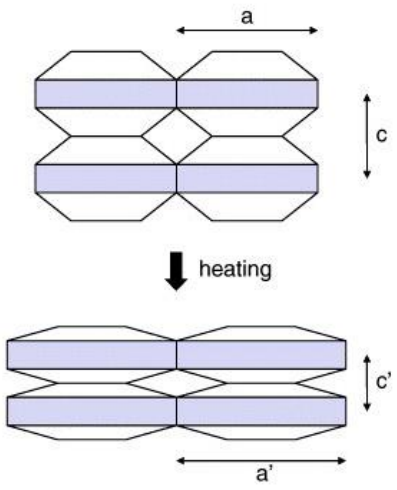

FIG. 5.2. SCHEMATIC OF ANISOTROPIC THERMAL EXPANSION IN THE SILICATES. AS THE SHADED LAYERS UNDERGO THERMAL EXPANSION, THEY ARE PULLED CLOSER TOGETHER IN THE DIRECTION PERPENDICULAR TO THE LAYERS, WHICH CAUSES SIGNIFICANT THERMAL CONTRACTION IN THIS DIRECTION.

Consequently, significant NTE is non uniform and appears in one direction only which is perpendicular to the sheet that expands thermally. Although volume thermal expansion can be either positive or negative in this mechanism, many materials show net negative (although not large) volume thermal expansion. The typical value of NTE is around -2 ppm/K in this group of materials.

Zirconium tungstate

The ZrW2O8 consists of ZrO6 octahedra and WO4 tetrahedra, which are connected via the corner O atoms. As an important exception, one O atom on each WO4 tetrahedron is not connected to another unit and is therefore regarded as unconstrained, the NTE was reported by Martinek and Hummel in 1986 [3]. This O atom is located on a WO4 vertex oriented along one of the [111]

directions that is shown in Fig.5.3 [4]. The ZrV2O7, which has a similar structure of ZrW2O8, is a member of the ZrW2O8 family, this family contain also HfW2O8, ZrMo2O8 and etc. Due to the strong covalent bonds, ZrO6 octahedra and the WO4 tetrahedra themselves show negligible thermal expansion. The primary origin of NTE in ZrW2O8 has long been attributed to the large-amplitude low-energy transverse vibration of the O atom in the middle of the W–O–Zr linkage [5]. A transverse vibration of a bridging O in a framework in which metal (M)–O bond distances remain largely unchanged, will cause contraction of the M–M distance and a negative coefficient of thermal expansion (Fig. 5.3) is exploited. The range NTE is between -6 to -9 ppm/K.

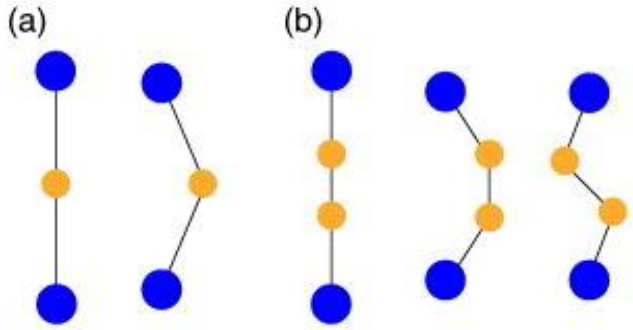

FIG. 5.3 SCHEMATIC OF LOCAL VIBRATIONAL MODES RESPONSIBLE FOR NEGATIVE THERMAL EXPANSION: (A) SINGLE-ATOM AND (B) DIATOMIC LINKAGES. THE LARGER (BLUE) CIRCLES REPRESENT HEAVY (USUALLY METAL) ATOMS, WHEREAS THE SMALLER (ORANGE) CIRCLES REPRESENT LIGHT ATOMS SUCH AS CARBON, NITROGEN, OR OXYGEN.

Cyanides

For NTE in a flexible network, it is important that steric contraction outweighs the conventional thermal expansion of chemical bonds. To this end, strong covalent bonds are not indispensable. This point is exemplified by a series of cyanide-bridged compounds [6-9]. This class of materials exhibits the largest NTE in this category, i.e. $\alpha = -33.5$ ppm K^{-1}.

Invar Alloy

Invar means the first discovered Fe–Ni alloys in a narrow sense, but now it is used as a general term for magnetic metals and alloys that exhibit thermal-expansion anomalies of magnetic origin. The magnetovolume effect itself is often called the Invar effect. For over a hundred years, Fe–36Ni (0.1-1 ppm/K) has been an important general-purpose, low-expansion material. Aside from the Fe–

Ni alloys, this group of materials includes materials of many kinds such as Fe–Pt Invar (-6 to -30 ppm/K) and super Invar (Fe–Ni–Co) [10].

Composites

Since all of the NTE material above discussed contain transition metals, so their cost is expensive if compare with polymeric materials. In order to reduce costs, composite materials which contain a polymer matrix and NTE particles as filler were developed, fabricated and tested. The issue is that almost all known polymers are positive CTE materials, just a few of them have NTE like Kevlar with -2 ppm/K. So the composite material contains positive CTE polymer and NTE filler will not have a better NTE response than the above listed materials. Yamanoto and Eleftherios [11] made a new cellular structure which have ultra-low thermal expansion, as shown in Fig. 5.4. The idea is to have a frame that is built by low CTE materials, and a high CTE material is placed inside the frame and reserved space for the high CTE material expansion. In other words, this design can only avoid the material expansion thanks to the reserved space, but is not able to reach a negative CTE.

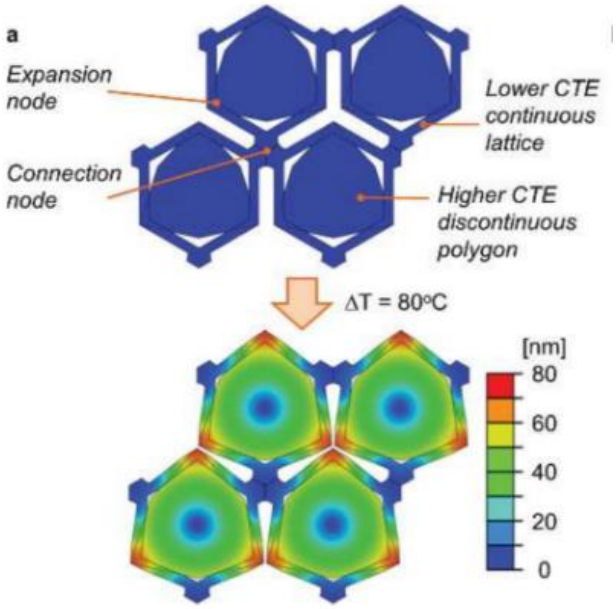

FIG. 5.4. STRUCTURE OF THE MATERIAL DESIGN FROM YAMANOTO AND ELEFTHERIOS [11].

5.2. Novel Polymer Film with a Negative and Tuneable Coefficient of Thermal Expansion

5.2.1. Objective and Approach

The objective is to design a novel polymeric material in the form of a film that can provide a tuneable and indeed negative coefficient of thermal expansion to be used, within this thesis, for temperature driven outperforming morphing materials. It is worth noting that, despite the scope of this thesis, the proposed material can be used for several other applications which require the use of light-weight materials whose thermal properties can be tuned according to the specific application.

The **overall requirements** that the polymeric material shall satisfy can be summarized as follows:

- Light-weight and flexible
- Isotropic response to temperature gradients
- Tuneable coefficient of thermal expansion
- Maximized negative coefficient of thermal expansion using only materials with a positive coefficient of thermal expansion

The above listed desirable material properties represent major challenges and are here addressed respectively with the following **key material design choices**:

- Remove unnecessary material to reduce weight: this leads to the strategic choice of designing a film with a miniaturized cellular structure
- Mechanical flexibility is achieved by using flexible polymers that form the cells
- Isotropy in the material response is achieved by properly designing and aggregating the forming cells, so by properly designing the material structure at the microscale
- An intelligent design of the material at the microscale can allow slight changes to reach variable coefficients of thermal expansion at a low effort (as here demonstrated)
- An intelligent design of the film at the microscale can allow to achieve and amplify, if necessary, negative coefficients of expansion of the resulting discrete film by creating its

miniaturized structure with polymers that are characterized by a positive coefficient of thermal expansion.

The latter strategic material design choice is obviously related to the criteria of making a film characterized by a discrete structure at the microscale instead than a continuous film whose structure and properties are related only to the specific aggregation of the polymer chains. A discrete film requires the design of the forming cells, and these can be achieved by assembling miniaturized polymeric elements that expand once exposed to temperature gradients. The expansion of these elements causes the formation of internal forces and stresses that result in an overall cell deformation whose degree and versus can be controlled by controlling the position/interaction of the mentioned elements.

5.2.2. Taking Inspiration from Micro-Thermal Actuators: A Preliminary Study

It is well known that any material has a specific degree of expansion/restriction when exposed to temperature gradients and this response is dictated by the positive/negative coefficient of thermal expansion of that material. However, typically the capability of expanding/contracting is rather limited by the material molecular structure and, as demonstrated in chapter 4., this deformation capability is not sufficient to induce a significant percentage of deformation in a multilayer system, as required for morphing applications. We believe that a way out to this issue is the exploitation of thermal amplification mechanisms into our material microstructure design. For instance, thermal actuators represented for us a great source of inspiration. Surface-micro machined thermal actuators typically utilize constrained thermal expansion to achieve amplified motion. The bent-beam or “V” shaped actuator [12-16] is one of the most common, it amplifies the small input displacement created by thermal expansion of the V shaped beams, also commonly called legs, arranged in parallel as shown in Figure 5.5. Because of the shallow angle of the beams, the centre shuttle experiences an amplified displacement in the direction of the offset.

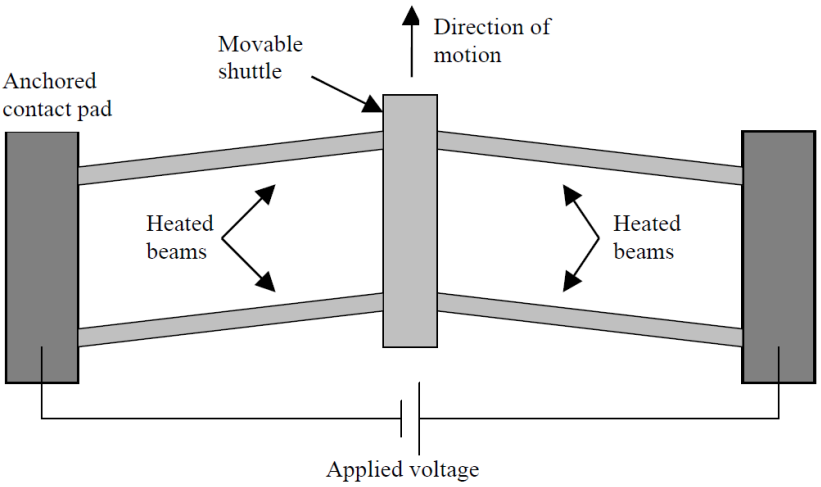

FIG. 5.5. V-SHAPED THERMOMECHANICAL MICROACTUATOR. COURTESY BY REF. [12]

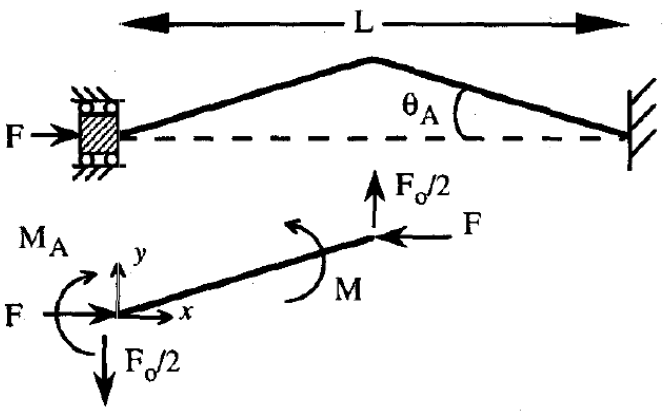

FIG. 5.6. THERMAL ACTUATOR MODEL AND CONSTRAINS. COURTESY BY REF. [13]

It is possible to predict the amplified displacement of the beams, by modelling the actuator through a beam theory in which the beams are constrained as in Figure 5.6[13]. One of the two ends of the beam is fixed and the other is guided along the x direction. The equation that governs the left portion of the beam is:

$$EI \ \frac{\partial^2 y}{\partial x^2} = M = M_A - Fy - F_o x/2 \quad (1)$$

being *E* the Young's modulus of the beam, *I* the moment of inertia, *EI* the flexural rigidity, F is the reaction force along the x-axis that is necessary to model the thermal stress, *Fo* the output force.

The boundary conditions are:

$$y|_{x=0} = 0 \qquad (2)$$

$$\left.\frac{\partial y}{\partial x}\right|_{x=0} = \left.\frac{\partial y}{\partial x}\right|_{x=L/2} = tan\theta_A \qquad (3)$$

$$\sigma = \Delta T E \alpha = \frac{E}{L}\left(\Delta L + \frac{FL}{EWT}\right) \qquad (4)$$

in which ΔT is the temperature change, L, W and T are the actuator length, width and thickness, respectively, ΔL is the change L due to F and α is the thermal expansion coefficient of the material.

Comsol Multiphysics models in a thermomechanical environment were found to be reliable when the resulting data were compared with the theoretical predictions. Figure 30 shows the case of a Nylon beam, whose coefficient of thermal expansion is 28ppm/K, formed by two arms (100 μm in length) that are tilted with an angle θ of 45° and that are fully constrained at the base in the red points shown in Figure 5.7. In other words, the *x*, *y* displacements and the rotations are blocked.

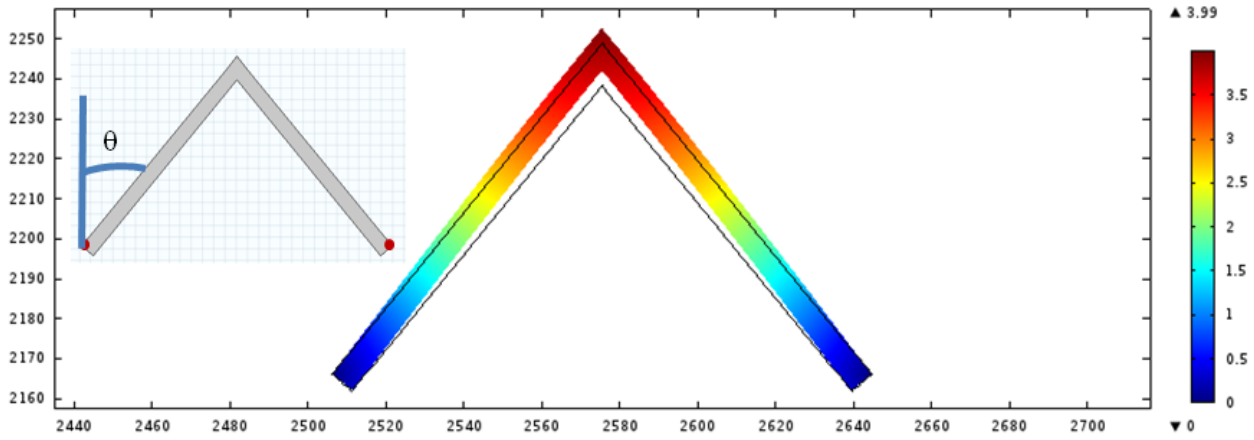

FIG. 5.7. EXAMPLE OF THE NUMERICAL RESULTS FOR A NYLON-BASED AMLIFICATION MECHANISM.

Once the tilted beams are exposed to a temperature gradient from 30°C to 120°C, they expand along the beam axes and, being the beams blocked in the horizontal displacement, they experience a deflection which moves the upper corner upward (along the vertical direction). The scale bar in the figure represents the surface total displacement (in μm) and highlights that the highest displacement in the beam is reached at the aforementioned upper corner. The maximum displacement along *y* is a

function of the beam length and of the tilting angle θ. In order to quantify the benefit of displacing the beams in such a configuration, and, most importantly, to verify under which conditions the mechanism can truly amplify the overall beam displacement, the mechanism was compared with a continuous beam displaced vertically, made of the same material as the mechanism (Nylon) and characterized by a length that is the same as the total length of the two beam elements forming the mechanism. In other words, the straight beam had a total length of 200 μm and was fully constrained at the base as in Figure 31. The mechanism in this case was modelled with a variable tilting angle θ, more specifically, with θ varying from 0° to 90° while the overall 200 μm length was kept constant where they were overlapped when the tilting angle is 0°.

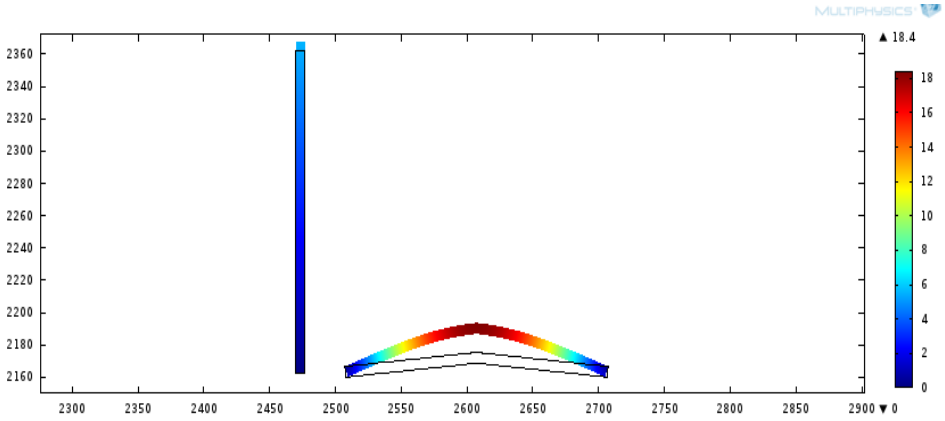

FIG. 5.8. COMPARISON OF THE MAXIMUM DISPLACEMENT FOR THE MECHANISM AND THE CONTINUOUS BEAM, IN THIS GRAPH THE 80° ANGLE CASE IS PLOTTED.

The scale bar in Figure 5.8 clearly highlights that the mechanism experiences a significantly higher total upward displacement than the axial displacement (along the vertical direction) of the straight beam. This is already proofing the efficacy of the mechanism since the effect of splitting and tilting the beams truly results into an overall amplification of the vertical displacement. However, this study also shows that this effect can be truly exploited after a specific tilting angle of the beams. Figure 5.9, which reports the total displacement of the straight beam compared with that of the mechanism while its tilting angle is changing, shows that θ threshold value is 60°. In other words, for tilting angles lower than 60°, the straight beam is characterized by a higher degree of deformation due to thermal gradients than the mechanism. For angles above the mentioned

threshold values, the mechanism amplifies the overall displacement and the amplification capability increases with increasing angle until reaching a maximum for a tilting angle of 80°.

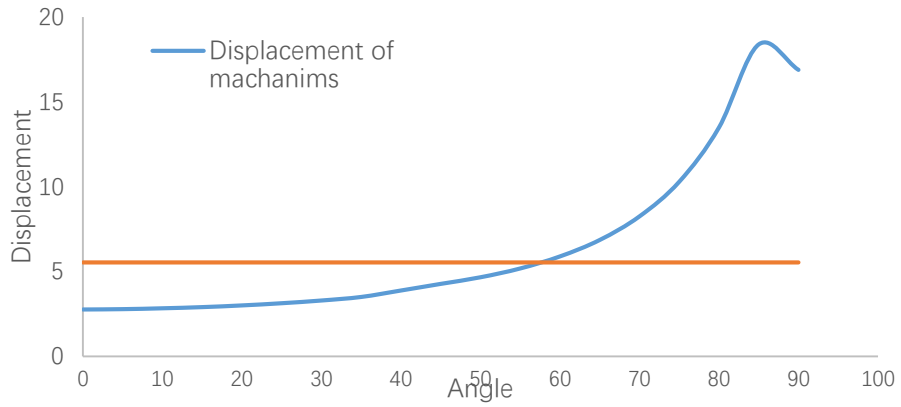

FIG. 5.9. COMPARISON OF MECHANISM AND STRAIGHT BEAM IN TERMS OF DISPLACEMENT VS. TILTING ANGLE VARIATION.

As mentioned in section 5.2.1. the overall approach is to realize a discrete material that presents an internal isotropy. This also implies, among several other things, that the elemental unit structure that forms the material overall structure at the microscale should somehow be repeated. By assuming that the mechanism represents our initial unit system, then two consecutive units were assembled and studied as depicted in Figure 5.10. It is worth noting that in this case the model in terms of temperature ranges, beam length, material, external constraints, was set as before. The two mechanisms are interconnected at the base and the *y* displacement of the interconnection points was let free while the *x* displacement was blocked. The analysis was again repeated for variable angles in the range from 40° to 80°. In this case the maximum displacement (16.04μm) corresponds to 75° angle (Fig. 5.11). The two mechanisms placed in series behave differently than the single mechanism. This is due to the presence of the internal constrain that allows for vertical displacements along *y* direction at the joint point of the two mechanisms. The axial expansion of the beams leads to the vertical displacement of the upper corner of the two mechanisms, as in the single mechanism case. But the axial expansion at the base of the two mechanisms, has a force component along the *x* and *y* direction. The component along *x* is cancelled out by the imposed internal constrain (*x* displacements are blocked), while the component along y, being not blocked, moves upward the interconnection point at the base of the two mechanisms. This effect is more evident in

the 60° than in the 75° case, as shown by comparing Figures 5.11 and Figure 5.12. The 60 degree (Fig. 5.12) has been chosen for further studies which have the potential to proof and activate the thermo mechanical micro actuator concept.

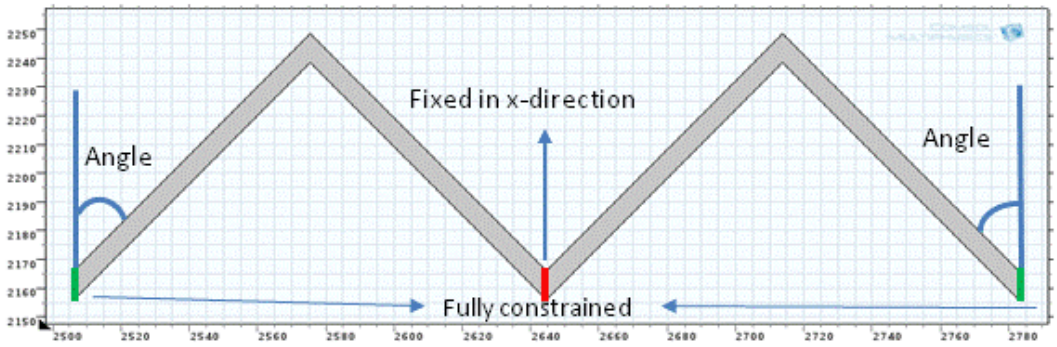

FIG. 5.10. SKETCH OF THE MODEL FOR TWO UNITS' MECHANISM, WITH X-DIRECTION CONSTRAIN (RED) AND FULLY CONSTRAINED (GREEN).

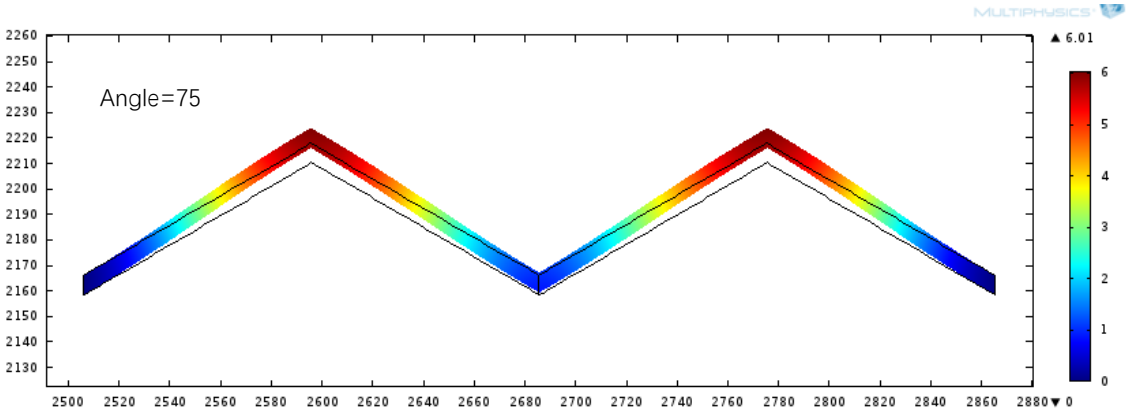

FIG. 5.11. MAXIMUM DISPLACEMENT RESULT WHEN THE ANGLE IS 75 DEGREES.

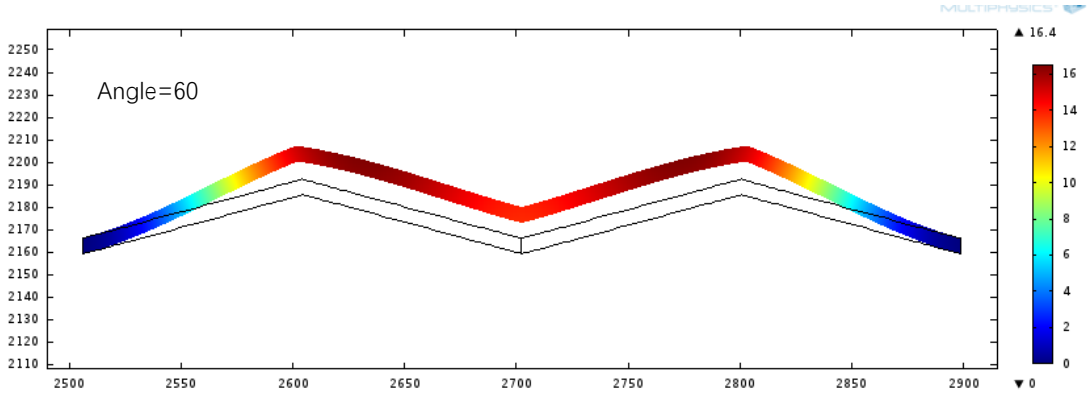

FIG. 5.12. MAXIMUM DISPLACEMENT RESULT WHEN THE ANGLE IS 60 DEGREES.

5.2.3. Design of a Single Cell: Initial Assessment

The preliminary results shown in section 5.2.2 highlighted the possibility of amplifying thermal effects of a material by using this material to build the special mechanism previously discussed in which two beams cross each other thanks to a specific tilting angle (see Figure 30). It was also shown that, a series of mechanisms (e.g. two mechanisms in series) keep the same effect at the top-most edge points of the system, but are also capable to provide a displacement of the base of the system were the mechanisms are interconnecting.

These results can be used to build-up a unit cell whose thermal properties should be amplified. Figure 5.13 shows as schematic of the initial design and the concept to form a unit cell.

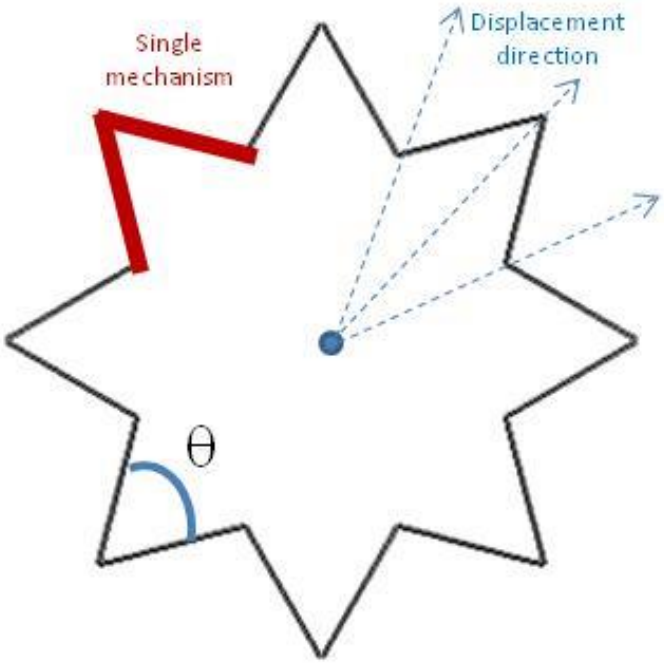

FIG. 5.13. SCHEMATIC OF A UNIT CELL.

The figure highlights in red a single mechanism that has a tilting angle θ which is then repeated to form a closed-loop up to a **star shape**. The structure is constrained at the centre of the cell in which all displacements are fully blocked. The top-edge and the base of each mechanism that forms the

star, are constrained in such a way that radial movements only are allowed. The number of mechanisms that fit in the star and the size of the star are a function of the tilting angle and of the beam length. The cell is exposed to a temperature gradient between 30°C and 120°C. The properties of the materials that were used to model the star cell are reported in Table 5.1.

TABLE 5.1: MECHANICAL AND THERMAL PROPERTIES OF THE MATERIAL USED IN STAR STRUCTURE.

Quantities	Symbols	Dimensions	Polycarbonate	Nylon
Heat capacity	C	J/(kg*K)	1080	1700
Young's modulus	E	Pa	$7.9e^{9}$	$2e^{9}$
Thermal expansion coeff.	A	1/K	$23e^{-6}$	$280e^{-6}$
Poisson ratio	ν		0.37	0.4
Thermal conductivity	K	W/(m*K)	0.26	0.26
Density	Rho	kg/m^3	1.42	1.15

Based on the previous results, an initial 60° tilting angle is chosen since it provides: a higher maximum displacement and an overall expansion also in the interconnecting points in the case of a series of multiple mechanisms. The star cell is then formed by combination of 8 mechanism units whose beam elements are made of polycarbonate (see properties in Table 6). The resulting cell diameter is of 21.1495 μm. Figure 5.14 shows the corresponding result in terms of maximum surface displacement once the star is exposed to the above mentioned temperature gradient. As desired, a uniform expansion is observed since all base and edge points of the series of mechanisms move along the radial direction.

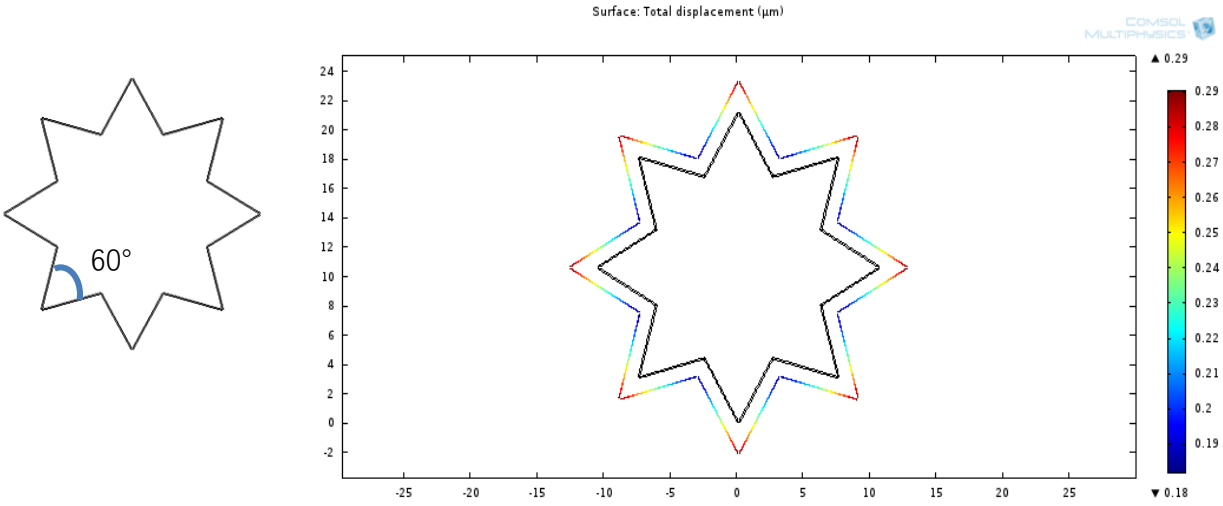

FIG. 5.14: STAR CELL SKETCH AND SIMULATION RESULT FOR THE 60 DEGEE ANGLE CASE.

The analysis is then repeated for different tilting angles (20 degree). Clearly in this case a significantly higher number of mechanisms builds-up the full cell and, since the length of each beam is kept constant, the overall cell diameter increases significantly reaching the value of 338.72 μm. Despite an increase in complexity of the latter cell design, the overall cell expansion is found to be exactly the same as in the previous case (1.37%) as shown in Figure 5.15.

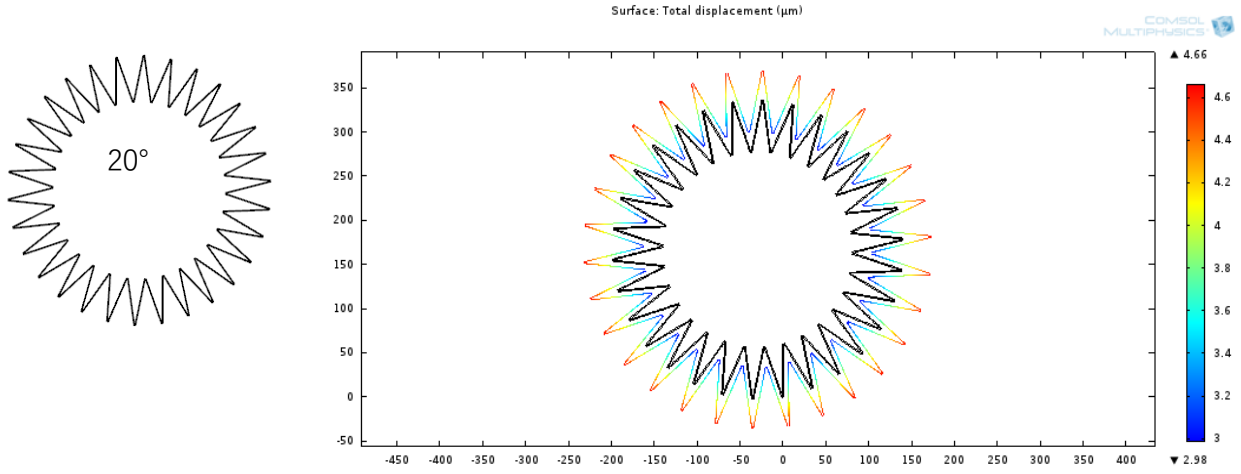

FIG. 5.15: THE STAR SKETCH AND SIMULATION WITH CONTAIN THE MECHANISM UNIT WITH 20-DEGREE ANGLE.

Further investigations are then performed to understand why no variation in response is recorded when the star design changes dramatically while going from a 60° to a 20° structure. To reduce computational costs, a quarter Nylon star (see table 6 for the adopted material properties) is

modelled taking advantage of the symmetry of the proposed design, and as depicted in Figure 5.16. This portion of the star is compared with a quarter of a circular area made of the same material (Nylon) and having the same radius as the star, but in this case the material forms a continuum layer that occupies the same area as a quarter of the star. This is done to verify the efficiency of the amplification mechanism. The adopted model and the corresponding results are shown in Figure 38 and highlights that the star design and the continuum layer deform in the same way when exposed to a temperature gradient. In other words, this result shows that the proposed amplification mechanism loses efficacy once it is incorporated into a more complex design as the star design.

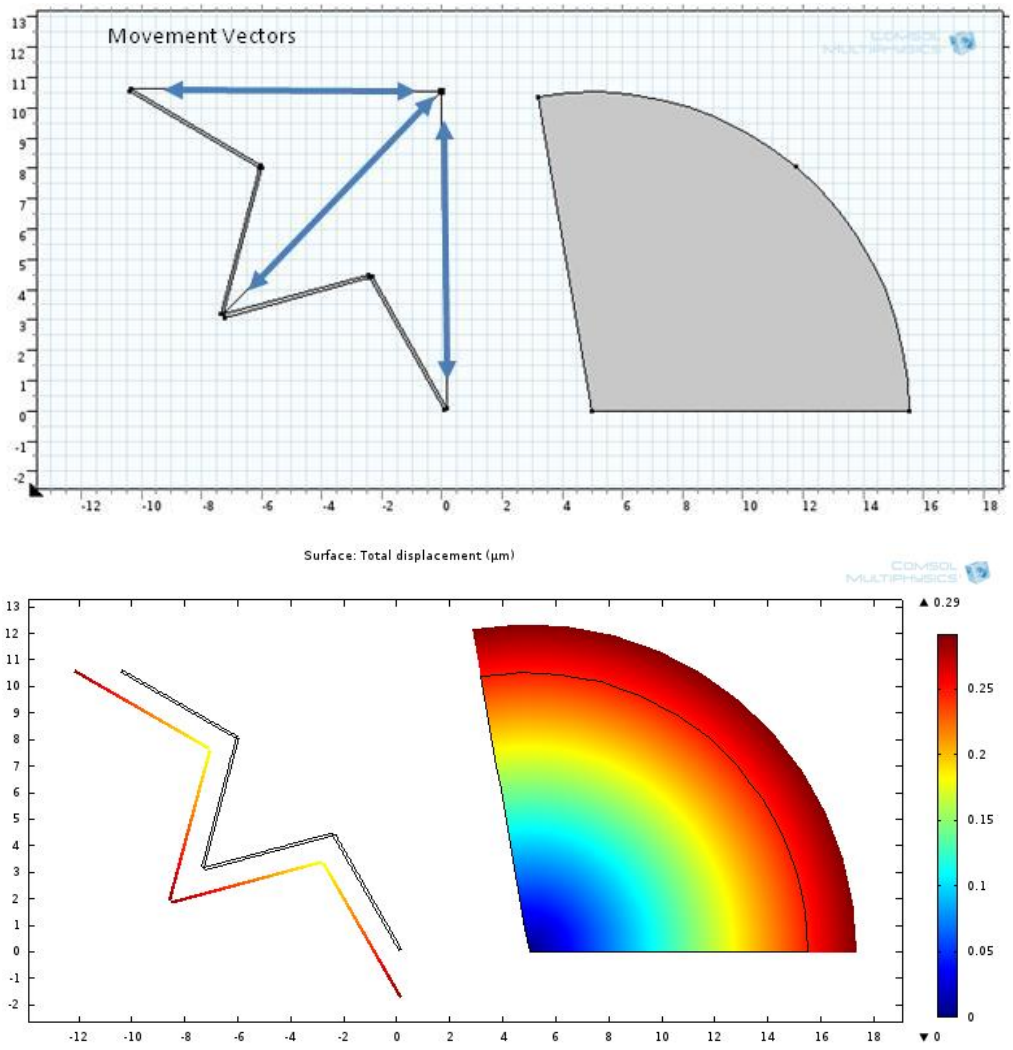

FIG. 5.16. COMPARISON OF THE STAR DESIGN WITH A CONTINUUM LAYER.

5.2.4. Tunable (positive/negative) Coefficient of Thermal Expansion: the Strategy

The preliminary work reported in section 5.2.3 was essential to understand deeply how to use amplification mechanisms into the design of discrete cells in order to exploit desired and specific thermal properties. The lack of amplification reported in section 5.2.3 when compared to a continuum layer of the same material, is solely related to missing internal constraints. ***Internal constraints*** are here integrated by ***adding to the star shape extra parts that can be differently shaped to optimize and tune, as desired, the thermal response of the resulting discrete material***. This extra element is made of a material that has a different coefficient of thermal expansion than the material that forms the main star structure. A strategic integration of these elements into the structure can lead either to a material whose overall response reflects a positive coefficient of thermal expansion, or to a material whose overall response shows a negative coefficient of thermal expansion. For instance, let's assume that the main star structure is made of Polycarbonate and the extra elements are made of Nylon that has a higher coefficient of thermal expansion than polycarbonate (both indeed have a positive coefficient). If the goal is to have a material with an enhanced, still positive, coefficient of thermal expansion, then the extra elements can link the two tilted beams of the unit mechanism as in Figure 5.17 (blue colour). Once the system is exposed to a temperature gradient, then the material with a larger coefficient (Nylon) expands more and pushes the interconnected beams, causing an opening of the angle, thus causing an overall expansion of the star. The numerical result of such a case is shown in Figure 30 and it is compared with the case of a full polycarbonate piece (right on Fig. 5.17) that clearly undergoes a smaller area increase due to the imposed increased temperature.

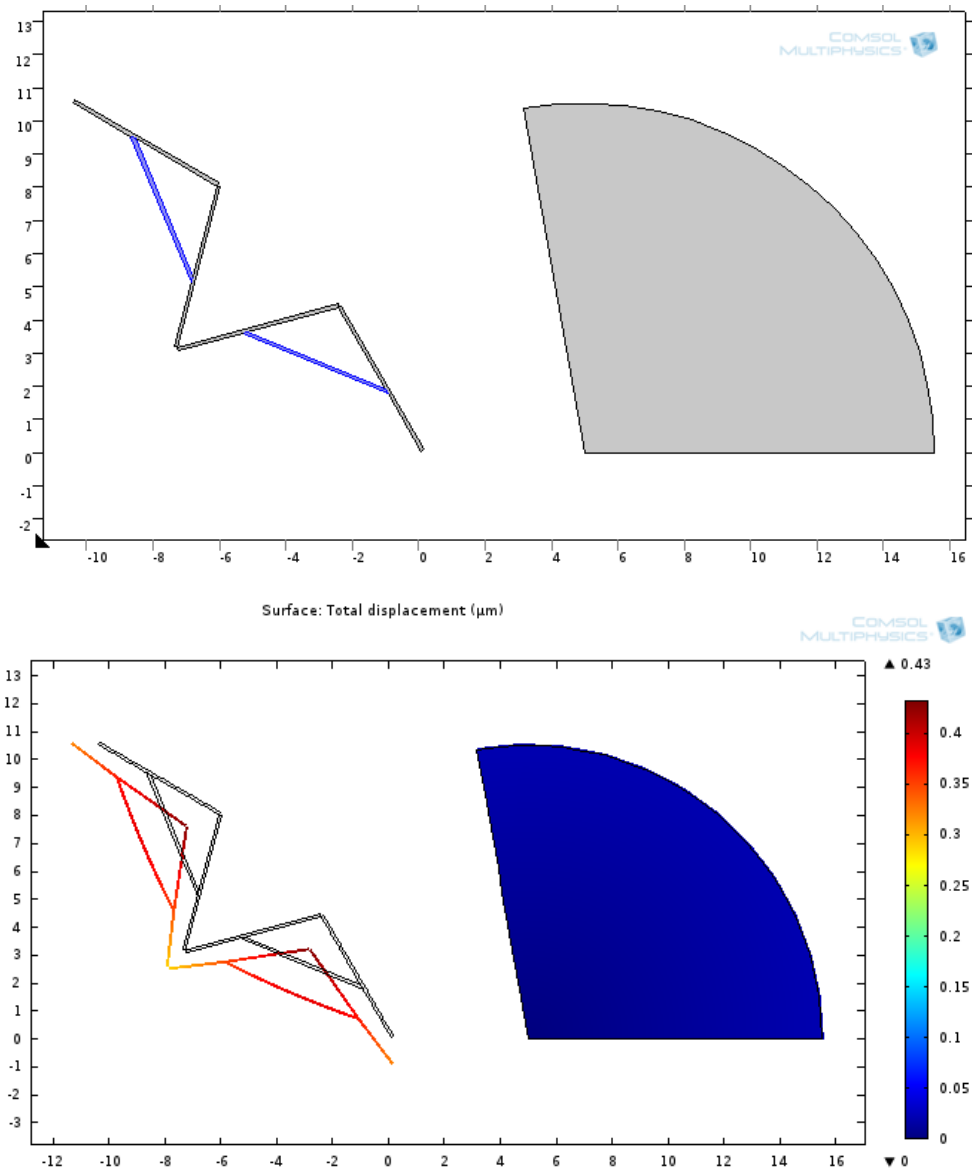

FIG. 5.17. SKETCH AND SIMULATION RESULT OF THE STAR DESIGN MODIFIED TO ACHIEVE LARGER EXPANSIONS UNDER TEMPERATURE. THE SCALE BAR SHOWS THE SURFACE DISPLACEMENT IN MICRO-METER.

On the other hand, if the Nylon elements are added to the polycarbonate star structure as in Figure 5.18 (blue elements), then, when temperature increases, the nylon elements expand as before, but this time, instead than opening the angle of the unit mechanism, they will tend to close it, thus to shrink the star. In other words, in this case ***the overall response is of a material that has a negative coefficient of thermal expansion even though it is fully composed of materials that are characterized by a positive coefficient***.

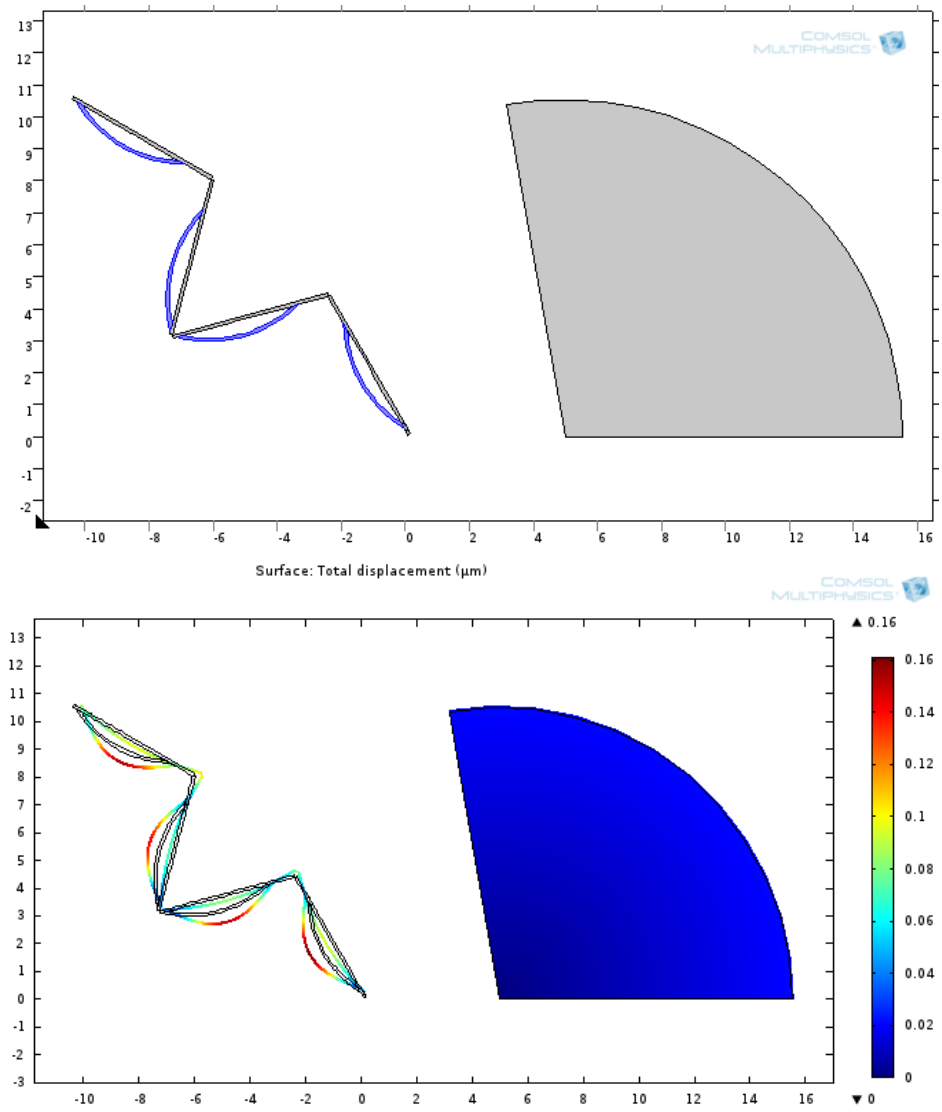

FIG. 5.18. SKETCH AND SIMULATION RESULT OF THE STAR DESIGN MODIFIED TO ACHIEVE SHRINKING UNDER TEMPERATURE INCREMENST. THE SCALE BAR SHOWS THE SURFACE DISPLACEMENT IN MICRO METER.

5.2.5. Cell Design Optimization for Ultra-Low (negative) Values

The star design can be modified to vary/tune the negative coefficient of thermal expansion using only materials characterized by a positive coefficient. Following the same concept described in the previous section, 8 different designs were studied as shown in Figure 5.19.

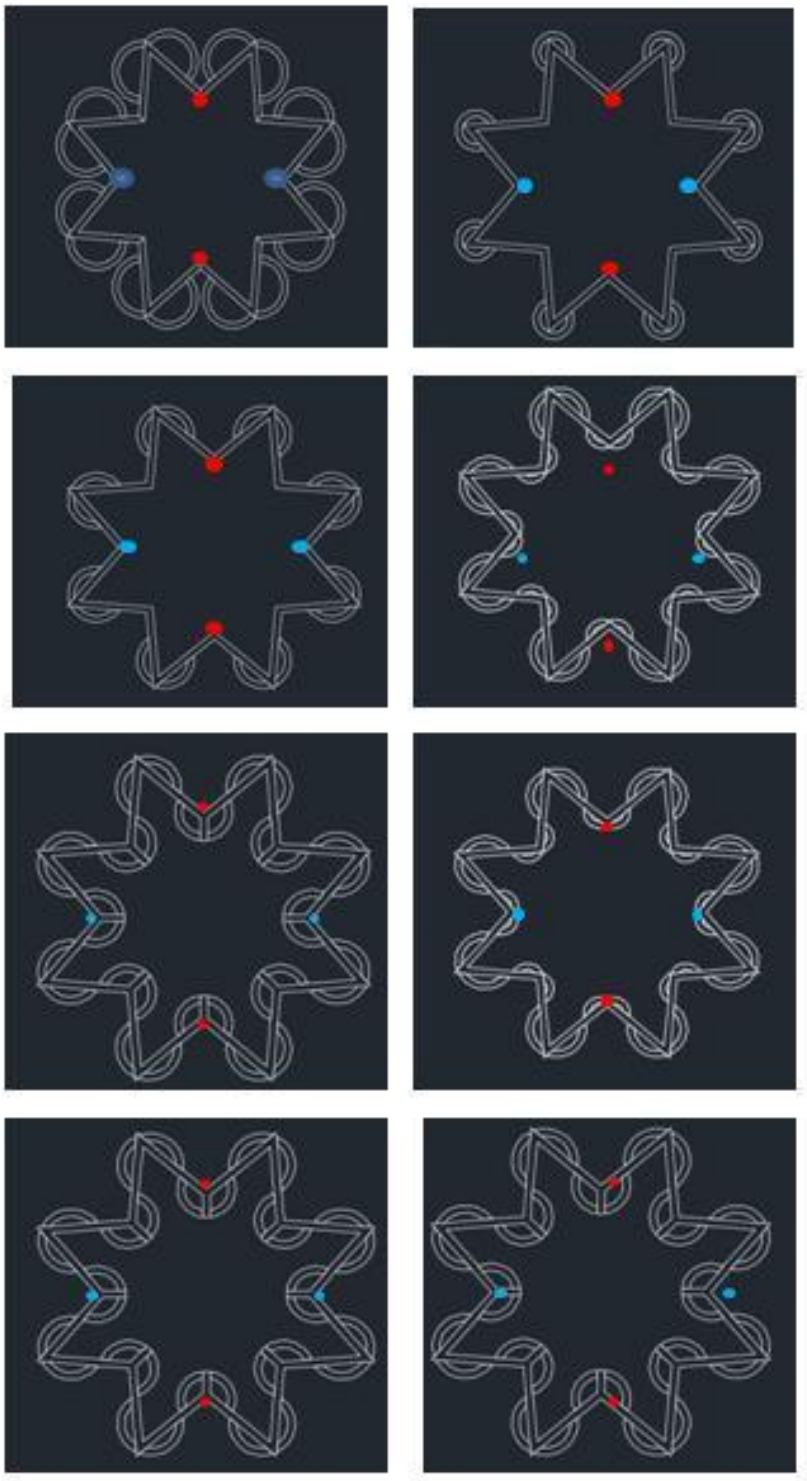

FIG. 5.19. PROPOSED DESIGNS TO INCREASE THE NEGATIVE COEFFICIENT OF EXPANSION.

These designs show an increasing maximum shrinking effect when temperature increases up to 120°C as shown in Fig. 5.20. This shrinking effect is quantified with the maximum displacement which sets at 25.6μm for the best model (Fig.43b).

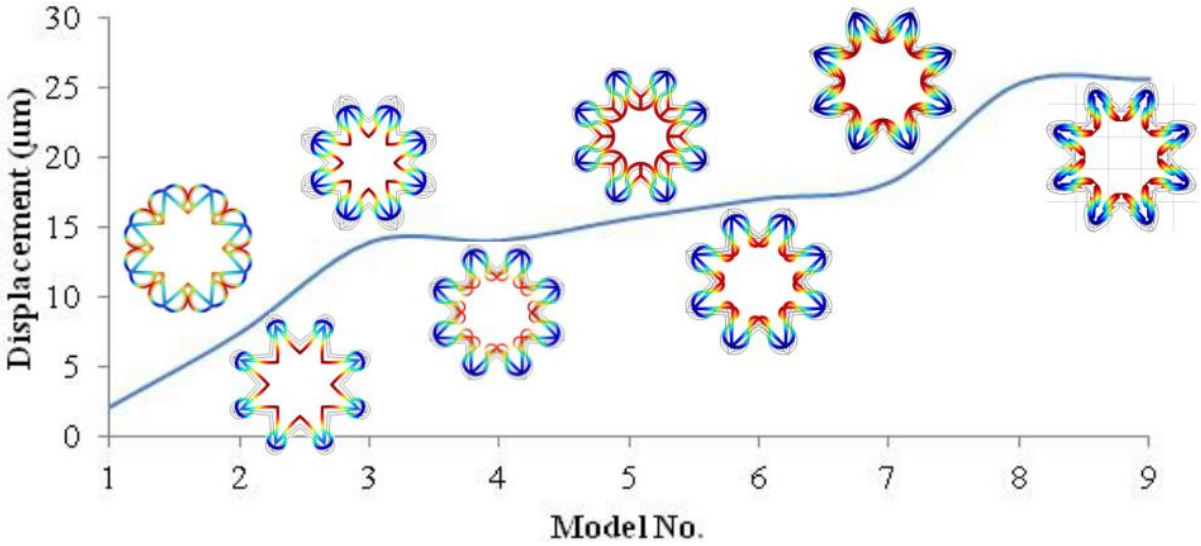

FIG. 5.20: THE DISPLACEMENT TREND AGAINST WITH DIFFERENT STAR MODELS.

A reliable material design, however needs to take into consideration also other factors. As already broadly described, the cell design comprises two materials that are shaped in such a way to allow the cell to act mechanically (expand/shrink) as desired. The two materials need to interact within each other to reach the described function, which means that they need to exchange loads in the form of internal stress. In other words, the forming materials must be able to sustain these stresses. Our design strategy was such to keep both materials into a linear stress range. The reached (numerical) stress levels were verified to be at the most 65MPa which is below the proportional limit of both materials (approximately 80MPa). Figure 5.21 shows in particular the total displacement and the von Mises stress distribution for the optimized design.

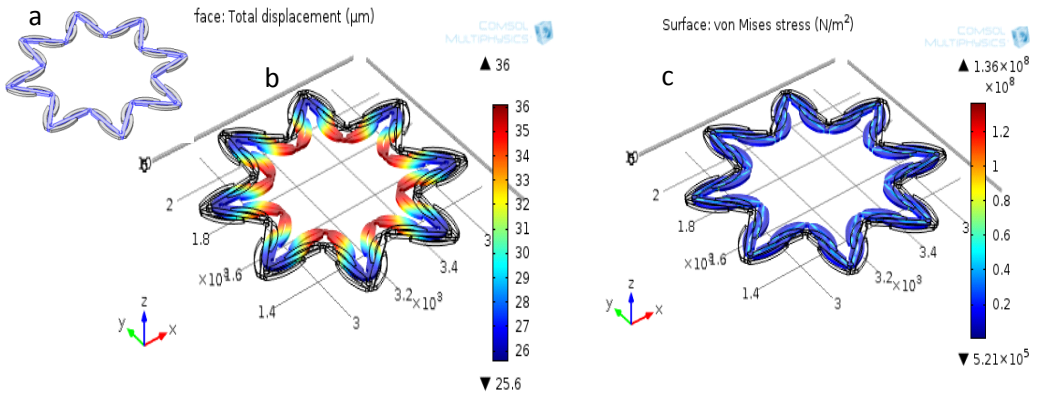

FIG. 5.21. A) COMSOL MULTIPHYSICS MODEL, B) MAXIMUM DISPLACEMENTT AND C) STRESS.

The coefficient of thermal expansion of the proposed design was calculated starting from the maximum displacement. The comparison with existing materials was performed by means of different methods as in table 7. This table shows very clearly that the proposed design only presents a negative coefficient of thermal expansion since its forming materials are both characterized by a positive coefficient. This key, and indeed successful aspect, can be easily viewed in Figure 5.22. In this figure, the optimized star design is compared with a uniform layer of Nylon when they are exposed to a temperature gradient from 0 to 500K (the most common temperature range used to characterize the coefficient of thermal expansion of materials). These numerical results clearly highlight that the Nylon film has an opposite response than that of the star. In other words, when temperature decreases, the star expands while the Nylon film shrinks. When temperature increases, the star shrinks and the Nylon film expands. Moreover, not only the response is opposite, but also the magnitude of expansion/contractions is lower in the Nylon case. It is worth noting that the existing negative thermal expansion materials, including ceramics and alloys, have a common coefficient range of about -10e-6 to -150e-6 1/K [37], while the thermal expansion coefficient of the designed star structure sets to a significantly higher value: -365.714e-6 1/K (Table 5.2). To the best of our knowledge, this represents today the highest ever presented negative expansion coefficient for polymeric materials and for all materials in general.

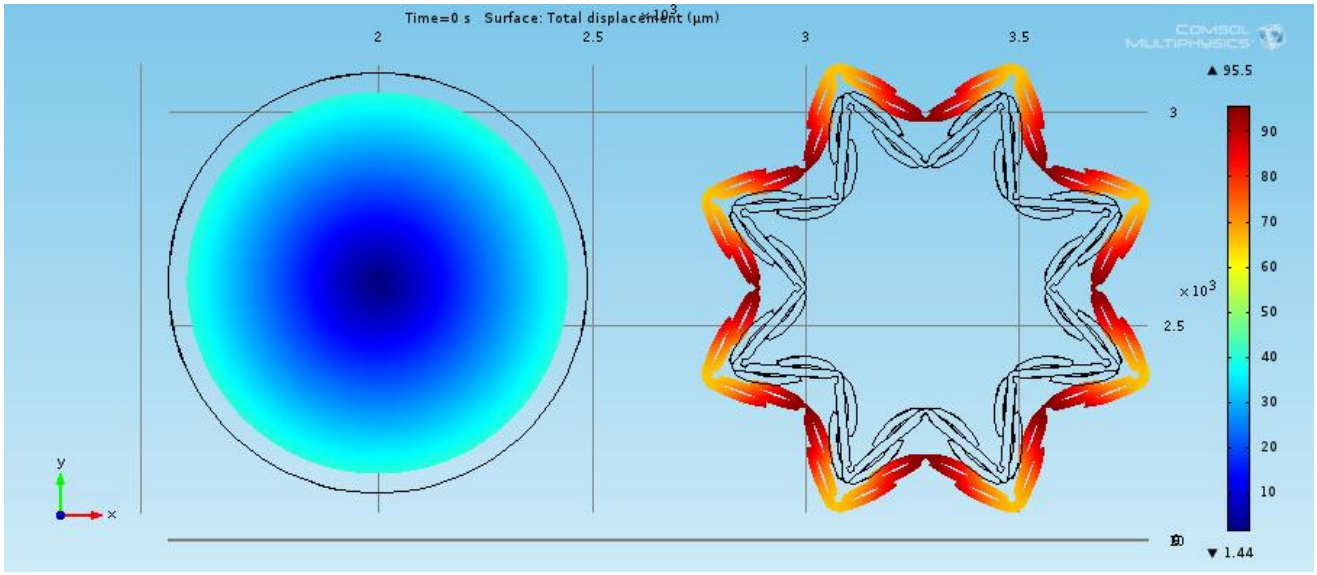

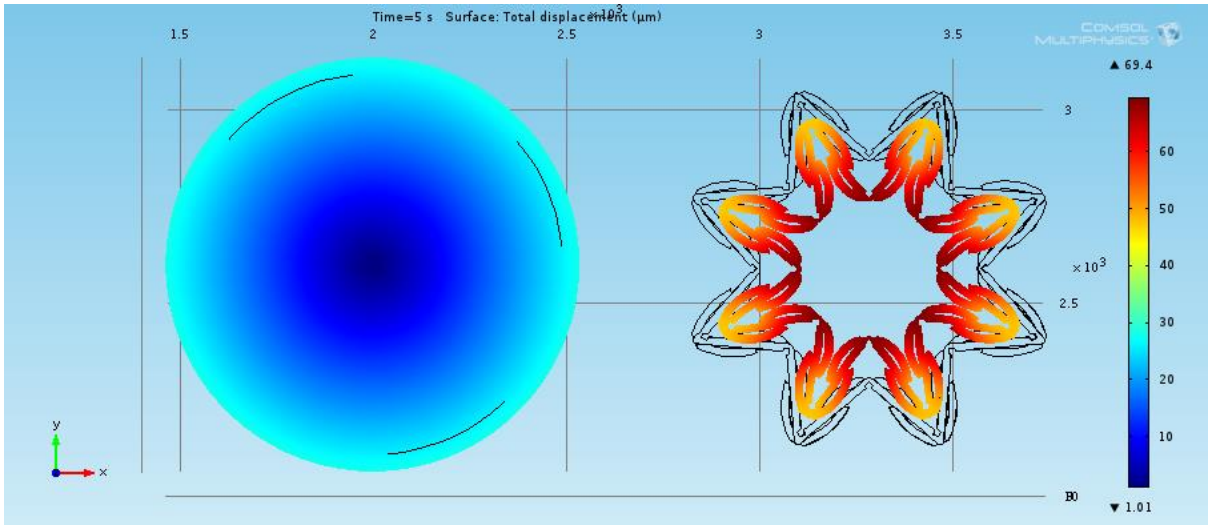

FIG. 5.22: COMPARISON OF THE STAR RESPONSE AND OF NYLON UNDER THE TEMPERATURE RANGE BETWEEN 0-500K.

Another important advantage of the proposed material design is that it is quite fast in response. Figure 5.23 shows the response over time of the star design when temperature increases from 0 to 500K. This graph clearly highlight that the response is very fast since the material seem to be adapting its shape at the same speed as temperature varies. However further analysis need to be taken into account to consider also the response of the intrinsic material properties with temperature. This could not be considered in this study because of luck of experimental data available in the literature toward this aim.

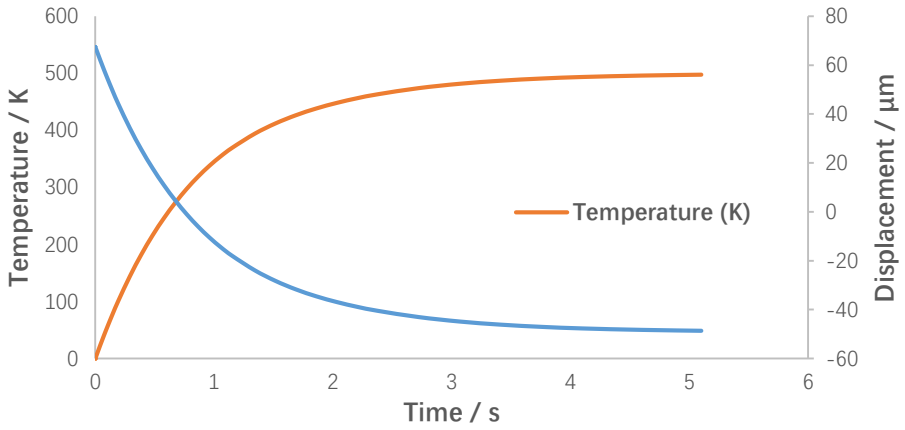

FIG. 5.23. SIMULATION RESULT OF RESPONSE OVER TIME OF THE STAR DESIGN WHEN TEMPERATURE INCREASES FROM 0 TO 500K.

TABLE 5.2: THE COEFFICIENT OF THERMAL EXPANSION COMPARISON.

	Star	Min	Max	Mean of Value	Mean of Weight
Displacement (μm)	-25.6	1.4	19.6	10.5	12.1
CTE (1/K)	**-365.714e^{-6}**	20e^{-6}	280e^{-6}	150e^{-6}	173e^{-6}
Range of negative CTE : -10 - -150 e^{-6} (including Ceramic & Metal alloy)					

5.2.6. Polymeric film with a miniaturized discrete structure and negative coefficient of thermal expansion

In the previous sections a novel cell design was proposed, analyzed and optimized to provide the highest ever presented negative coefficient of thermal expansion. The repetition of this unit cell over a plane gives rise to a discrete film whose response takes advantage of the response of the forming cells (a polymer film with a negative coefficient of thermal expansion). It is clear that the approach used to combine these cells is critical to achieve and reflect in a large scale the local response. Figure 5.24 shows the numerical results in which the unit cell was repeated 9 times along the x and y direction forming a 3x3 unit cells film. A variation in temperature from 0 to 500K shows again a very good agreement with the expectations. The film expands when temperature decreases and shrinks when temperature increases.

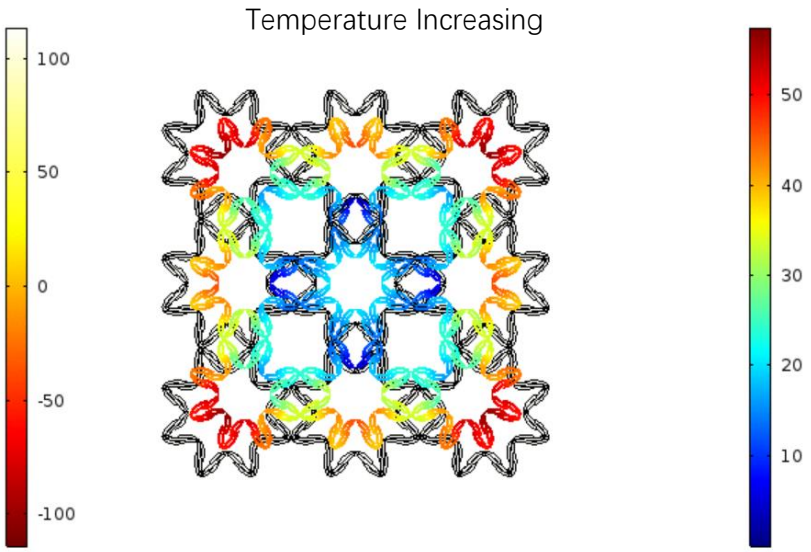

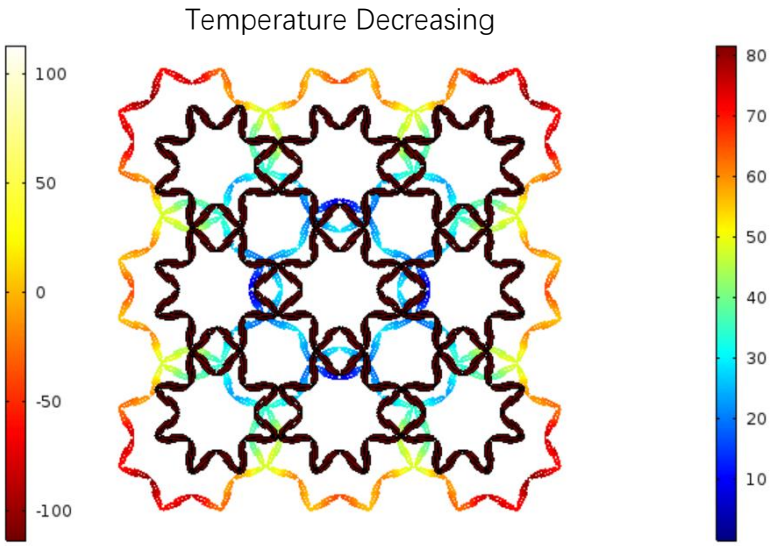

FIG. 5.24. DISCRETE FILM STRUCTURE IN THE SHRINKING AND EXPANSION MODES DUE TO TEMPERATURE VARIATIONS.

5.2.7. Experimental Activity

The fabrication of the designed materials is indeed a complex process since it requires shaping and precisely overlapping two different polymeric materials so as to achieve the desired functions. To this end a non-standard microfabrication process was successfully implemented after several trials in terms of adopted materials and fabrication steps. Here the successful process will only be reported and discussed in details. The main star structure is formed by a Polyimide layer and the internal constraints are formed by Poly (vinyl alcohol) also known as PVA that have a coefficient of thermal expansion of 28e-6 1/K and 100e-6 1/K, respectively. The thermal and mechanical properties of these materials are in line with the models reported in the previous section. The implemented fabrication process is divided in two key phases. First, the internal constrains are patterned and then the main star structure is pattern to overlap them in specific areas only. It is worth noting that the original fabrication attempts were opposite since first the star structure was patterned and then the internal constraints were fabricated on top of them. But this was causing several issues, thus the process was finally reversed. Figure 5.25 shows a schematic of the first phase of the fabrication process which was performed in a clean room environment.

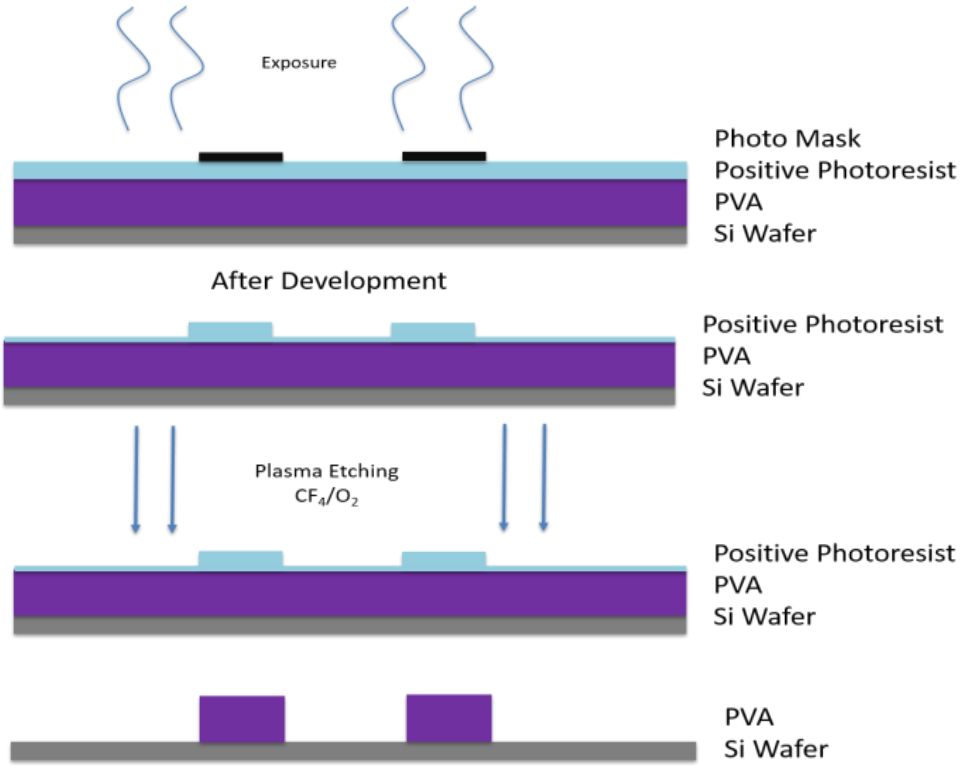

FIG. 5.25. SCHEMATIC OF THE FABRICATION PROCESS (FIRST PHASE)

An 8μm thick PVA layer was spin-coated on a [100] Si wafer, then it was covered with a 5μm thick layer of positive photoresist (AZ 4533) once the PVA was totally dried. The thickness of the photoresist and of the PVA were carefully measured and then monitored for the reasons described below. The photoresist layer was then coved with a negative photo mask, exposed to UV light in 20sec and developed using a AZ 351B developer with a development ratio of 30sec/μm. An important factor is that the photoresist layer was not fully developed during this step because the PVA layer can be wet etched by the AZ 351B developer. So, a residual 2μm thick photoresist layer (shown in the schematic) is left on top of the underlying PVA layer. A dry etching process was then performed using oxigen plasma O_2: CF_4 with a gas flow ratio of 7.5:2.5. It is worth noting that the thickness of the photoresist layer that was left on top is sufficient to allow a good shape patterning of the PVA features since the average etching ratio of PVA over the positive photoresist is 8:3 at the above mentioned plasma conditions.

In this way, during the plasma etching step, the first 2μm of photoresist that was intentionally left on top, is etched uniformly, then the photoresist become the mask for PVA etching. Since PVA and

photoresist have different etching ratio, the PVA can be perfectly etched when the photoresist is fully etched ways. In other words, the process was perfectly tuned.

The second phase of the process to fabricate the main star structure, is schematically represented in Figure 5.26.

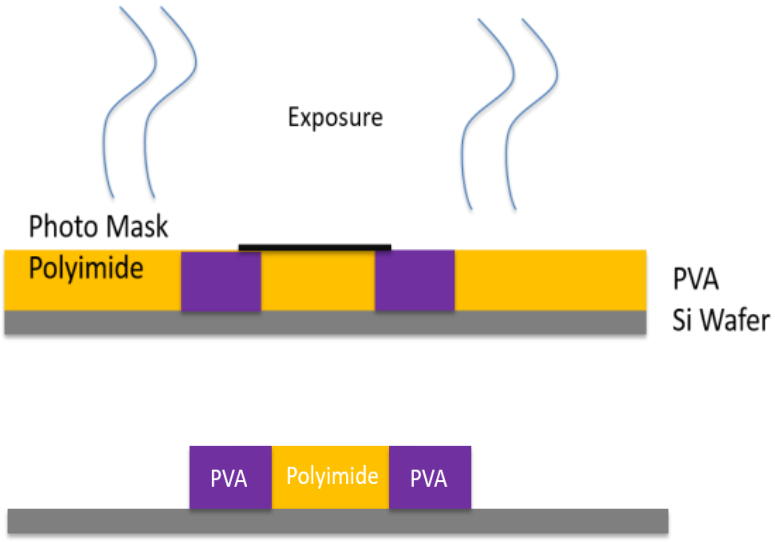

FIG. 5.26. SECOND PHASE OF THE DEVELOPED FABRICATION PROCESS.

The main star structure was made of photosensitive polyimide (PI 4110, Microsystem) which was spin-coated (3000rpm, 30sec) on the patterned PVA layer. A mask aligner was used to align and expose for 20sec the polyimide layer. A PA-401D and PA-401R developer were finally used to develop the exposed layer.

Once the discrete material was fabricated, a major challenge was found in its release or lift-off from the Si substrate which had the sole role of allowing the fabrication process. The PVA features were in fact not releasable from the wafer once they were treated up to 120℃ as required for the polyimide soft-bake. Different trials like, applying an addition layer between the Si wafer and PVA layer, reduce the soft bake temperature of photoresist and also change the processing order, but none of them lead to a successful release. This issue was finally solved by applying a piece of aluminum foil between the wafer and the PVA as shown in Figure 5.27.

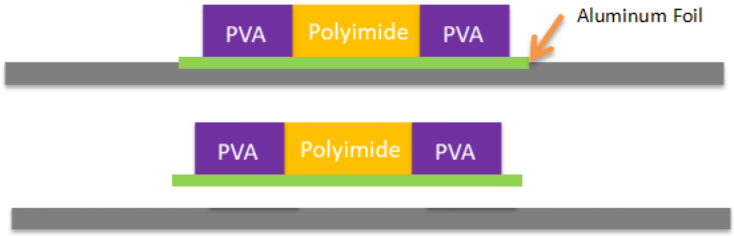

FIG. 5.27. THE SCHEMATIC OF THE MODIFIED FABRICATION PROCESS IN ORDER TO SOLVE THE LIFT-OFF ISSUE.

The results of the two fabrication phases can be viewed in Figure 5.28.

1st Phase: 2nd Phase:

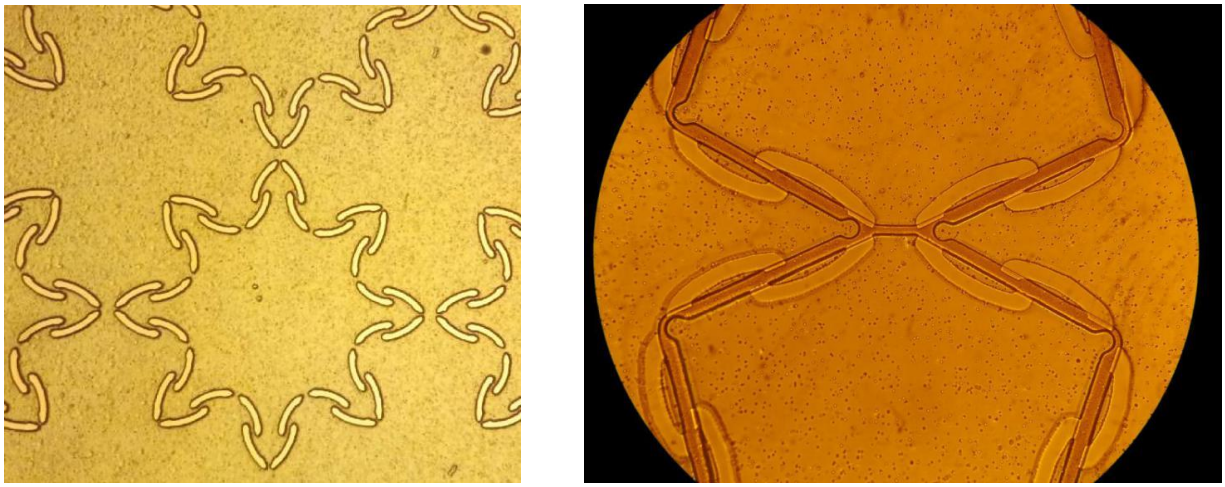

FIG. 5.28. RESULTS OF THE TWO PHASES OF THE OPTIMIZED FABRICATION PROCESS. OPTICAL IMAGES.

The upper optical microscope image shows the resulting internal constraints made of PVA, while the bottom image in the same Figure shows the additional polyimide structures that partially overlaps the PVA elements.

Figure 5.29 shows different star sample with different design which have been designed to have different CTE. The fabricated cells are compared with the predicted numerical data.

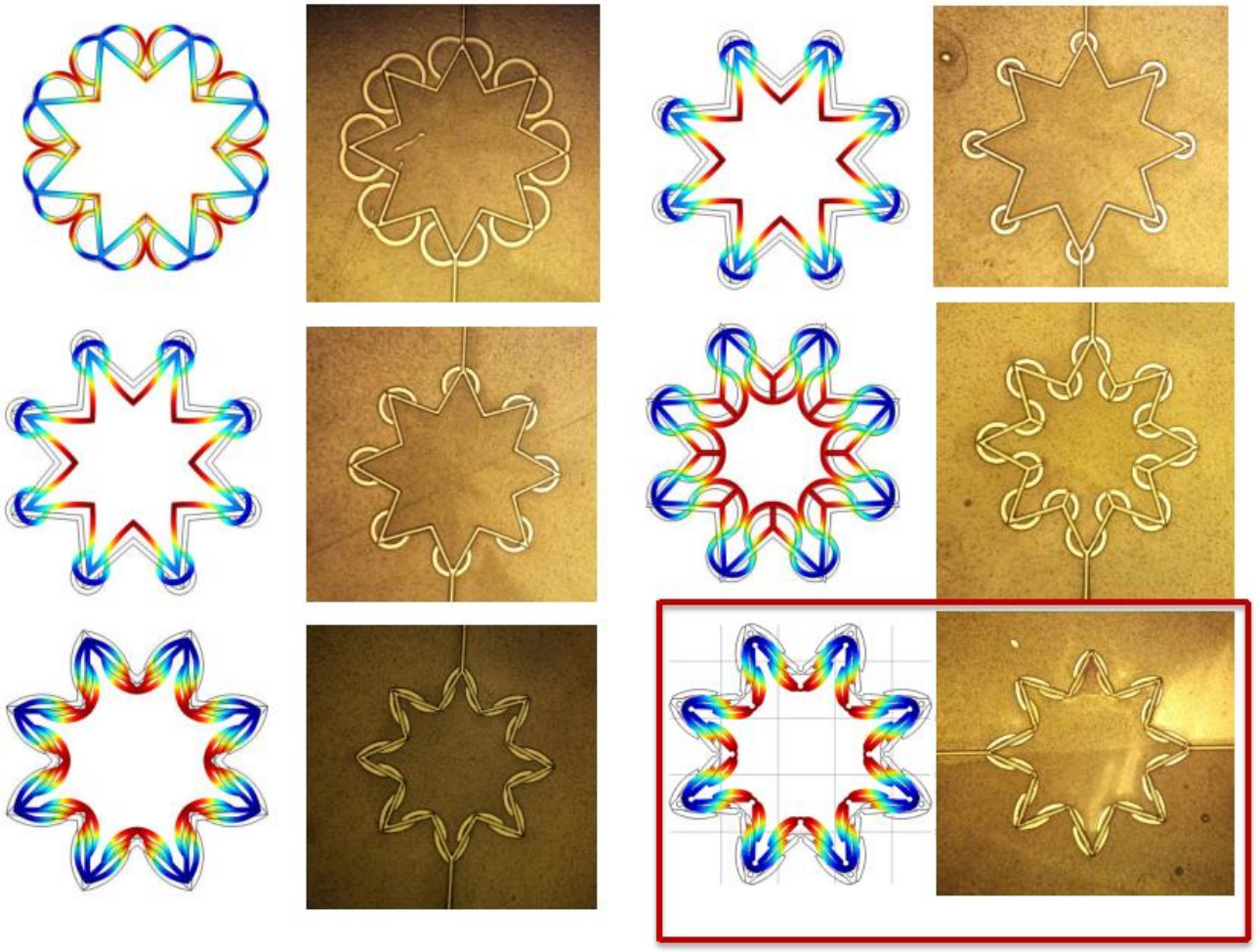

FIG 5.29. THE SAMPLE OF DIFFERENT STAR DESIGN.

Finally, the same procedure was used to fabricate the discrete polymeric material that is conceptually made by a repeating the unit cell in the xy plane. The resulting polymer film has a discrete cellular microstructure and is characterized by the predicted negative thermal expansion coefficient. An optical microscope image of a portion of one of the fabricated films can be viewed in Figure 5.30. The image focuses on several stars as well as on the interconnecting points between the stars forming the film.

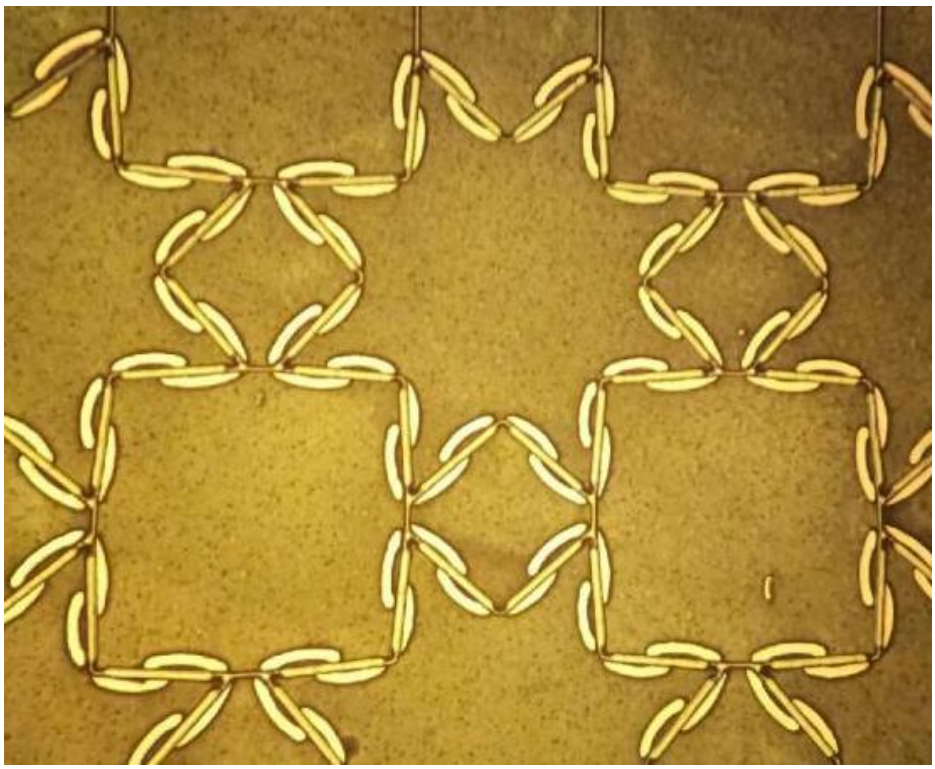

FIG. 5.30. FABRICATED FILM THAT, IN VIEW OF HIS POLYMERIC AND MINIATURIZED CELLULAR STRUCTURE, HAS A NEGATIVE THERMAL EXPANSION COEFFICIENT. OPTICAL IMAGES.

5.3. References

1. Joseph N Grima, Pierre S Farrugia, A system with adjustable positive or negative thermal expansion, Proceedings of the Royal Society A, Volume 463, issue 2082, 8 June 2007

2. Cora Lind, Two Decades of Negative Thermal Expansion Research: Where Do We Stand?, Materials 2012, 5(6), 1125-1154;

3. Koshi Takenaka , Negative thermal expansion materials: technological key for control of thermal expansion, Science and Technology of Advanced Materials, Volume 13, Number 1, 2012

4. Cao D , Bridges F, Kowach G R., and Ramirez A P. , Correlated atomic motions in the negative thermal expansion material ZrW_2O_8: A local structure study, Phys. Rev. 2003;68(B):014303

5. Tucker M G, , Goodwin A L, , Dove M T, , Keen D A, , Wells S A., and Evans J S O. Negative Thermal Expansion in ZrW_2O_8: Mechanisms, Rigid Unit Modes, and Neutron Total Scattering, Phys. Rev. Lett. 2005;95:255501.

6. Williams D J, Partin D E, Lincoln F J, Kouvetakis J., and O'Keeffe M. J. , The Disordered Crystal Structures of $Zn(CN)_2$ and $Ga(CN)_3$, Solid State Chem. 1997;134:164.
7. Margadonna S, , Prassides K., and Fitch A N. J. Am., The Disordered Crystal Structures of $Zn(CN)_2$ and $Ga(CN)_3$, Chem. Soc. 2004;126:15390.
8. Chapman K W, , Chupas P J., and Kepert C J. Direct Observation of a Transverse Vibrational Mechanism for Negative Thermal Expansion in $Zn(CN)_2$: An Atomic Pair Distribution Function Analysis, J. Am. Chem. Soc. 2005;127:15630.
9. Phillips A E, , Goodwin A L, , Halder G J, , Southon P D., and Kepert C J. Angew., Nanoporosity and exceptional negative thermal expansion in single-network cadmium cyanide., Chem. Int. Ed. 2008;47:1396.

10. Sumiyama K, , Shiga M, , Morioka M., and Nakamura Y., Characteristic magnetovolume effects in Invar type Fe-Pt alloys., J. Phys. F: Met. Phys. 1979;9:1665.

11. Namiko Yamamoto, Thin Films with Ultra-low Thermal Expansion, Advanced Material, Volume 26, Issue 19, May 21, 2014, 3076–3080

12. L.Que, J.-S. Park and Y.B. Gianchandani, "Bent-Beam Electro-Thermal Actuators for High Force Applications," IEEE Conf. on Micro Electro Mechanical Systems, Orlando, Florida. pp. 31-36, Jan., 1999.;

13. L.L. Howell and S.M. Lyon,"Thermomechanical In-Plane Microactuator (TIM)", U.S. Patent No. 6,734,597, issued May 11, 2004.

14. R. Cragun and L.L. Howell, "Linear Thermomechanical Microactuators", Microelctromechanical Systems (MEMS), at the 1999 ASME International Mechanical Engineering Congress and Exposition, pp. 181-188, November, 1999.

15. Yogesh B. Gianchandani, Bent-Beam Strain Sensors Member, IEEE, and Khalil Najafi, Member, IEEE

16. JOURNAL OF MICROELECTROMECHANICAL SYSTEMS, VOL. 5, NO. 1, MARCH 1996

17. Michael S. Baker, Richard A. Plass, Thomas J. Headley, Jeremy A. Walraven, Final Report: Compliant Thermo-Mechanical MEMS Actuators, LDRD #52553SANDIA REPORT, SAND2004-6635, Unlimited Release, Printed December 2004

Chapter 6

Temperature Driven Out-of-Plane Local/Global Morphing

In Chapter 4 it was demonstrated the need of having a polymeric material characterized by a negative coefficient of thermal expansion in order to improve the out-of-plane morphing capability of a bilayer system, driven by temperature, without the need of adding a significant number of layers. In Chapter 5 a novel film design was presented and was proven to be the best ever presented in literature in terms of negative coefficient of thermal expansion. In this chapter the aforementioned film is used to maximize the global out-of-plane morphing capability of the bilayer. Moreover, a novel concept is presented for allowing a material to morph not only at the global level, but also at the local level (microscale) by means of a pixelling approach. The presented morphing material has the potential to overcome several limitations of known morphing materials that are mostly affected by slow response speed, loss of rigidity during shape changes, limited number of shapes, global (macro-scale) morphing only. The here designed material has the potential to pave the way to a new class of morphing materials.

6.1. Novel Temperature Activated Morphing Material

Here the design of a novel temperature driven morphing material is presented. The key concept was already presented in Chapter 4 in which it was demonstrated that, the simplest but most efficient morphing system, whose shape can adapt to temperature changes, consists of a bilayer system in which one of the layer needs to have an **ultra-low negative coefficient of thermal expansion.** in Chapter 5 the design of a novel polymeric material whose properties reflect the needs, was presented and is here used for out-of-plane morphing purposes. It is worth noting that, we are focusing in out-of-plane (3D) morphing only, just because **the designed polymeric film is** already intrinsically a **2D morphing material** that can be **activated by temperature** and that can morph in-plane providing large (or tunable) expansions and contractions.

The 3D morphing is here achieved grabbing mismatches in coefficient of thermal expansion within the layers of a bilayer system in order to drive morphing, instead than exploiting, for instance, changes or phase transformations of the material molecular structure when temperature reaches specific critical values. The material design is shown in Figure 6.1. It consists of a polymeric film (e.g. polyimide) that has an ultra-high coefficient of thermal expansion that is sandwiched with another layer characterized by a large positive coefficient. The negative coefficient layer is made of the cellular polymeric film described in chapter 5 while the other layer could be made of Nylon (280e-6 1/K). The design of the proposed morphing material is shown in Figure 6.1

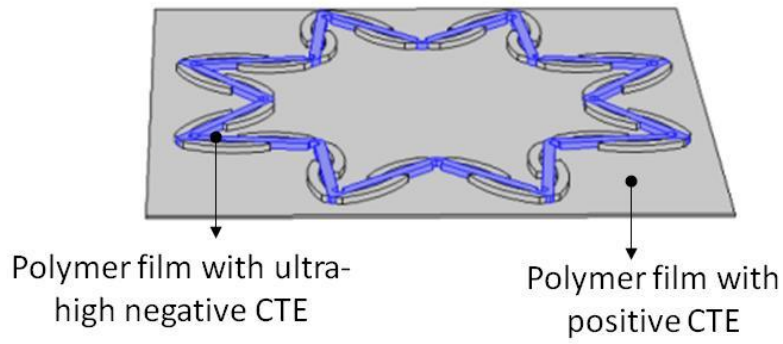

FIG. 6.1. DESIGN OF THE 3D MORPHING FILM.

The above layer is formed by a skeletal structure (the star) whose diameter is 960μm while the length of the square substrate is 1000μm. The models used to simulate the material response are the same as that previously described, so the material is fully constrained at the edges of the plate.

Consequently, once temperature reaches 120°C, a 45.5% out of plane deformation is reached (Fig. 6.2).

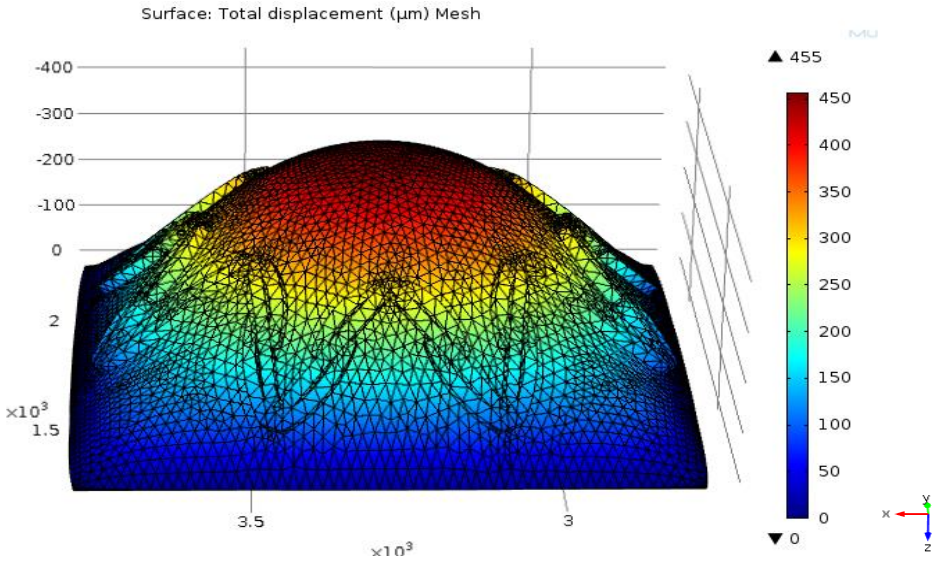

FIG. 6.2. MAXIMUM OUT-OF-PLANE DEFORMATION OBTAINED BY CHANGING THICKNESS RATIO.

It is worth noting that this result reflects an optimization that was performed on the thickness ratio when the total thickness is 20 μm. The maximum percentage of deformation, 45.5%, is reached when the thickness of the substrate is 6μm. This is because the optimization of the multilayer system in terms of thickness ratio was performed in Chapter 4 considering layers of continuum material which is different from the current design in which the second layer is formed by a discrete material.

In order to understand the effectiveness of the proposed material design, a comparison of this design (named: 2-layer with star) with the optimized response of multilayers (bi- and tri-layers) made with continuum films that are all characterized by a positive coefficient of thermal expansion (named: 2-layer; 3-layer), or by a positive layer and a negative layer (the substrate) both of continuum material (named: 2 Layer with negative substrate), is performed. The corresponding results are reported in Figure 6.3. The trends clearly show the drastic 3D morphing improvement that is reached with the proposed design that presents a 42% improvement of deformation percentage when compared with the 2-layer case. In agreement with the studies reported in Chapter 4, the 2-layer system presents the smallest degree of deformation, the addition of a layer to it, slightly improves the result, but a bilayer with a negative coefficient has a much stronger impact on the material response. This is further improved by replacing the continuum layer that has a negative coefficient of thermal expansion with the star design.

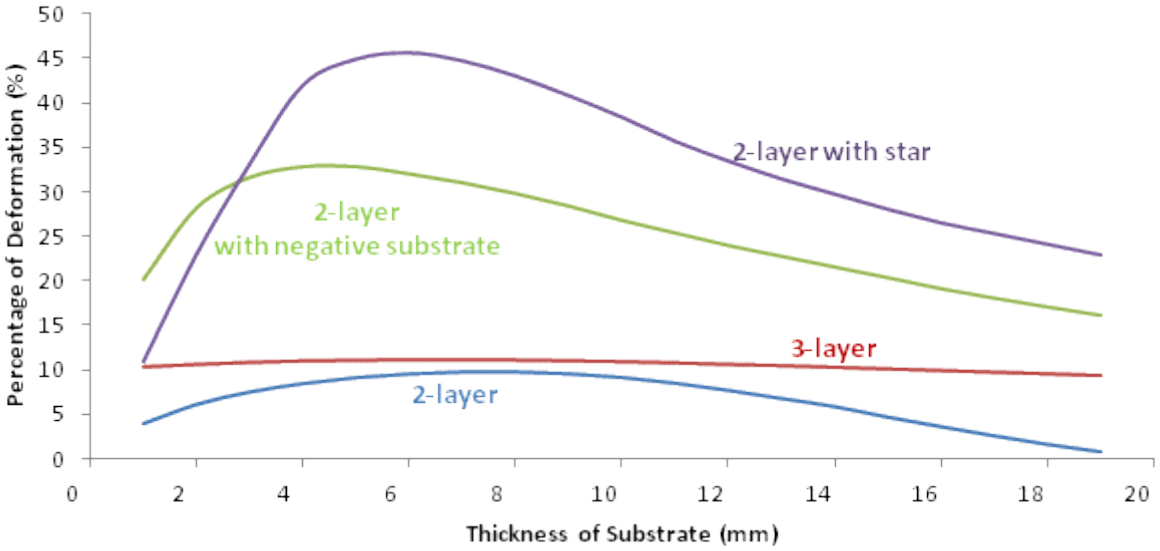

FIG. 6.3. PERCENTAGE OF DEFORMATION TRENDS OF BI AND TRILAYERS WITH ALL POSITIVE LAYERS OR WITH A COMBINATION OF POSITIVE AND NEGATIVE COEFFICIENTS.

6.2. Material Design Improvement

In the previous section it was demonstrated that the use of the star design improves significantly the out-of-plane morphing capability of the material not only because it shows a negative coefficient of thermal expansion, but also because this coefficient is maximized through this discrete material design. The material design optimization was also performed in terms of the relative thickness of the layers. In this section, a further material design optimization is performed to achieve:

- further out-of-plane deformation improvement
- morphing speed

The first is achieved by playing again with size, but in this case, instead than varying the layers thicknesses, the substrate size is changed while the star size is kept fixed. The second objective is achieved by modifying the heating location and methods within the star.

Further out-of-plane deformation improvement

The reference model is a two-layer system in which one layer is the star (made with Polycarbonate and Nylon) and the other layer is Nylon. The substrate layer in this case has a circular shape (and not square as in previous sections) and the system is constrained in the center as shown in Figure 6.4. This is done to have a uniform deformation and let the material deform freely. The substrate diameter is initially the same as the outer star diameter (979.3548μm). The bilayer was then heated from 20 °C to 120 °C.

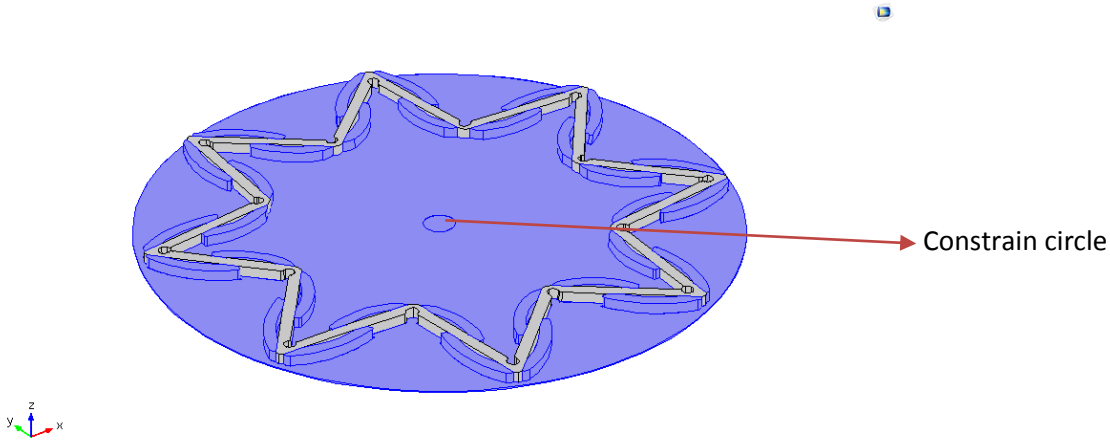

FIG. 6.4: COMSOL MULTYPHYSICS MODEL, BUILD BY TWO MATERIALS: POLYCARBONATE (GREY) AND NYLON (BLUE) CONSTRAINED IN THE CENTRE. THE DIAMETER OF THE SUBSTRATE IS 979.3548 MICRO METER.

The result of this reference model is shown in Figure 6.5 which provides a uniform deformation of 10%. The variation of deformation degree is due to the different constrain which previous case has edge constrain and this case as center constrain.

Starting from the reference model, 13 further models in which the substrate diameter was increased from 979.3548μm to 2500μm were performed under the same constrains and environmental conditions (temperature range is between 0-500K). The results are reported in Figure 6.6 in terms of degree of displacement over time. This graph shows that degree of deformation increases with the diameter increase. This is because the substrate deformation is induced by the star that is always located in the centre of the plate. The star locally bends the plate and the remaining portion of the substrate, which is not covered by the star, will follow the same induced deflection. From this point of view, the larger size of the substrate has greater ability to morph. It is obvious that these results reflect ideal cases in which the system is perfect and is embedded into a perfect environment. The imperfections of the real world will cause disturbances to this ideal behaviour and will stop this process earlier. For instance, a factor that can't be taken into account in the simulation is the flexibility of the material that will present a limit of size after which, even if the material is punched in the centre part (through the star), the low rigidity of the material will not allow to let this punching effect be propagated to large areas. A local effect only will be observed.

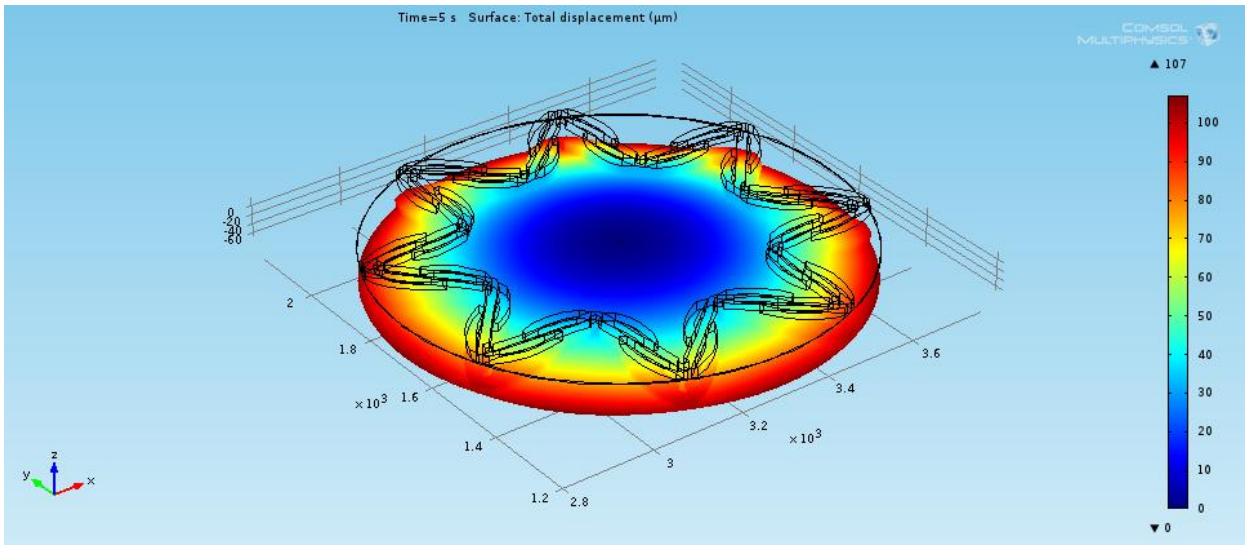

FIG. 6.5: SIMULATION RESULT OF THE TESTING REFERENCE MODEL, WHICH SHOWS A MAX DEGREE OF DEFORMATION OF ABOUT 10%.

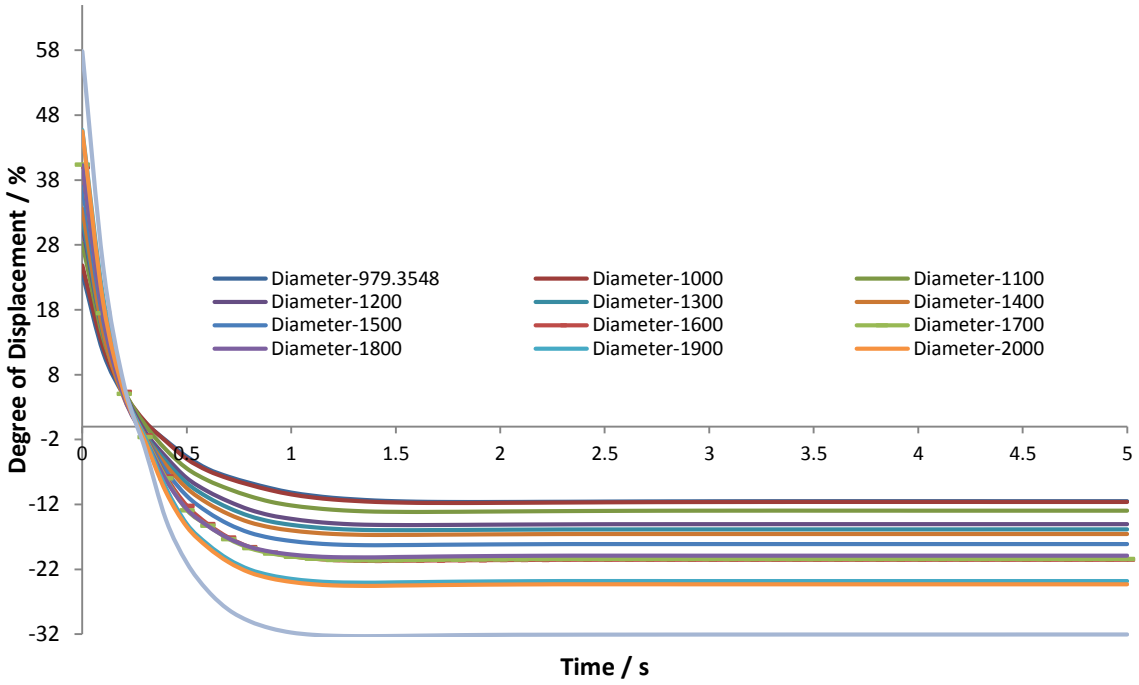

FIG. 6.6: DEGREE OF DEFORMATION RELATED TO DIFFERENT SUBSTRATE DIAMETER FROM COMSOL SIMULATIONS.

Morphing speed

One of the greatest limits of some existing morphing materials (e.g. shape memory polymers) is the slow response time. The typical recovery time of SMPs goes approximately from 30s to few minutes. Accordingly, to the numerical study, the response time of the proposed bilayer system that contains the star, is characterized by an overall material response of 1 second as can be viewed in Figure 6.6. The degree of deformation over time changes very rapidly within the first second and then reaches a steady plateau.

Here further design improvements are performed to increase the response time of the material by introducing different heating methods. In Figure 6.7, the list of all adopted heating methods (for a total of 12 different cases) is schematically reported.

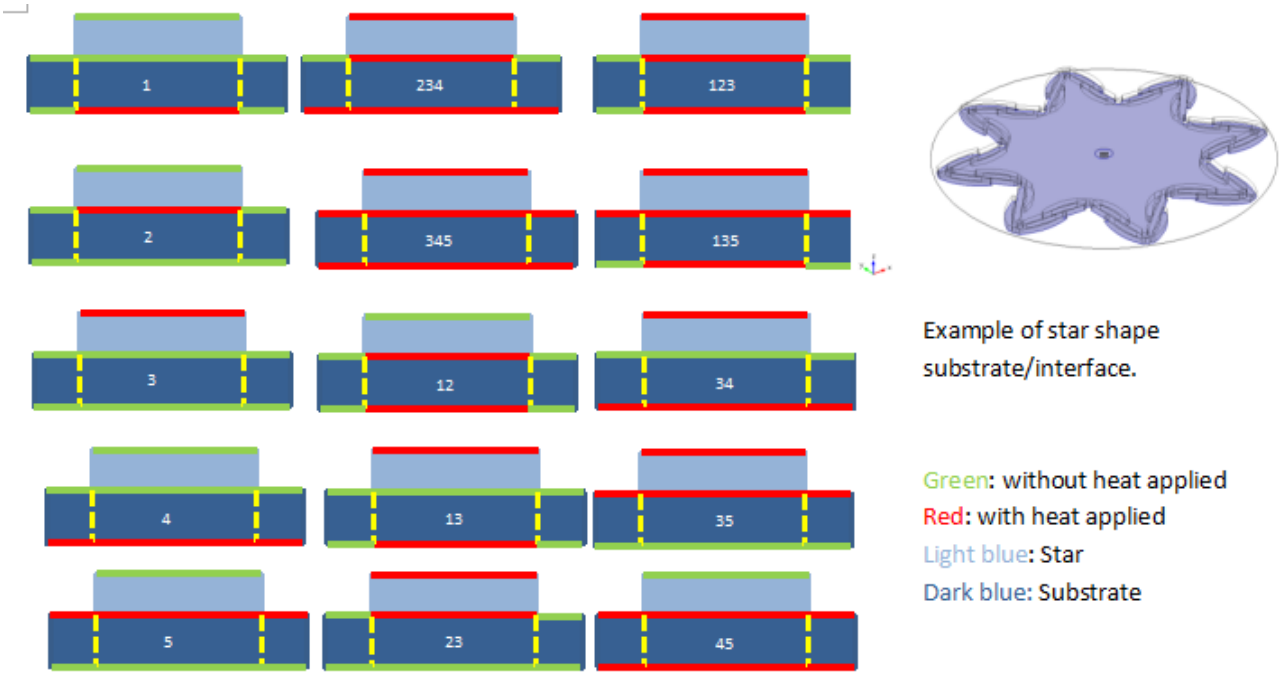

FIG. 6.7. COMBINATION OF POSSIBLE HEATING METHODS. 1: STAR SHAPE SUBSTRATE; 2: STAR SHAPE INTERFACE; 3: TOP STAR LAYER; 4: FULL SUBSTRATE; 5: FULL INTERFACE.

All of the possibilities of heating method were simulated under the same conditions as the previous simulations (Fig. 6.6). Firstly, the simulations were run in the time range from 0 – 0.15s and 0.002s per step. The results are shown in Fig. 6.8 in which two main groups can be highlighted. One group reaches a maximum temperature (500 °C) within 0.02s (in the red circle), another group reaches the maximum temperature in 0.12s. In the next step of simulation, the combinations with a red circle in Fig. 6.8 were simulated in the time range from 0-0.005s with 0.0001s per step. The result is displayed in Fig. 6.9 in which the three combinations: 34, 234 and 345 result being the fastest in response. The last step is to have a close view of these three combinations, the simulations condition was set as from 0-0.001s with 0.00001s per step for which the result is shown in Fig. 6.10. The combination 234 and 345 result being almost the same. In these cases, the maximum temperature is reached in 0.008s. From the label of the combination 234 and 345 shown in Fig. 6.10, the fastest heating method is to introduce the heat from all of three surface, since the sample size is in micro scale, the different between these two combinations (234 and 345) is limited.

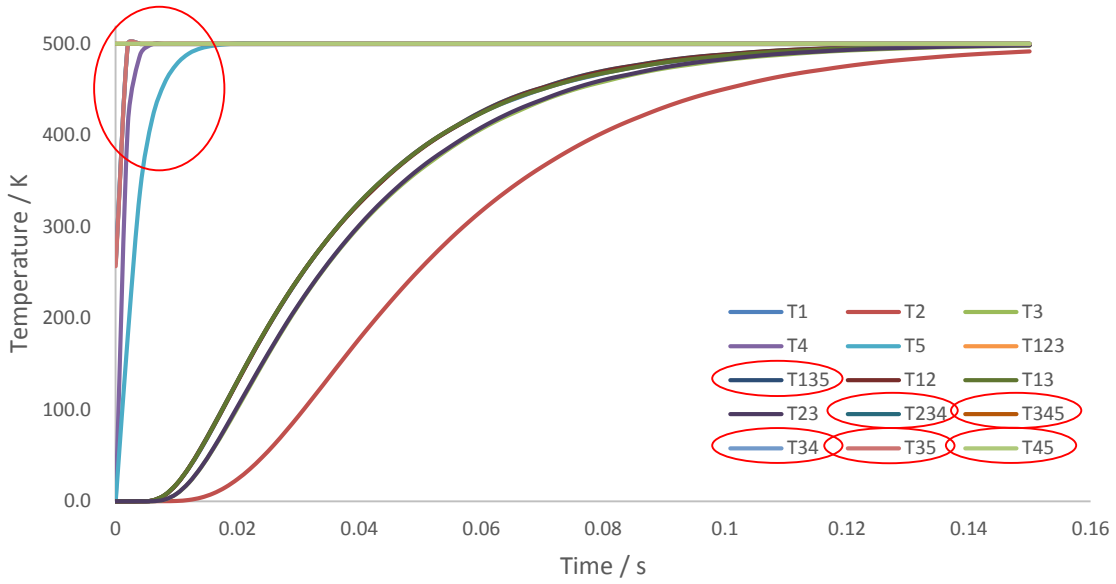

FIG. 6.8. SIMULATIONS OF DIFFERENT HEATING METHODS, FROM 0-0.15S WITH 0.002S PER STEP.

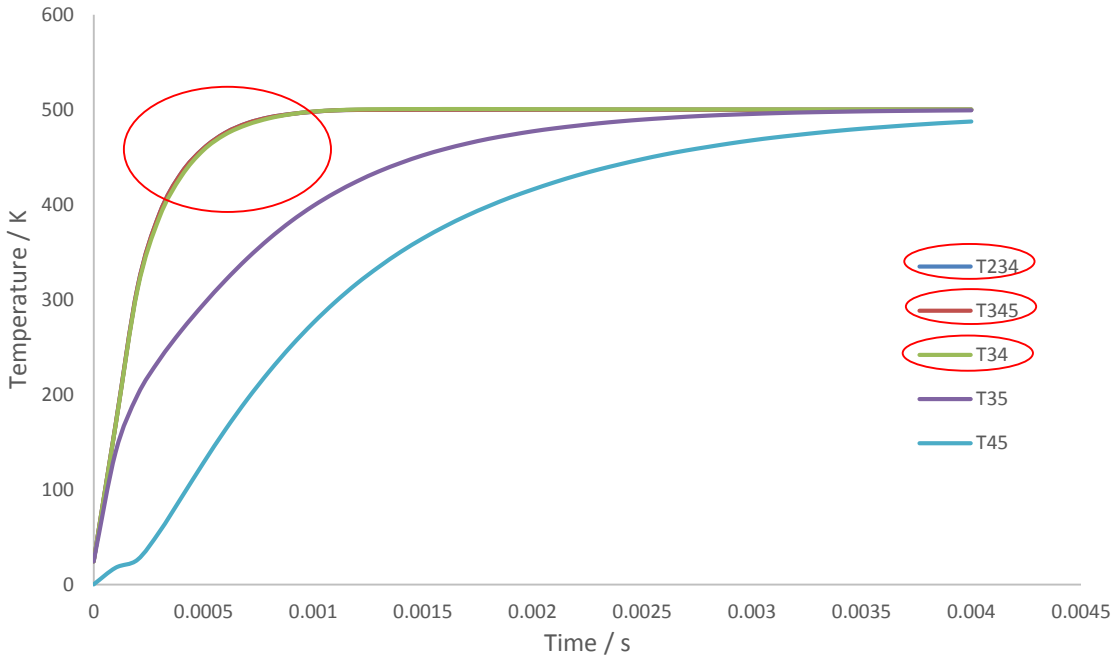

FIG. 6.9: SIMULATION OF FAST HEAT METHOD, FROM 0-0.005S WITH 0.0001S PER STEP.

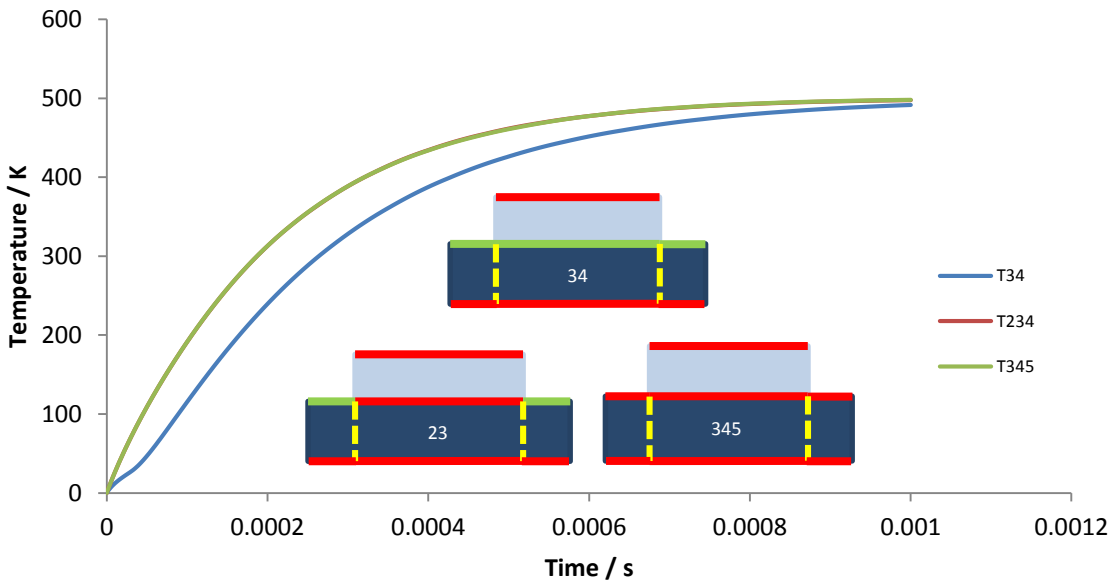

FIG.6.10: SIMULATIONS OF THE THREE FASTEST COMBINATIONS, FROM 0-0.001 WITH 0.00001S PER STEP.

Shear Stress

The final step of studying is related to the operation condition according to the shear stress limitation of the material which used in the composite system. The cut plane was taken from the reference model which shows the interface (z=0, Fig. 55), then the von Mises stress that occurs in this cut plane was analysed. The maximum shear stress of the material used in this system is about 40 MPa, so the right operation condition should be in the range for which the shear stress does not exceeds this value. In our model, the shear stress at the interface is less than 40MPa when the temperature between 255-375K with the max degree of deformation is 6% (60µm). Since the degree of deformation is not as much as expected, the composite system can be improved by further material selection and geometry development in order to increase the degree of deformation.

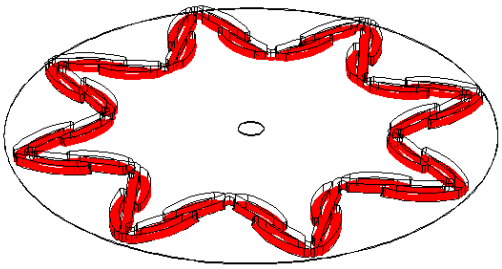

FIG. 6.11. THE 3D CUT PLANE WHICH SHOWS THE INTERFACE BETWEEN SUBSTRATE AND STAR LAYER.

6.3. Local Morphing and Infinite Number of Shapes

Local morphing is a key aspect that should be addressed in morphing materials. This is because being able to independently and locally modify the shape of a material at the microscale, can allow to reach unprecedented functions. For instance, this could be used to reduce drag to a micro air vehicle, to improve the blood flow in arteries etc. To reach this aim, the concept of material pixelling is here introduced. Pixelling means that, as in computer or TV screens, the shape can be reached by splitting the material into several little pieces whose shape can be independently controlled. The governing piece in this work is chosen to be the star size. Figure 6.12 shows the concept for a 4x4 arrangement.

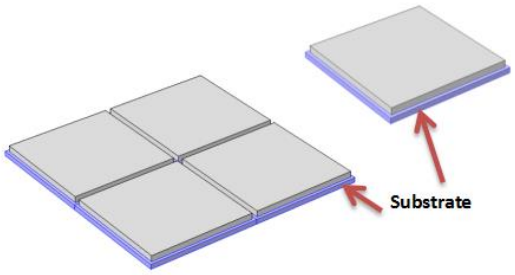

FIG. 6.12. COMSOL SIMULATION MODELS OF SINGLE PIXEL AND 4 PIXELS ARRANGEMENT

The mechanical and thermal properties are shown in table 6.1. The single pixel was simulated under the same condition as previous models in which the four bottom edges were fixed. The polycarbonate is used as substrate. Figure 6.13 shows the optimization of the top layer thickness to maximize the out of plane morphing in this constrain configuration.

Local morphing in a pixel arrangement can be achieved by controlling the local temperature, and this can be used also to achieve an ***infinite number of shapes***. Figure 6.14 shows an example of local shape changes.

TABLE 6.1: THE MECHANICAL AND THERMAL PROPERTIES USED IN CUBES MODEL.

Quantities	**Symbols**	**Dimensions**	**Polycarbonate**	**Nylon**
Young's modulus	E	Pa	7.9e9	$2e^{9}$
Thermal expansion coeff.	A	1/K	$23e^{-6}$	$280e^{-6}$

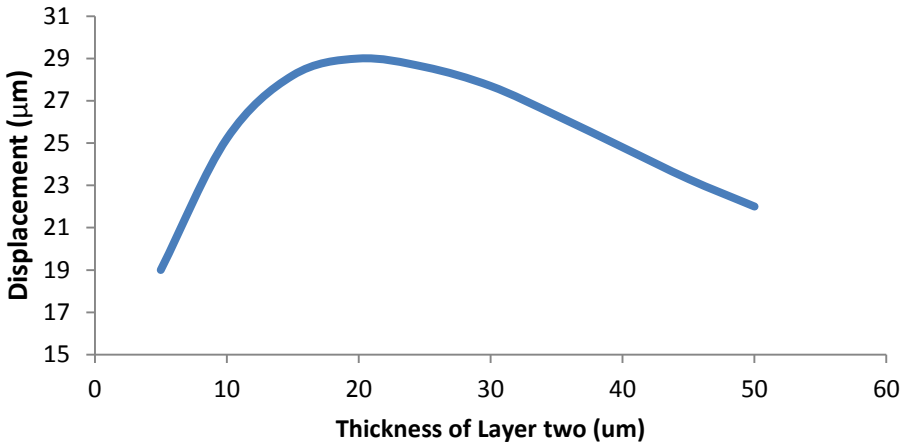

FIG. 6.13. THE TREND OF DISPLACEMENT AGAINST THICKNESS OF TOP LAYER.

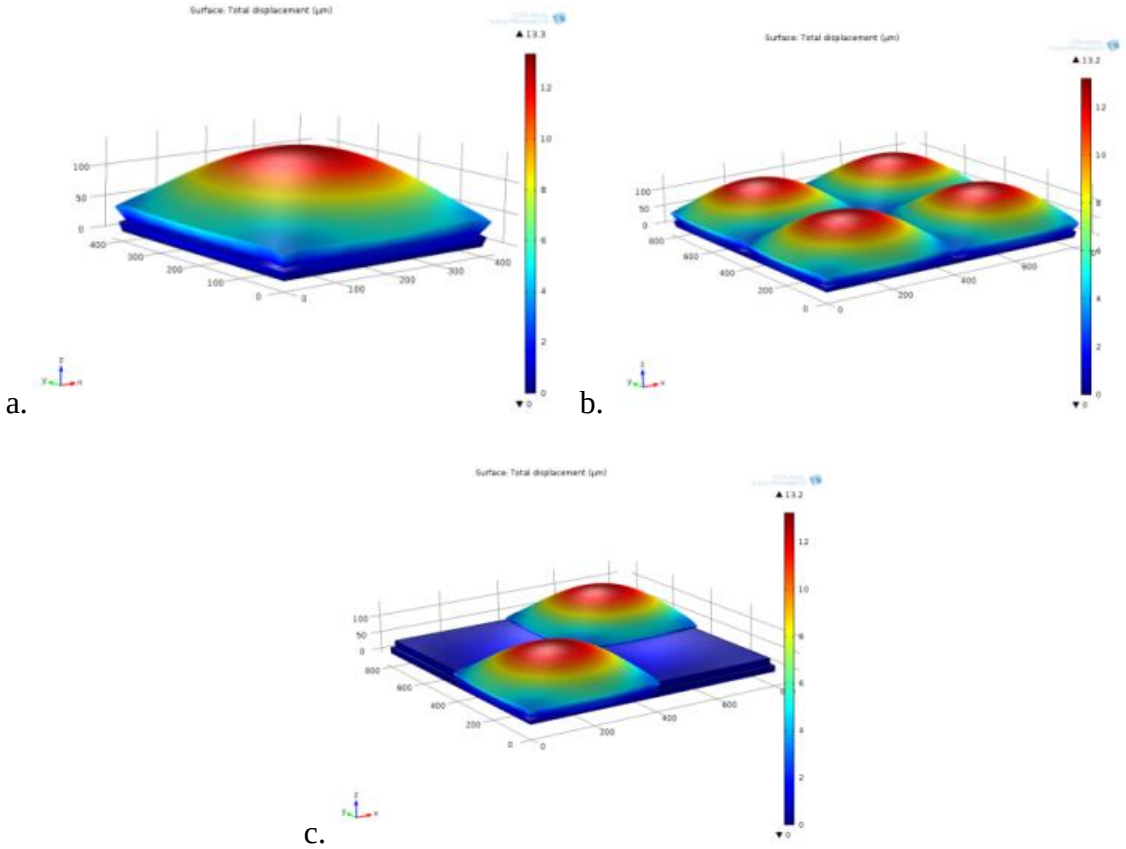

FIG. 6.14. DIFFERENT SHAPE CHANGES BY CONTROLLING THE LOCAL TEMPERATURE. A) SINGLE CELL, B) FOUR CELLS WITH FULL HEATING OUTPUT, C) FOUR CELLS WITH TWO CELLS HEATING OUTPUT.

Conclusions

In this study, we designed, fabricated, tested and characterized a passive and an active cellular micro structured film which could be extremely useful for morphing applications. The passive film consists on miniaturized polyimide cells whose shape take inspiration from the classical hexachiral structure. A novel fabrication process based on non-standard microfabrication techniques, was designed and optimized. The fabricated samples were experimentally tested under different environmental conditions to simulate an air environment as well as a fluid environment and in the latter case fluids with varying surface tension and viscosity were investigated. This was done because of the ultra-light weight and miniaturized film structure which makes the film extremely sensitive to the above listed factors. The film characterization was quite broad and complex so just a few of the observed properties are here highlighted. The film was found to be anisotropic in its response, to have a fully elastic response even after reaching the so called auxetic failure for which the interconnecting wires undergo into elastic buckling. The loading/ unloading cycles show a variable hysteresis which becomes more significant at the film level than at the cellular level. This hysteresis as well as the auxeticity of the material is strongly related to the loading speed, to the viscosity of the liquid environment, to the surface tension and to the loading constraints. All these factors have a deep and often different impact into the response at the local (single cell) or global level (film). The successful design and experimental validation of a novel auxetic film that has highly expandable properties was finally presented.

The novel temperature-driven cellular film (polyimide-based) was also carried out from a theoretical (modeling) and experimental prospective. A broad part of this study was related to the material design and its microstructure optimization to optimize first the thermal response of the cellular film and then the local and global morphing capability in 3D. An important amount of work was also given to the design and optimization of the fabrication procedure which resulted being quite complex in this case. The results of this study are interesting. First of all, the design of a cellular film that is able to provide a tunable thermal response was optimized. In particular, the largest ever presented coefficient of thermal expansion (-357 e-6

1/K) has been presented. The uniqueness of this approach is that this is done by using only constitutive polymers that have a positive coefficient of thermal expansion (polyimide and PVA). This material has been successfully used to create a bilayer system that is capable to provide a maximized out-of-plane morphing. Pixelling of this bilayer system can be used for local film morphing.

The advantage of the presented active film is that it is characterized by a potentially unlimited number of shape changes, it is ultra-light weight, it can be self-activated by means of an integrated heating system, it keeps its rigidity during shape changes and is relatively fast in its response (faster for instance of shape memory polymers, alloys etc.), it uses standard polymers that can be easily synthesized while providing unique properties which are not available today in any known existing polymer (with the exception of natural polymers like elastine, that however present this behavior just because of their special liquid environment).